Peripheral Virus Infection-induced Microglial and Neuronal Alterations

Thesis

for the degree of

doctor rerum naturalium

(Dr. rer. nat.)

approved by the Faculty of Natural Sciences of

Otto von Guericke University Magdeburg

By: M. Sc. Henning Peter Düsedau

Born on 04.03.1990 in Wolmirstedt, Germany

Examiner: Prof. Dr. rer. nat. habil. Ildiko Rita Dunay

Prof. Dr. rer. nat. habil. Carsten G. K. Lüder

Submitted on: 20.06.2022

Defended on: 29.11.2022

"Sometimes science is a lot more art than science.

A lot of people don't get that."

Rick Sanchez

PREAMBEL

Results of the present work were published in:

Düsedau HP, Steffen J, Figueiredo CA, Boehme JD, Schultz K, Erck C, Korte M, Faber-Zuschratter H, Smalla K-H, Dieterich D, Kröger A, Bruder D, Dunay IR (2021) Influenza A Virus (H1N1) Infection Induces Microglial Activation and Temporal Dysbalance in Glutamatergic Synaptic Transmission. *mBio* 12:e0177621. https://doi.org/10.1128/mBio.01776-21

Text sections from the above-mentioned publication were used in sections 2.2, 3, 4, and 5.

ABSTRACT

Infection with influenza A viruses (IAV) may lead to seasonal epidemics among all age groups mainly affecting bronchial epithelial cells of the upper respiratory tract. A viral infection is initially sensed by components of the innate immune system, leading to a swift production of pyrogenic cytokines to mount an anti-viral immune response. However, systemic inflammation is accompanied by fever and further results in altered behavioral routines, such as reduced appetite and social isolation, implying a disturbed brain homeostasis that may precede neurological disorders. Previous experimental studies reported about dysregulation of microglial cells, increased expression of inflammatory cytokines, and compromised hippocampal neuronal morphology causing impaired cognition in mice upon influenza infection. However, characterization of microglia activation and underlying processes of behavioral alterations remained unaddressed. Utilizing a murine infection model with a non-neurotropic IAV strain that mimics the disease progression in humans, this study demonstrates that an infection-induced peripheral immune response is trailed by a temporally disturbed expression of blood-brain barrier-associated proteins. Although histological examination of brains from IAV-infected mice displayed no noticeable pathological effects, in-depth characterization of microglial cells via flow cytometry highlighted an increased surface expression of major histocompatibility complex classes I and II, cluster of differentiation (CD) 80, and F4/80 upon infection. Gene expression analysis of lysosomal proteins, scavenger receptors, and complement factors further deciphered an increased capacity of microglia-mediated synaptic pruning in IAV-infected mice. Finally, a novel multiplexed flow cytometry-based approach was established and applied to scrutinize previously described neurological alterations. Notably, quantitative analysis of synaptosomes isolated from cortex and hippocampus revealed a significant reduction of the vesicular glutamate transporter 1 (VGLUT1), thereby highlighting a dysbalance in excitatory neurotransmission in IAV-infected mice. In summary, the present study highlights the disturbed CNS homeostasis indicated by distinct microglia activation and altered glutamatergic neurotransmission as a result of the peripheral infection-induced systemic inflammation, further underlining the importance of the body-brain axis.

TABLE OF CONTENTS

1. INTRODUCTION

The brain is an exceptional organ that is able to process and store large amounts of information but also to facilitate social interactions and behavior. Although the development and function of the brain have been intensely studied over the last decades, many aspects of brain pathology still remain unclear. For example, the underlying mechanisms of behavioral alterations induced by peripheral infections are not fully explained. As such alterations are hypothesized to act as triggering events leading to certain neuropsychiatric disorders or neurodegenerative diseases, more research is required to better understand and control these processes.

1.1. THE CENTRAL NERVOUS SYSTEM

In higher vertebrates, the central nervous system (CNS) forms a bilateral and symmetrical, highly specialized complex that comprises of the brain and the spinal cord. While the spinal cord is the most caudal part of the CNS and responsible for the transduction of sensory information from the body to the brain and vice versa, the brain exerts a tremendous number of tasks that include, but are not limited to – memory, sensation, communication, and movement [1]. It is believed that the ability to quickly process and interpret sensory information provides an evolutionary advantage to the organism by facilitating a better adaption and response towards environmental challenges [2]. In this regard, the human brain presumably represents the most complex organ found in nature and its structure can be subdivided into seven major parts, i.e. the medulla oblongata, pons, cerebellum, midbrain, diencephalon, and cerebrum. The cerebrum is composed of two hemispheres that each contain an outside layer, the cerebral cortex, and three subjacent structures: the basal ganglia, the hippocampus, and the amygdaloid nuclei [3].

Given its importance, the CNS is particularly protected in mammals. While the brain resides in the cranial cavity of the skull being secured from physical damage, the spinal cord extends through the spinal canal of the vertebral column beginning with cervical vertebrae at the neck and terminating in the sacral region [4].

1.1.1. BARRIERS OF THE CENTRAL NERVOUS SYSTEM

In addition to the protection offered by the skull and spine, the CNS is guarded by specialized blood vessels of the blood-brain barrier (BBB) and the blood-cerebrospinal fluid barrier (BCSFB), and a series of distinct membrane layers that form the meninges. Together, these physical and vascular barriers shield the brain from entering pathogens and other exogenous threats, such as blood-borne toxic metabolites.

1.1.1.1. MENINGES

In mammals, the spinal cord and brain are sheathed by three protective membranes, collectively named the meninges: the dura mater, arachnoid mater, and pia mater [5, 6] (Figure 1). The dura mater represents the outer meningeal membrane with close proximity to the inner skull and is composed of the periosteal and the meningeal layer. The dura mater is a thick membrane, highly innervated and vascularized [7]. For example, it harbors the dural venous sinuses that collect blood flowing from the brain to the heart, but also lymphatic vessels that run along the dural sinuses and the middle meningeal artery [8, 9]. Importantly, blood vessels of the dura mater contain capillary segments and postcapillary venules that are fenestrated and mostly lack tight junctions, i.e. zipper-like structures formed between neighboring cells that exclude any extracellular space by forming protein complexes of membrane, cytoplasmic, and cytoskeletal proteins [4, 10, 11]. Therefore, the dura vessels are permeable for blood-derived molecules up to 45 kilodalton (kDa) and immune cells, such as innate lymphoid cells, dendritic cells, macrophages, and T cells [7]. The dura envelops the middle meningeal layer, the arachnoid mater, which in combination with the pia mater forms the leptomeninges. The arachnoid mater is characterized by a spider web-like structure of delicate trabeculae that project onto the pia mater (Figure 1). The subarachnoid space is a cavity filled with the cerebrospinal fluid (CSF) and comprising of leptomeningeal blood vessels [4]. In addition, the outer cell layer of the arachnoid mater forms an impermeable barrier that restricts the free diffusion of blood-derived molecules from the fenestrated vasculature of the dura mater into the CSF [7]. For that reason, arachnoid barrier cells express the tight junction proteins Claudin-11 and E-Cadherin but also a variety of efflux and solute transporters that participate in the solute clearance out of the CSF [12]. Finally, the pia mater is the innermost meningeal membrane composed of a single fibroblast layer in close proximity to the glia limitans of the brain parenchyma [12] and similar to the dura mater, the pia mater is highly vascularized. However, pial blood vessels express tight junction proteins

Occludin and Claudins in addition to adherens junctions, and thus establish a semipermeable barrier that regulates the free movement of immune cells but allows the CSF to enter perivascular spaces of brain-penetrating arteries [4, 12, 13].

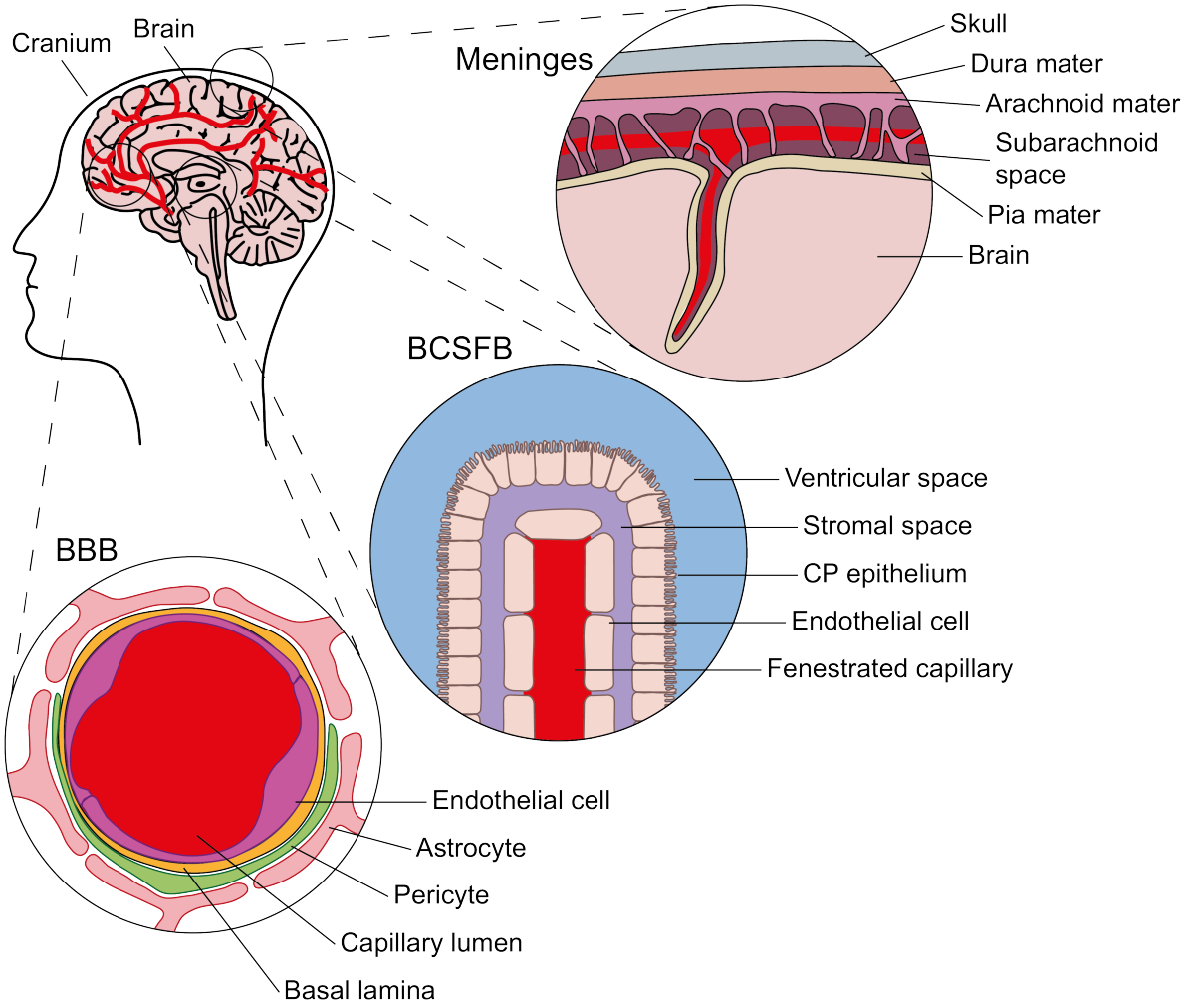

Figure 1: Barriers of the CNS.
The brain is an exceptional organ that requires a particular protection. In addition to the skull, the brain is guarded by the distinct membrane layers of the meninges, and the specialized vasculature of the BBB and the BCSFB. The meninges comprise of the dura mater and leptomeninges that are formed by the arachnoid and pia mater. In addition to lymphatic vessels, the dura mater contains fenestrated blood vessels permeable for blood-derived molecules and immune cells. The arachnoid mater is characterized by a spider web-like structure that projects onto the pia mater thereby shaping the subarachnoid space, which is filled with the CSF. The pia mater is the innermost meningeal membrane and in close proximity to the glia limitans of the brain parenchyma. The BBB is responsible for the maintenance of a homeostatic brain microenvironment and is formed by a continuous layer of specialized endothelial cells sealed by tight junctions. Capillary vessel walls closely interact with pericytes and are almost entirely covered by astrocytic end-feet to further fortify the barrier. The BCSFB represents a highly vascularized, secretory tissue formed at the Choroid Plexus in all brain ventricles. The BCSFB is key producer of the CSF, which nourishes the brain, provides buoyancy, and acts as a fluid cushion to protect the brain from injury. (adapted from [4, 14, 15])

Even though the meninges are meant to prevent pathogens from entering the brain, they themselves are not immune to infection. For example, viruses and bacteria can induce meningitis,

which is driven by resident meningeal immune cells and infiltrating leukocytes and often results in acute and long-term neurological impairments [12]. Furthermore, the meninges have been shown to play an important role in the course of multiple sclerosis (MS) and experimental autoimmune encephalomyelitis, providing an entry site for autoreactive effector T cells and B cells on their way to the brain parenchyma [12].

1.1.1.2. THE BLOOD-BRAIN BARRIER

Along with the meningeal membrane layers, the protection and homeostasis maintenance of the CNS is mediated by the BBB. As the proper function of neurons within the brain is dependent on a specific, highly regulated microenvironment, the BBB which is formed by a specialized microvasculature ensures the optimal chemical composition of the brain parenchyma [16] (Figure 1). For that reason, BBB endothelial cells limit movement of neurotoxic plasma molecules and cells between the blood and the brain [4, 17, 18], while further providing energy substrates in form of glucose and oxygen to meet the brain's high energy consumption [19].

The unique properties of the BBB rely on its microvasculature that is formed by a continuous layer of specialized endothelial cells tightly sealed by tight junctions. For example, endothelial cells of the BBB express the tight junction proteins zonula occludens-1 (ZO-1), Claudin-1, -3, -5, -12, and Occludin [16, 20–22]. At the capillary level, blood vessels closely interact with pericytes that can induce the expression of barrier-specific genes in endothelial cells, such as transferrin receptor or excitatory amino acid transporter (EAAT) 3 gene expression [23]. Furthermore, both arteriolar and capillary vessel walls are almost entirely covered by astrocytic end-feet [24], fortifying the barrier function via the induction of the Sonic hedgehog signaling pathway in endothelial cells [18, 24, 25]. Next to the variety of tight junction proteins, endothelial cells of the BBB express a range of different transporters, receptors, and ion channels to orchestrate the bi-directional exchange of molecules between blood and brain. This includes carbohydrate transporters, substrate-specific carriers, and adenosine triphosphate (ATP)-binding cassette transporters for an active efflux of substrates from brain to blood [18]. In addition, the interconnection of neurons, astrocytes, cells of the BBB (endothelial cells, myocytes, pericytes) and extracellular matrix components within the so-called neurovascular unit is able to control the vasodilation of cerebral arteries, arterioles, and capillaries in order to regulate the rate of cerebral blood flow and oxygen delivery to the brain [26].

In the light of the many tasks to be performed by the BBB, it becomes clear that disturbance or disruption would largely influence the CNS homeostasis. In this regard, systemic inflammation, injuries or stroke have been shown to reduce expression BBB-associated tight junction proteins Occludin and ZO-1 [27], resulting in an elevated transcellular permeability for cytokines, chemokines or immune cells from the blood the brain parenchyma [18]. Moreover, infection of BBB endothelial cells with adenovirus or West Nile virus can reduce expression [28] or cause degradation of tight junction proteins [29] while inducing C-C motif ligand 2 (CCL2) release [28, 30]. In addition, a growing body of evidence suggests the role of the BBB in neurodegenerative diseases such as Alzheimer's disease (AD) and MS. In AD patients and mouse models of AD, expression of the BBB transporter Glucose transporter 1 and the low density lipoprotein receptor-related protein 1 (LRP1) is reduced, resulting in energy deficiency of neurons and the disturbed efflux of amyloid-β from brain to blood [24]. In MS, breakdown of the BBB is associated with the expression of adhesion molecules E- and P-selectin in endothelial cells, allowing the initial capture and rolling of leukocytes in capillaries and postcapillary venules. In addition, adhesion as well as trans- or paracellular diapedesis of CNS-infiltrating leukocytes is further facilitated by endothelial expression of intercellular adhesion molecule-1 (ICAM-1) and vascular cell adhesion molecule-1 (VCAM-1), that ultimately interact with corresponding lymphocyte function-associated antigen-1 (LFA-1) and very late antigen-4 (VLA-4) expressed on autoreactive immune cells [18].

1.1.1.3. THE BLOOD-CEREBROSPINAL FLUID BARRIER

When addressing the barriers of the brain, research focus has often been laid on the BBB while paying less attention to its more permeable counterpart, the BCSFB [31] (Figure 1). Formed at the Choroid Plexus (CP), the BCSFB represents a highly vascularized, secretory tissue found within all brain ventricles [14, 32] that functions as a key producer of the CSF [31, 33]. The CSF, which nourishes the brain and contains various signaling molecules important during brain development [14], serves as a fluid cushion for the brain and spinal cord, protecting the CNS from injury [32]. Furthermore, the CSF provides buoyancy [34], thus reducing the effective weight of the human brain parenchyma from 1.5 kg to 50 g in order to shield it from being crushed by its own mass [31].

The CP is composed of polarized cuboidal epithelial cells that form a monolayer around a core of stroma cells and a capillary endothelium [14]. Different types of cell junctions between adjacent cells of the CP epithelium form the basis for the BCSFB to prevent the unregulated entry

of molecules from the systemic circulation into the CSF [14]. For example, CP epithelial cells express tight junction proteins such as Occludin, Claudins 1-6, 9-12, 19 and 22, and ZO proteins 1-3 that regulate paracellular diffusion through the BCSFB. Moreover, adherens junctions at the basolateral membrane further ensure the apicobasal polarity and cellular interaction of CP epithelial cells [33]. In addition to the CP epithelium being convoluted and protruding into the ventricular lumen, the apical surface of CP epithelial cells contains microvilli which help to extend the surface area of th CP [31, 32]

Although the CP surface extension is rather small when compared to the total surface area of the BBB, the BCSFB demonstrates a high transport rate accounting for up to 80 % of the total CSF production [31]. The fenestrated capillaries of the CP are permeable to water and small molecules up to 12 nm [14, 31], thus promoting a rapid provision of substrates to the CP stroma [32]. However, as the CSF is not simply an plasma ultrafiltrate [31], its secretion into the ventricular lumen depends on the expression of various transporter proteins by the CP epithelial cells. This includes several ion channels, aquaporin, glucose transporters, ATP-binding cassette transporters, and members of the solute carrier super-families [33]. Furthermore, sympathetic and parasympathetic innervation of the CP is thought to influence the blood flow and secretion of the CSF [14].

Ultimately, the CSF contains a range of nutrients and metabolites important for CNS functions. However, its role extends beyond a simple nourishment of the brain: The CSF is also home to hormones and signaling molecules [14]. Flowing through the interconnected network of ventricles spanning the CNS or upon entering the parenchyma via the glymphatic system, the CSF can promote long-range signaling to distinct brain regions, altogether affecting CNS development, steady state functions, and neuroinflammation [32]. In this context, the CP has been shown to release pro-inflammatory cytokines interleukin-(IL)-1β and tumor necrosis factor (TNF) into the ventricular lumen in response to administration of lipopolysaccharides (LPS), i.e. cell wall components of gram-negative bacteria, in murine models of sepsis. Simultaneously, activation of the CP further modifies its barrier integrity via downregulation of Occludin expression and upregulation of matrix metalloproteinases 8 and 9, which in turn degrade Claudin family proteins as integral components of tight junction protein complexes [11, 33]. In combination with increased expression of chemokines, such as CCL2 and C-X-C motif ligands (CXCL) 9-11 that attract blood-borne leukocytes, the CP may act as an entrance gate for immune cells into the CNS and contributor of neuroinflammation [33].

1.1.2. CELLS OF THE CNS

1.1.2.1. NEURONS AND SIGNAL TRANSDUCTION

Neurons and glia cells form the fundamental basis of the brain and are indispensable for its functionality. It is estimated that the human brain harbors up to 10^{11} neurons [35] which form neural circuits of more than 100,000 km length [2], and assumingly, this complexity of the neural circuitry plays a key role in the ability of the brain to process large amounts of sensory information [2].

Commencing in the developing mammalian brain, neuronal cells form cellular networks by giving rise to axons and dendrites, i.e. specialized cellular branches that allow the communication with other cells. Dendrites are arrays of short fibers that mediate the reception of electrochemical input signals from other neurons, whereas axons are long connecting fibers that facilitate the transmission of such signals to other cells [36] (Figure 2). By forming growth cones at their tips, axonal processes are able to elongate away from the cell soma and, when reaching a new target, a synapse is formed by the dendrite and the growing axon [37]. Synapses are specialized, asymmetric intracellular junctions that form the information-processing networks of the brain by forwarding a fast-traveling, electric intracellular signal: the action potential [3, 38]. Uniformly among various species, chemical synapses display a similar structure comprising of a pre-synaptic terminal, a post-synaptic specialization, and an interstitial space forming the "synaptic cleft" (Figure 2). Noteworthy, Cadherins and immunoglobulin-domains facilitate the tight adhesion of pre- and post-synaptic compartments, contributing to synapse formation [39, 40]. The pre-synapse contains several scaffolding proteins of the cytomatrix, e.g. Bassoon and Piccolo, that establish the molecular and structural organization of the pre-synaptic active zone [41, 42]. In addition, pre-synaptic nerve terminals harbor synaptic vesicles that fuse with the plasma membrane upon arrival of the action potential to release their content of neurotransmitters into the synaptic cleft [41]. Synaptic vesicles at the pre-synapse can be identified by several membrane proteins, such as Synaptophysin (Syp), or the vesicular glutamate transporter 1 (VGLUT1) and the vesicular γ-aminobutyric acid (GABA) transporter (VGAT), that fill the synaptic vesicles with neurotransmitters [40, 41]. At the post-synaptic neuron, the neurotransmitters bind to corresponding neurotransmitter receptors allocated and clustered at the post-synaptic density. Here, scaffolding proteins form a dense network of multi-protein complexes

in order to provide a target structure for chemical signal transduction [41]. Of note, post-synaptic scaffolding proteins located at excitatory synapses differ from those at inhibitory synapses. For example, post-synaptic density protein 95 (PSD-95), sarcoma homology 3 and multiple ankyrin repeat domains protein 2 (SHANK2), and members of the Homer protein family play an important role in promoting spine morphology, stability, and function [43]. Correspondingly, Gephyrin has been described to function as a scaffolding protein that allocates and stabilizes inhibitory synaptic receptors at the inhibitory synapse [44].

Altogether, synapses process the transmitted information during the transfer as the frequency and length of the action potential is computed into specific reactions of the post-synaptic neurons [40]. Excitatory neurotransmission is realized by binding of glutamate to ligand-gated ion channels (LGICs) such as the α-amino-3-hydroxy-5-methyl-4-isoxazolepropionic acid (AMPA)- or N-methyl-D-aspartic acid (NMDA)-receptors, allowing the rapid influx of cations into the post-synaptic neuron. Thus, its membrane potential will depolarize, bringing it closer to the threshold of firing an action potential. In contrast, fast inhibitory neurotransmission mediated by GABA binding to its $GABA_A$ receptors, which are permeable to negatively charged anions and counteract the depolarizing effects of glutamatergic signal transmission to decrease the likelihood of the post-synaptic neuron to fire an action potential [3, 38].

Besides LGICs, certain neurotransmitters can also bind to G-protein–coupled receptors (GPCRs) that transduce electrochemical neurotransmission into slower but long-lasting, intracellular biochemical responses with neuromodulatory effects [3, 38]. The neurotransmitters dopamine and serotonin signal via GPCRs and are involved in several neuronal functions. For example, dopamine has been shown to regulate reward and motivation [45, 46], whereas serotonin influences sleep, mood, aggression, and appetite [47]. After their release into the synaptic cleft, neurotransmitters are quickly removed by neurotransmitter transporters to minimize the time of interaction with neurotransmitter receptors, hence allowing short and specific synaptic signals [3, 38]. While the re-uptake of neurotransmitters may occur mainly at the pre-synaptic axon terminal, neurons are further supported by surrounding non-neuronal glia cells [3, 38]. Of note, a fine-tuned balance of excitatory and inhibitory neurotransmission is crucial for neuronal viability as the accumulation of glutamate at the synaptic cleft can result in excitotoxicity. Glutamate uptake in neurons is mediated by glutamate transporters EAAT2, and transporter expression can be disturbed by inflammation. Consequently, the impaired recovery of glutamate has been shown to be a hallmark of neurodegenerative disorders such as MS, AD, amyotrophic lateral sclerosis (ALS), and Parkinson's disease (PD) [48].

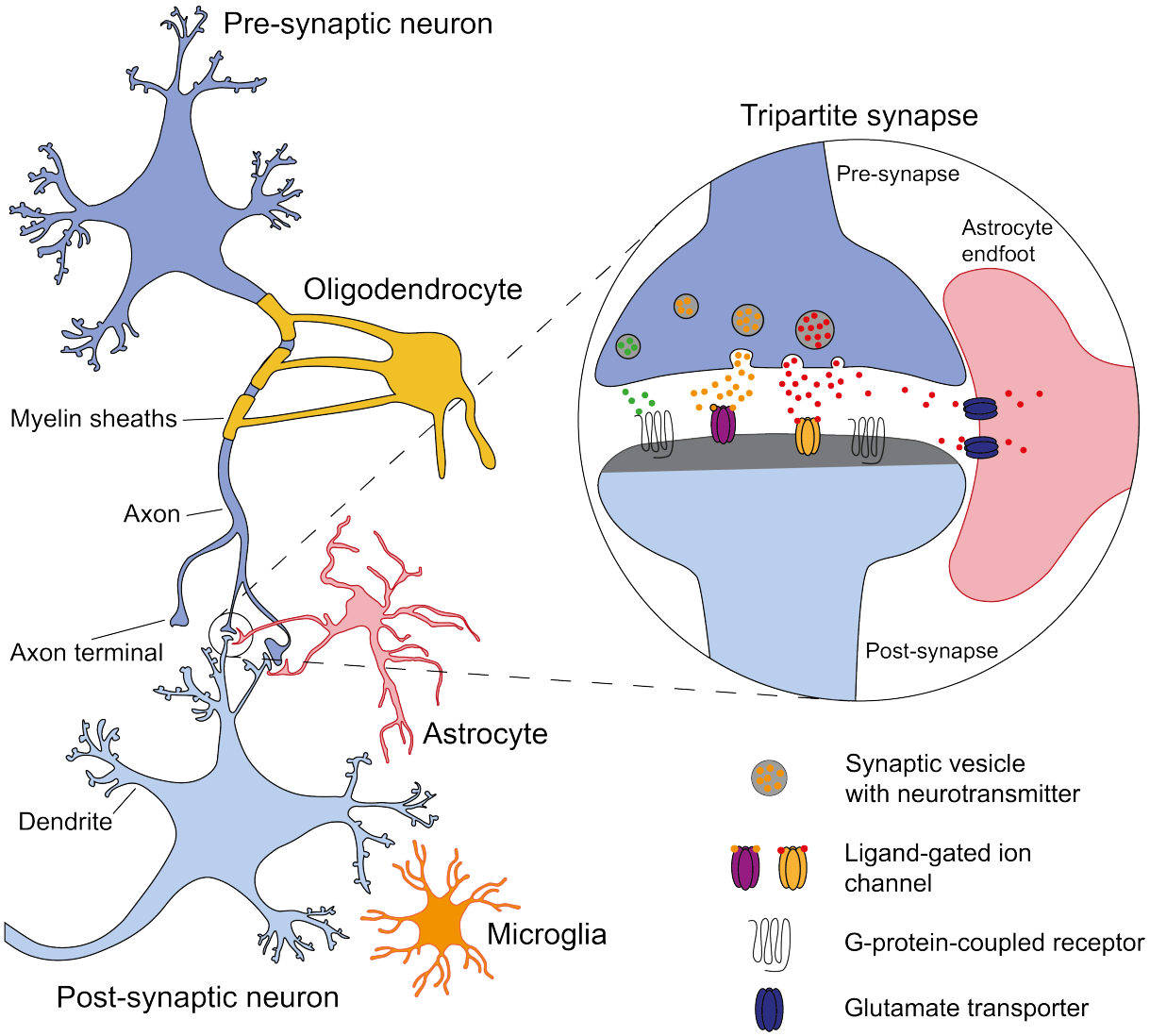

Figure 2: Cellular interactions in the CNS.
In the mammalian brain, neurons form intracellular networks via chemical synapses that allow a rapid signal transduction. Proper function of neurons is facilitated by support from different subsets of glial cells: oligodendrocytes, astrocytes, and microglial cells. While oligodendrocytes form myelin sheaths necessary for a fast conduction of neuronal action potentials, astrocytes support neurons in many ways such as by supplying nutrients, clearing of glutamate from the synaptic cleft or by releasing neurotrophic factors. Microglial cells represent the innate immune cells and macrophage population of the brain. Next to various housekeeping tasks, these cells also act as the first line of defense. The tripartite synapse describes the synapse structure formed by the pre- and post-synaptic neuron in collaboration with astrocytic end-feet. Synaptic vesicles at the axon terminal of pre-synaptic neurons are loaded with neurotransmitters. Upon release into the synaptic cleft, neurotransmitters are sensed by specific ligand-gated ion channels or G-protein-coupled receptors on the membranes of the post-synaptic neurons. Glutamate transporters on astrocytic end-feet quickly remove remaining glutamate from the synaptic cleft. (adapted from [49])

In addition to being modulated by neurotransmitter signaling, neuronal functions are further regulated by neurotrophins. Neurotrophins, or neurotrophic factors, describe a family of secreted proteins that orchestrate the development, maturation, differentiation and survival of

neurons, thus playing an essential role during the formation of the CNS [50]. The family of neurotrophins comprises of nerve growth factor (NGF), brain-derived neurotrophic factor (BDNF), neurotrophin (NT)-3, and NT-4. All neurotrophic factors are initially synthesized as precursors, i.e. pro-neurotrophins, that still contain the N-terminal domain which is subsequently cleaved to produce the mature form of the neurotrophin [51]. While all mature neurotrophins signal via their corresponding members of the tyrosine kinase receptor (Trk) family [52], pro-neurotrophins have shown a high affinity towards the p75 neurotrophin receptor ($p75^{NTR}$) [50]. The important roles of mature NGF (mNGF) and mBDNF have been extensively studied over the last decades and highlighted their effects not only on brain development and neuronal survival, but also on nociception (mNGF) [53] or promotion of glutamate release while reducing $GABA_A$-mediated signaling in the CNS (mBDNF) [52]. In contrast, pro-neurotrophin signaling via the $p75^{NTR}$ has been demonstrated to elicit apoptosis [54] and expression of the receptor in the adult brain is associated with neuronal damage or degeneration [55]. Although pro-neurotrophin-mediated effects as a whole have yet not been fully elucidated, recent data indicate that pro-neurotrophins furthermore regulate excitability of neurons [56] and a dysbalanced neurotrophin/pro-neurotrophin ratio is assumed to play a role in major depression [57, 58].

1.1.2.2. OLIGODENDROCYTES

Despite neurons often being recognized as the most important cells of the brain, their function highly relies on the metabolic and functional support by glial cells and for this reason, the ratio of neurons:glia cells in human brains is estimated to be approximately 1:1 [59]. Oligodendrocytes represent a subset of these glia cells and their key feature is the insulation of neuronal axons by forming the multispiral membrane myelin [60, 61].

Oligodendrocytes derive from a population of self-renewing oligodendrocyte progenitor cells that remains persistent throughout life, allowing the maintenance of myelin plasticity or reaction to damage [62]. During brain development, oligodendrocytes extend their processes towards nearby axons to generate lipid-rich myelin sheaths, which enable the fast conduction of neuronal action potentials [3, 36, 60] (Figure 2). The myelin sheaths represent structures of compacted cytoplasmic membranes that contain high levels of saturated, long-chain fatty acids, glycosphingolipids, and cholesterol. The compaction of lipid bilayers is facilitated by myelin basic protein, which tightly binds two adjacent cytosolic membrane surfaces together upon its

self-polymerization. To support efficient diffusion of metabolites with the myelin sheaths, oligodendrocytes form gap junctions that are permeable to ions and small molecules [63].

Of note, the role of oligodendrocytes has recently been shown to encompass more functions than simply insulating axons. For example, oligodendrocytes contribute to ion homeostasis by providing a large number of potassium channels underneath the myelin sheaths [17] and furthermore, they release trophic factors, e.g. ciliary neurotrophic factor and insulin-like growth factor-1, being important for neuronal survival and axonal integrity [36, 64]. Overall, our current understandings highlight the important role of oligodendrocytes in mammalian brains in facilitating circuit function, and loss of oligodendrocytes or demyelination of grey and white matter in the CNS are hallmarks of neurodegenerative diseases such as MS [63, 65]. Here, MS lesion formation is mediated by cells of the adaptive immune system, including B and T cells reactive to myelin antigens. Myelin loss is accompanied by impaired axonal transport, sensory loss and limited mobility [65].

1.1.2.3. ASTROCYTES

Astrocytes represent another subset and the largest fraction of glia cells [59]. They are characterized by a star-shaped morphology with various thin processes that form a close connection to virtually all cell types within CNS and, more importantly, to synapses [3, 17, 66].

Synaptogenesis describes the process of synapse formation and maintenance and is one hallmark of brain development. During synaptogenesis, proliferating astrocytes seed across parenchyma while promoting the generation of new glutamatergic, GABAergic, and cholinergic synapses by neurons via the release of synapse-modifying signals, including thrombospondin and transforming growth factor-β [3, 17, 67, 68]. Synapses are then further strengthened and stabilized, or alternatively negatively regulated by additional mediators released by astrocytes [17]. Moreover, astrocytes are capable of eliminating weak or excessive synapses at the end of synaptogenesis through multiple Epidermal Growth Factor-like domains 10-, apolipoprotein E-, and glial Mer receptor tyrosine kinase-driven phagocytic pathways [17, 69, 70].

In the adult brain, astrocytic execute numerous tasks that range from the support of neurons with nutrients and metabolites to the regulation of blood flow through their interaction with endothelial cells of the BBB [71] (Figure 1). They maintain synaptic signal transduction by perpetuating the homeostatic concentration of the neurotransmitters via glutamate transporters EAAT1 and EAAT2 on their cell membranes [72], allowing a rapid uptake of glutamate from

the synaptic cleft and preventing excitotoxicity of neurons [3, 17] (Figure 2). Subsequent to glutamate uptake, astrocytes can convert glutamate to glutamine which is then transferred back to neurons to serve as a precursor of glutamate [3]. Interestingly, astrocytes themselves express neurotransmitter receptors, such as AMPA [3] or GPCRs, which not only sense neuronal activity but induce intracellular Ca^{2+} signaling pathways [73]. Moreover, astrocytes carry antioxidant mechanisms to protect neurons from oxidative damage caused by reactive oxygen species (ROS) as metabolic by-products of high energy production [71]. Astrocytes are further capable of releasing BDNF, which modulates synapse transmission [70] as well as the development and survival of neurons [3].

As important astrocyte function is for maintaining the steady state of the brain, their dysfunction has been described as contributing factors to various neurodegenerative diseases including AD [74], PD, and ALS [75]. During inflammatory conditions, reactive astrocytes can be characterized by hypertrophy and the release of pro-inflammatory mediators, e.g. IL-1β, IL-6, TNF [75], and complement factors [76]. While the morphological change of astrocytes further results in diminished synaptic contacts, disturbed synaptic functions [75], and impaired glymphatic functionality [77], the reported impairment in glutamate removal from synaptic clefts causes additional neuronal death via excitotoxicity during progression of AD [74].

1.1.2.4. MICROGLIA AND FUNCTION

Although microglial cells are typically coined as the brain-resident macrophages, they are not of neuroectodermal but hematopoietic origin and derive from erythromyeloid progenitor cells of the extra-embryonic yolk sac during embryogenesis [78, 79]. Upon arrival in the brain, microglial progenitor cells spread across the entire parenchyma where they remain as a long-lived, self-renewing population throughout life [17, 80, 81]. Here, they are in charge of brain homeostasis and synaptogenesis.

In the developmental brain, microglia play an important role during the establishment of the neuronal architecture, as they efficiently engulf dead or excessive cells [81, 82] or limit neuron numbers by phagocytosing neural precursor cells [17, 80]. In the adult brain, microglia are spatially distributed within the parenchyma and form a tile-like network of cells that display a highly ramified morphology with numerous thin processes, continuously scanning their surrounding environment [79, 83, 84] while closely interacting with synapses [85, 86] (Figure 2). Thereby, microglia have been shown to actively contribute to learning and memory in the CNS

by refinement of neuronal circuits [80, 81] or strengthening of synapses via the release of BDNF, an important regulator of synaptic plasticity [87]. In order to detect disturbances in the CNS homeostasis, microglia express a set of receptors to recognize chemokines, cytokines [79], or subtle changes in their chemical microenvironment, such as release of ATP by dying cells [88]. Furthermore, microglia express the fractalkine receptor C-X_3-C motif receptor 1 (CX_3CR1) that binds to neuronal C-X_3-C motif ligand 1 (CX_3CL1, fractalkine) and promotes microglial chemotaxis [69, 89].

In addition, microglia harbor the complement receptor 3 (CR3), which represents an important mediator of synapse removal by phagocytosis, a process also referred to as synaptic pruning. Microglia-mediated synaptic pruning has been shown to be essential for the maturation of synaptic inputs [69] and relies on the mechanisms of the classical component pathway: On the one hand, synapses and neurons that expose phosphatidylserine become tagged by complement components C1q and C3, which then act as "eat-me" signals for microglial cells [17, 69, 89]. On the other hand, neuronal expression of the CD47 receptor, which inactivates microglia by binding to signal regulatory protein-α, acts as a "don't-eat-me" signal shown to protect tagged synapses from phagocytosis [89, 90].

Hence, it becomes evident that the appropriate development of a complex structure such as the brain relies on a fine-tuned process of synaptic pruning. Indeed, previous studies have shown that aberrant or insufficient removal of synapses is associated with neurodevelopmental disorders such as autism spectrum disorder (ASD), schizophrenia, and epilepsy [69]. For example, previous studies indicated that reduced elimination of post-synaptic spines is a feature of ASD, whereas schizophrenia correlates with excessive phagocytosis of mature synapses [91, 92].

Finally, as the major parenchymal-resident immune cell population in the brain, microglia also represent the first line of defense in the CNS. To this end, microglia are able to detect pathogen-associated molecular patterns and endogenous danger signals via a set of pattern recognition receptors (PRRs) such as nucleotide-binding oligomerization domain (NOD)-like receptors, triggering receptor expressed on myeloid cells (TREMs), and toll-like receptors (TLRs) [93]. Binding of ligands to these receptors results in a swift activation of microglia that undergo a morphological change by retracting their processes and becoming more amoeboid and migratory [94]. Furthermore, these cells orchestrate neuroinflammation by the release of cytokines, e.g. IL-1β, IL-6, TNF [79], ROS and nitrogen species (NOS), and chemokines that attract peripheral immune cells to the site of inflammation [93, 94]. Although acute inflammation of the

CNS driven by activated microglia may be deleterious, it has been described as a physiological response with tight regulation and repair mechanisms. However, prolonged activation of microglia is thought to result in reoccurring synaptic pruning as the ability of microglia to differentiate between live and dead neurons was found to be impaired [89]. Moreover, microglia-released ROS are toxic to neurons and induce inflammatory stress in these cells, which in turn expose more phosphatidylserine to become tagged for pruning by complement factors [89, 92]. As microglia activation is considered a hallmark of several neuropathologies such as AD [95] and PD [96], the role and function of microglia in neurodegeneration has been extensively studied [79, 97].

1.1.3. IMMUNOSURVEILLANCE OF THE CNS

For many decades, the CNS was considered as an immune-privileged site, shielded by its barriers and only equipped with parenchymal microglia as tissue-resident immune cells. The presence of peripheral leukocytes was perceived as a pathological consequence of acute inflammatory responses within the CNS or neurodegenerative diseases, and thus considered detrimental [77, 98]. Over the last years, several discoveries have helped to change this narrative and contributed to an evolved understanding of the immunosurveillance of the CNS: While the brain parenchyma is indeed restricted to peripheral immunity during steady state, the CNS border regions harbor a broad range of peripheral immune cells contributing to homeostasis but also mediating protection against pathogens. For example, the dural and subdural meninges, CP, and perivascular space have been shown to be constantly populated by border-associated macrophages (BAMs), T and B cells, mast cells, monocytes, natural killer cells, innate lymphoid cells, dendritic cells, and granulocytes etc. [77, 99]. Of note, the distribution of immune cells across the CNS border regions is heterogeneous, given that specific subsets patrol or reside at preferred locations, such as the perivascular spaces being mostly occupied by mast cells and BAMs [100]. Furthermore, as the CSF is drained to the deep cervical lymph nodes via the lymphatic vasculature of the meninges [4], it is constantly sampled [77]. Therefore, the meninges serve as a crucial neuro-immunological interface at which blood-borne T cells may circulate and interact with antigen-presenting cells [98] to constantly surveil the brain for pathological content in order to maintain homeostasis [100].

Besides exerting a protective role, peripheral immune cells in the healthy CNS have been shown to be important for normal brain function. Although the full extent of immune-CNS interaction

is not entirely elucidated, previous studies have shown the beneficial effects of B cells in promoting oligodendrogenesis and myelination of axons during brain development [101]. In addition, interferon (IFN)-γ and IL-4 derived from meningeal T cells affect social behavior [102] as well as learning and memory [103], suggesting a strong connection between meningeal immunity and neuronal function. Hence, the homeostasis of the CNS is achieved by a balance between a regulated immune cell activation and pathogen control that, if disturbed, may result in pathology and tissue damage, as seen in MS. Here, the interplay of various immune cell subsets, including autoreactive T and B cells, as well as monocytes and macrophages has been shown to drive neuroinflammation and -degeneration [98]. Yet, in other neuropathologies adaptive immunity has been shown to exert protective effects, such as enhancing microglial phagocytosis of amyloid-β via cytokine and chemokine release in murine models of AD [104] or providing supportive neuroprotection in ALS [105]. In addition, CNS-specific, IFN-γ-releasing $CD4^+$ T cells were described to orchestrate the infiltration of monocytes into the brain parenchyma through the CP upon brain injury [106]. Furthermore, the CP's structural permissiveness for transepithelial leukocyte trafficking [107] provides an educative gate for these recruited monocytes, that locally differentiate to macrophages while acquiring an anti-inflammatory phenotype [106] and assist microglia in clearance of debris form the damaged CNS [108].

1.2. INFLUENZA A VIRUS INFECTIONS

Infections with influenza viruses in humans accumulate in annual epidemics, i.e. "influenza seasons", with up to 50 million cases in the European Union [109], thus representing a significant cause for morbidity and mortality [110]. Influenza viruses belong to the family of *Orthomyxoviridae* [111] that comprises of the types A, B, C, and D [112] with influenza A virus (IAV) and influenza B virus representing the predominant circulating genera during the influenza season 2019/20 in Germany [113]. In addition to epidemics, influenza viruses are able to cause pandemics, however all pandemics within the last century were induced by different variants of IAV.

IAV is an enveloped single-stranded, negative-sense ribonucleic acid (RNA) virus with a genome segmented into 8 viral molecules organized into ribonucleoproteins. The viral genome segments encode for subunits of the RNA polymerase, the viral glycoproteins haemagglutinin (HA) and neuraminidase (NA), viral nucleoprotein (NP), the matrix protein and membrane protein, the non-structural protein 1 (NS1), and nuclear export protein [112, 114]. Typically,

variants of IAV are subtyped based on the antigenic properties of the surface proteins HA and NA, important mediators of viral tropism and release of new virions from the host cell [114]. In humans, IAV mainly infects bronchial epithelial cells of the upper respiratory tract by binding of HA to glycoproteins with terminal α-2,6-linked sialic acid [114]. Upon its release into the cytoplasm, transcription and replication of viral RNA occur in the nucleus of the host cell, whereas translation of the resulting messenger RNAs (mRNAs) into viral proteins takes place in the cytosol. Finally, new virions assemble from newly formed viral ribonucleoproteins, viral transmembrane proteins, and the host cell membrane. The release of IAV particles results in cell death and is mediated by NA-dependent cleavage of remaining sialic acid residues on the plasma membrane in order to prevent the retention of new virions at the cell surface [112, 114].

An important feature of influenza viruses is their ability to evade pre-existing immunity in humans by introducing point mutations into their genome as a consequence of an absent proofreading mechanism during RNA replication. Eventually, changes in the amino acid sequences of HA and NA alter the antigenic properties of new viruses to bypass an antibody-mediated immunity, thus being the causative of seasonal epidemics [114, 115]. Moreover, as IAV has a large reservoir of species and can circulate in humans, pigs or migratory birds [112], substantial changes in the viral epitope may arise from antigenic shift: In cells simultaneously infected with different virus strains, reassortment of IAV genome can occur due to its segmented nature, thereby leading to the emergence of a new pandemic subtype [114, 115].

1.2.1. IMMUNE RESPONSE TO IAV INFECTIONS

In order to infect and replicate within host cells, IAV first has to overcome the host's innate and adaptive immune system. As a first barrier, the epithelial cells of the upper respiratory tract are covered with viscous mucus, which traps IAV with its high amount of glycosylated proteins. Mucociliary clearance then removes the virus before it can infect the underlying cells [116]. In addition, a set of PRRs consisting of TLRs, retinoic acid inducible gene (RIG)-I, and the nucleotide-binding domain, leucine-rich repeat family, pyrin domain-containing 3 (NLRP3), is capable of sensing viral RNA, thereby facilitating the release of cytokines and chemokines to recruit innate immune cells, to induce an antiviral state, and to regulate adaptive immunity [116, 117]. The group of TLRs to recognize either double-stranded or single-stranded RNA comprises TLR3, TLR7, and TLR8 and their activation results in downstream induction of the transcription factors nuclear factor-κB (NF-κB) and interferon regulatory factors (IRFs) 3 and 7

[116, 117]. Upon sensing cytosolic viral RNA, RIG-I-mediated activation of the mitochondrial antiviral-signaling protein (MAVS) also leads to NF-κB and IRF3 pathway induction, culminating in the release of pro-inflammatory cytokines IL-1β, IL-6, IL-8, IL-12, TNF, and type I IFNs [116, 117]. In addition, the release type I IFNs mediates the expression of a plethora of IFN-stimulated genes (ISGs) that limit viral replication and promote an immune alertness in neighboring cells [117]. Furthermore, the presence of cytosolic viral RNA can trigger the formation of NLPR3 inflammasome in bronchial epithelial cells, which results in the secretion of IL-1β and IL-18 but also elicits pyroptosis [117].

Eventually, the replication and spread of IAV in the respiratory tract leads to the recruitment and activation of innate immune cell subsets, such as monocytes, macrophages, neutrophil granulocytes, natural killer T cells, and mucosal-associated invariant T cells [110]. In turn, these cells release pro-inflammatory cytokines that attract other leukocytes and enhance activity of antigen-presenting cells [118]. As a result, the early innate immune response transits to an adaptive immune response promoted by T cell-mediated and antibody-mediated humoral immunity. On the one hand, virus-specific $CD4^+$ helper T cells and $CD8^+$ cytotoxic T cells are important producers of pro-inflammatory IFN-γ and regulatory IL-10, but also necessary for the direct elimination of virus-infected cells [112, 118]. Furthermore, $CD4^+$ helper T cells facilitate the formation and maintenance of long-lived $CD8^+$ memory T cells that provide heterosubtypic immunity to future influenza virus infection as they preferentially recognize epitopes of more conserved internal viral proteins presented via MHC class-I molecules [110, 118]. On the other hand, the activation of B cells and induction of the germinal center reaction in secondary lymphoid organs results in the generation of long-lived plasma cells that secrete large amounts of virus-neutralizing antibodies. In addition, the emergence of memory B cells provides long-term protection against re-infection with the virus [119, 120]. However, the released antibodies mainly target viral HA and NA and may lose specificity to new IAV variants as antigenic drift particularly affects the head domain of HA. Thus, individuals may acquire several influenza infections throughout life [112].

1.2.2. INFECTION-INDUCED BEHAVIORAL AND NEURONAL ALTERATIONS

In infected hosts, the initiation of an anti-viral immune response is often accompanied by systemic responses and symptoms that include fever, nausea, fatigue, reduced social interactions, anorexia, and weight loss [121, 122]. In the past, these alterations have been coined with the

term “sickness behavior” and were demonstrated to be a consequence of pyrogenic cytokines (IL-1β, IL-6, and TNF) released by activated immune cells during the acute phase response [121, 123]. Although it has become clear that this response is carefully regulated in order to adjust both systemic metabolism and immunometabolism to impair replication of the pathogen [122], the complete process of afferent immune-to-brain signaling has not been fully understood. In this context, important roles were ascribed to the circumventricular organs (CVOs) of the CNS, the vagus nerve, and endothelial cells of the BBB [123, 124]. CVOs are densely vascularized regions of the brain that lack of a functional BBB [125, 126]. Thus, CVOs were described as the sensory organs of the brain as their resident sensory neurons can become exposed directly to circulating cytokines which then are transduced into neuronal signals [123, 125]. In addition, the vagus nerve as the major afferent pathway was shown to be an important component of the neuro-immune communication owning to its capability to sense peripherally produced cytokines [121]. Furthermore, several studies have illustrated the role of endothelial cells of the BBB in response to circulating cytokines in the bloodstream: On the one hand, endothelial cells express transporters to convey blood-borne cytokines into the brain parenchyma [126, 127]. On the other hand, pyrogenic cytokines stimulate the BBB endothelium to produce and release prostaglandin E2 into the brain [121, 122], a critical mediator of fever and sickness behavior that may further promote the production of inflammatory molecules by microglia and astrocytes [124].

In consideration of infection-induced behavioral alterations and disturbance of brain homeostasis, it has been proposed that systemic inflammation may precede the onset of neurological disorders such as depression [128]. Of note, the risk of developing depression is increased upon IAV infection [129] and various experimental studies in animals have described morphological differences in microglial cells, neuronal alterations, increased expression of inflammatory cytokines, and impaired cognition in mice upon influenza infection [130, 131].

1.3. AIMS OF THIS STUDY

Influenza A virus represents a dominant fraction of the current variants of circulating influenza that can cause annual epidemics and even pandemics. Infections with IAV affect all age groups and are mainly restricted to the respiratory tract. Despite cough and fever represent typical symptoms of IAV infection, they also correspond to sickness behavior. In line, previous experimental animal studies have indicated an effect of IAV infection on CNS homeostasis. Yet, the role of microglia activation as well as the underlying processes of behavioral alterations remained unaddressed. Moreover, the IAV strains utilized in previous experiments either show low prevalence or neurotropic features.

Hence, this study utilized a low-dose infection with a non-neurotropic IAV strain that mimics the disease progression in humans to:

1. Characterize microglial cell activation and expression of activation-induced genes in the cortex and hippocampus at different time points after IAV infection.
2. Obtain profound knowledge on neuronal alterations at the synapse level.

2. MATERIALS AND METHODS

2.1. MATERIALS

2.1.1. TECHNICAL EQUIPMENT

Table 1: List of technical equipment

Equipment	Model	Manufacturer
-20 °C freezer	profi line	Liebherr, Germany
-80 °C freezer	HERAfreeze	ThermoFisher Scientific, Germany
Analytical balance	A120S	Sartorius, Germany
Autoclave	VX-65	Systec, Germany
Balance	MXX-5001.3	Denver Instruments, USA
Benchtop centrifuge	Hettich 1000	Hettich, Germany
Benchtop centrifuge	accuSpin Micro 17R	Thermo Scientific, Germany
Benchtop centrifuge	Ministar	VWR, Germany
Benchtop homogenizer	BeadBug 6	Benchmark Scientific Inc., USA
Benchtop tissue processor	TP1020	Leica, Germany
Biological safety workbench	Safe 2020	ThermoFisher Scientific, Germany
Centrifuge	Megafuge 40R	ThermoFisher Scientific, Germany
Cryostat	CryoStar™ NX50	ThermoFisher Scientific, Germany
Drilling machine	SBE 2000	Metabo, Germany
Drying Cabinet	400	Memmert, Germany
Flow cytometer	FACS Canto II™	BD Biosciences, Germany
Flow cytometer	LSR Fortessa	BD Biosciences, Germany
Flow cytometer with autosampler	Attune NxT	ThermoFisher Scientific, Germany
Gel electrophoresis power supply	Power Pac 200	Bio-Rad, Germany
Gel electrophoresis system	Mighty Small™ II	Hoefer Inc., USA
Gel electrophoresis transfer cell	Trans-Blot SD	Bio-Rad, Germany
Ice machine	AF 103	Scotsman Ice System, Italy
Imaging system	ChemiDoc XRS+	Bio-Rad, Germany
Magnetic stirrer	RCT	IKA®-Werke, Germany

Equipment	Model	Manufacturer
Microplate reader	SpectraMax M5	Molecular Devices LLC., USA
Microscope	Axiovert 200	Zeiss, Germany
Microscope	TSC SP8	Leica Microsystems, Germany
Microscope	Olympus VS120	Olympus Life Science, USA
Microtome	HM 355S	ThermoFisher Scientific, Germany
PCR workbench	UVC/T-M-AR	Kisker Biotech, Germany
pH meter	SevenEasy	Mettler Toledo,Germany
Real-Time PCR	LightCycler 96®	Roche, Germany
Refrigerator	MediLine	Liebherr, Germany
Shaker	DOS-10L	neoLab®, Germany
Spectral flow cytometer	Sony SP6800	Sony Biotechnology, USA
Spectrophotometer	NanoDrop 2000	ThermoFisher Scientific, Germany
Standing centrifuge	Avanti J-E	Beckman Coulter, USA
Stereo microscope	Stemi 305	Zeiss, Germany
Thermomixer	Comfort	Eppendorf, Germany
Transmission electron microscope	LEO 912	Carl Zeiss, Germany
Ultracentrifuge	Sorvall WX+	ThermoFisher Scientific, Germany
Ultracentrifuge rotor	TH-660	ThermoFisher Scientific, Germany
Ultramicrotome	Ultracut E	Reichert-Jung, Germany
Vortexer	VF2	IKA®-Werke, Germany
Water purification system with electrodeionization	Integral 10	Merck, Germany
Waterbath	1083	GFL, Germany

2.1.2. LABORATORY UTENSILS

Table 2: List of laboratory utensils

Utensils	Manufacturer
96-well plate (flat-bottom)	Greiner bio-one, Germany
96-well plate for LC480	Biozym, Germany
Adhesive clear qPCR seal	Biozym, Germany
Aluminum foil	Carl Roth, Germany
Autoclave bags	Carl Roth, Germany
Cannulas 18G, 20G, 22G, 26G	Braun, Germany
Cell strainer 70 µm	BD, Germany
Centrifugation tube 15/50 ml	Greiner bio-one, Germany
Coverslips 22x22 mm	Carl Roth, Germany
Dounce homogenizer 17 ml, “Elvehjem” Size 23	Kontes Glass Co., USA
Dounce homogenizer 2 ml	Sartorius, Germany
Dounce homogenizer 7 ml, “Tenbroeck”	Kontes Glass Co., USA

Utensils	Manufacturer
Flask 50, 100 ml	Schott, Germany
Gloves	Ansell, Malaysia
Ice bucket	Sigma-Aldrich, Germany
Microliter syringe	Hamilton Bonaduz AG, Switzerland
Mortar and pestle (porcelain, glazed)	Carl Roth, Germany
Mr. Frosty™ freezing container	Thermo Scientific, Germany
Multi-channel pipette	Eppendorf, Germany
Neubauer counting chamber	Marienfeld Superior, Germany
Nitrocellulose membrane Protran 0.45 µm	GE Healthcare, USA
Parafilm "Nescofilm"	Alfresa Pharma corp., Japan
Pasteur pipette	Brand, Germany
Peel-A-Way® embedding molds	Sigma-Aldrich, Germany
Petri dishes	Greiner bio-one, Germany
Pipettes 2.5, 10, 20, 100, 200, 1000, 5000 µl	Eppendorf, Germany
Pipetting aid "accu-jet® pro"	Brand, Germany
Reaction tube holder	Carl Roth, Germany
Round-bottom polystyrene test tubes 5 ml	Corning Life Sciences, Germany
Safe-lock tube 1.5 ml	Sarstedt, Germany
Safe-lock tube 2 ml	Eppendorf, Germany
Scalpel	Feather, Japan
Serological pipettes 10/25 ml	Greiner bio-one, Germany
SuperFrost Plus™ slides	Thermo Scientific, Germany
Surgical instruments	Fine Science Tools, Germany
Syringe-driven 0.22 µm sterile filter	Merck, Germany
Syringes 1, 20 ml	BD, Germany
Ultracentrifugation tubes 5 ml	Sorvall Instruments, USA
Vacutainer	BD, Germany
Vein catheter "Insyte Autoguard"	BD, Germany

2.1.3. CHEMICALS AND COMPOUNDS

Table 3: List of chemicals and compounds

Chemical	Company
10X Zinc Fixative (formalin free)	BD Pharmingen™, Germany
30 % acrylamide/bisacrylamide Rotiphorese® Gel 30 (37.5:1)	Roth
Acetic acid	Carl Roth, Germany
Amersham Low Molecular Weight calibration kit	GE Healthcare, USA
Ammoniumperoxodisulfate	Honeywell Fluka™, USA
Attune 1X focusing fluid	ThermoFisher Scientific, Germany
Attune 1X shutdown solution	ThermoFisher Scientific, Germany

Chemical	Company
Attune 1X wash solution	ThermoFisher Scientific, Germany
BashingBeads lysis tubes	Zymo Research, Germany
BioWhittaker® 10X PBS without Ca^{2+}/Mg^{2+}	Lonza, Germany
Bovine serum albumin (BSA)	Sigma-Aldrich, Germany
Bromophenol blue	Sigma-Aldrich, Germany
Citric acid	Carl Roth, Germany
cOmplete™, EDTA-free Protease Inhibitor Cocktail	Sigma-Aldrich, Germany
Dimethyl sulfoxide	Carl Roth, Germany
DPBS with Ca^{2+}/Mg^{2+}	Gibco, Germany
Dulbecco's phosphate-buffered saline (DPBS), without Ca^{2+}/Mg^{2+}	Gibco, Germany
Durcupan ACM	Honeywell Fluka™, USA
Epredia™ Histoplast Paraffin	Fisher Scientific, Germany
Ethanol (EtOH) 96 %	Fischar, Germany
Ethylenediaminetetraacetic acid (EDTA)	Sigma-Aldrich, Germany
FACS clean	BD Biosciences. Germany
FACS flow	BD Biosciences, Germany
FACS rinse	BD Biosciences, Germany
Fetal bovine serum (FBS)	Gibco, Germany
FM4-64	ThermoFisher Scientific, Germany
Formvar/Carbon-supported copper grids	Sigma-Aldrich, Germany
Glucose	Sigma-Aldrich, Germany
Glutaraldehyde	Santa Cruz Biotechnology, Germany
Glycerol	Carl Roth, Germany
Hank’s balanced salt solution (HBSS)	ThermoFisher Scientific, Germany
Hematoxylin solution	Carl Roth, Germany
HEPES 1M	ThermoFisher Scientific, Germany
Hydrochloric acid	J.T. Baker, Germany
Hydrogen peroxide	Carl Roth, Germany
IGEPAL CA-630	Sigma-Aldrich, Germany
Isoflurane	CP Pharma, Germany
Isopropanol	Carl Roth, Germany
Ketamine 10 %	Serumwerk Bernburg, Germany
Liquid barrier marker	Carl Roth, Germany
Liquid nitrogen	Air Liquide, Germany
Methanol	Sigma-Aldrich, Germany
Methyl butane	Carl Roth, Germany
Na-deoxycholate	Sigma-Aldrich, Germany
NaF	Sigma-Aldrich, Germany

Chemical	Company
Normal goat serum (NGS)	ThermoFisher Scientific, Germany
Osmium tetroxide	Sigma-Aldrich, Germany
PageRuler™ Plus Prestained Protein Ladder	ThermoFisher Scientific, Germany
Paraformaldehyde (PFA) solution 4 %	Santa Cruz Biotechnology, Germany
Percoll	GE Healthcare, Germany
Ponceau S	Sigma-Aldrich, Germany
ProLong™ Gold Antifade mountant with DAPI	CST, USA
Protein Assay Dye Reagent	Bio-Rad, Germany
Restore™ PLUS Western blot stripping buffer	ThermoFisher Scientific, Germany
RNAlater	ThermoFisher Scientific, Germany
Rompun (Xylazine) 2 %	Bayer, Germany
Roti Histol	Carl Roth, Germany
Roti-Block	Carl Roth, Germany
SDS-PAGE electrophoresis buffer 10x Tris/Glycine/SDS	Bio-Rad, Germany
SDS-PAGE transfer buffer 10x Tris/Glycine	Bio-Rad, Germany
Silica beads 300/1000 nm	Creative Diagnostics, USA
Sodium azide	Carl Roth, Germany
Sodium cacodylate trihydrate	Sigma-Aldrich, Germany
Sodium dodecyl sulfate (SDS)	Carl Roth, Germany
Sucrose	Sigma-Aldrich, Germany
TEMED	Sigma-Aldrich, Germany
Tissue-Tec® O.C.T.™ compound	Sakura Finetek, Germany
TRIS	Carl Roth, Germany
Triton X-100	Carl Roth, Germany
Trypan blue 0.5 % (w/v)	Biochrom, Germany
Tween 20	MP Biomedicals, Germany
UltraComp eBeads™ compensation beads	ThermoFisher Scientific, Germany
UltraPure™ DNase/RNase-free water	ThermoFisher Scientific, Germany
UltraPure™ SDS solution, 10 %	ThermoFisher Scientific, Germany
Vidisic EDO eye ointment with carbomer	Bausch&Lomb, USA
Zombie NIR™ fixable dye	BioLegend, USA
β-Mercaptoethanol	ThermoFisher Scientific, Germany

2.1.4. KITS

Table 4: List of used kits

Kit	Company
All-Prep DNA/RNA Mini Kit	Qiagen, Germany
FoxP3/Transcription Factor Staining Kit	ThermoFisher Scientific, Germany
LEGENDplex™ mouse inflammation panel	BioLegend, USA
Power SYBR® Green RNA-to-CT™ 1-Step Kit	ThermoFisher Scientific, Germany
SuperSignal™ West Femto chemiluminescent substrate	ThermoFisher Scientific, Germany
SuperSignal™ West Pico PLUS chemiluminescent substrate	ThermoFisher Scientific, Germany
TaqMan® RNA-to-CT™ 1-Step Kit	ThermoFisher Scientific, Germany
VECTASTAIN® ABC-HRP Kit	Vector Laboratories, USA

2.1.5. BUFFERS

Table 5: List of buffer solutions

Buffer name	Ingredients
30 % Sucrose	PBS 30 % (w/v) Sucrose
Anesthesia cocktail (Ketamine/Xylazine)	10 % (v/v) Xylazine (with Rompun 2 %, 10 mg/kg bodyweight) 20 % (v/v) Ketamine (with Ketamine 10 %, 100 mg/kg bodyweight)
Antigen retrieval buffer	10 mM Citric acid 0.1 % (v/v) Tween 20 pH 6.0
Blocking and permeabilization buffer	PBS 0.2 % (v/v) Triton X-100 5 % NGS
Buffer A	10 mM HEPES 320 mM Sucrose Protease inhibitors pH 7.4
Cryo buffer	SET buffer 5 % (v/v) DMSO
Dissection buffer	HBSS 13 mM HEPES 0.68 % (w/v) Glucose

Buffer name	Ingredients
EM fixation buffer I	100 mM Cacodylate buffer 2.5 % (w/v) PFA 2.5 % (w/v) Glutaraldehyde pH 7.4
EM fixation buffer II	100 mM Cacodylate buffer 1 % (w/v) Osmium tetroxide pH 7.4
FACS buffer	PBS 2 % (v/v) FBS 0.1 % (w/v) NaN3
Isotonic Percoll 100%	90 % (v/v) Percoll stock 10 % (v/v) 10X PBS
Isotonic Percoll 70%	70 % (v/v) Isotonic Percoll 30 % (v/v) DPBS without Ca^{2+}/Mg^{2+}
Isotonic Percoll 30%	30 % (v/v) Isotonic Percoll 70 % (v/v) DPBS without Ca^{2+}/Mg^{2+}
PER solution	10 % (w/v) ammoniumperoxodisulfate
Ponceau S staining solution	0.2 % (v/v) Ponceau S 3 % (v/v) Acetic acid
Primary antibody staining buffer	PBS 0.1 % (v/v) Triton X-100
RIPA lysis buffer	Protease inhibitors 50 mM TRIS/HCl 150 mM NaCl 1 % (v/v) IGEPAL CA-630 0.25 % (w/v) Na-deoxycholate 1 mM NaF pH 7.4
SDS-PAGE loading buffer	125 mM TRIS/HCl 2 % (v/v) SDS 10 % (v/v) Glycerol 2.5 % (v/v) β-Mercaptoethanol 1.5 mM Bromophenol blue pH 6.8
Secondary antibody staining buffer	PBS 0.1 % (v/v) Triton X-100 1 % NGS
Separating gel buffer	375 mM TRIS/HCl pH 8.8
SET buffer	320 mM Sucrose 1 mM EDTA 5 mM TRIS/HCl pH 7.4
Stacking gel buffer	250 mM TRIS/HCl pH 6.8
TBST buffer	99.0 % (v/v) TBS 0.1 % (v/v) Tween 20

Buffer name	Ingredients
Tris-buffered saline (TBS)	1.37 M NaCl 200 mM TRIS/HCl pH 7.6
Washing solution	PBS 0.1 % Tween 20

2.1.6. PRIMERS

2.1.6.1. TAQMAN® GENE EXPRESSION ASSAYS

Table 6: List of TaqMan® gene expression assays used for RT-qPCR

Protein	Gene	Assay ID
BDNF	*Bdnf*	Mm04230607_s1
C1qa	*C1qa*	Mm00432142_m1
C3	*C3*	Mm01232779_m1
CCL2	*Ccl2*	Mm00441242_m1
CD36	*Cd36*	Mm00432403_m1
CD68	*Cd68*	Mm03047343_m1
Claudin-5	*Cldn5*	Mm00727012_s1
HPRT	*Hprt*	Mm01545399_m1
IDO	*Ido1*	Mm00492586_s1
IFN-β	*Ifnb1*	Mm00439552_s1
IFN-γ	*Ifng*	Mm00801778_m1
IGTP	*Igtp*	Mm00497611_m1
IL-1β	*Il1b*	Mm00434228_m1
IL-6	*Il6*	Mm00446190_m1
iNOS	*Nos2*	Mm00440485_m1
IRGM1	*Irgm1*	Mm00492596_m1
NGF	*Ngf*	Mm00443039_m1
$p75^{NTR}$	*Ngfr*	Mm01309638_m1
TNF	*Tnf*	Mm00443258_m1
TREM-2	*Trem2*	Mm04209422_m1
TrkB	*Ntrk2*	Mm00435422_m1
VGLUT1	*Slc17a7*	Mm00812886_m1
ZO-1	*Tjp1*	Mm00493699_m1

2.1.6.2. SELF-DESIGNED PRIMERS

Table 7: List of self-designed primers used for RT-qPCR

Protein	Gene	*Species*	Primer	Sequence (5' to 3')
Claudin-1	*Cldn1*	*Mus musculus*	Fw	ACTCCTTGCTGAATCTGAACAGT
			Rv	GGACACAAAGATTGCGATCAG
CXCL9	*Cxcl9*	*Mus*	Fw	GAGTTCGAGGAACCCTAGTG

Protein	Gene	*Species*	Primer	Sequence (5' to 3')
		musculus	Rv	AACTGTTTGAGGTCTTTGAGG
CXCL10	*Cxcl10*	*Mus musculus*	Fw	AACTGCATCCATATCGATGAC
			Rv	GTGGCAATGATCTCAACAC
HPRT	*Hprt*	*Mus musculus*	Fw	GCTATAAATTCTTTGCTGACCTGCTG
			Rv	AATTACTTTTATGTCCCCTGTTGACTGG
MX2	*Mx2*	*Mus musculus*	Fw	TCACCAGAGTGCAAGTGAGG
			Rv	CATTCTCCCTCTGCCACATT
RSAD2	*Rsad2*	*Mus musculus*	Fw	GTCCTGTTTGGTGCCTGAAT
			Rv	GCCACGCTTCAGAAACATCT
Nucleo-protein	NP	Influenza A virus	Fw	GAGGGGTGAGAATGGACGAAAAAC
			Rv	CAGGCAGGCAGGCAGGACTT

2.1.7. ANTIBODIES

2.1.7.1. ANTIBODIES FOR HISTOPATHOLOGY

Table 8: List of primary antibodies used for histopathology

Primary Antibody (Clone)	Dilution	Reference	Company
Anti-mouse CD11b (298G2H5)	1:100	HS-384 117	Synaptic Systems, Germany
Anti-mouse IBA1 (134G9)	1:500	HS-234 017	Synaptic Systems, Germany
Anti-mouse MAP2 (198A5)	1:500	188 011	Synaptic Systems, Germany
Anti-mouse NeuN (Rb350D3)	1:2000	266 008	Synaptic Systems, Germany

Table 9: List of secondary antibodies used for histopathology

Secondary Antibody	Dilution	Reference	Company
Biotinylated anti-guinea pig	1:150	106-065-003	Jackson ImmunoResearch, UK
Biotinylated anti-mouse	1:120	115-065-146	Jackson ImmunoResearch, UK
Biotinylated anti-rabbit	1:120	712-065-153	Jackson ImmunoResearch, UK
Biotinylated anti-rat	1:150	712-065-153	Jackson ImmunoResearch, UK

2.1.7.2. ANTIBODIES FOR IMMUNOFLUORESCENCE CONFOCAL MICROSCOPY

Table 10: List of primary antibodies used for confocal microscopy

Primary Antibody (Clone)	Dilution	Reference	Company
Anti-mouse IBA1 (polyclonal)	1:200	HS-234 004	Synaptic Systems, Germany
Anti-mouse TMEM119 (28-3)	1:200	ab209064	Abcam, UK

Table 11: List of secondary antibodies used for confocal microscopy

Secondary Antibody	Fluorochrome	Dilution	Reference	Company
F(ab´)2 goat anti-mouse IgG (H+L)	-	1:500	A24514	ThermoFisher Scientific, Germany
Goat anti-guinea pig	AlexaFluor® 647	1:1000	A21450	ThermoFisher Scientific, Germany
Goat anti-rabbit	AlexaFluor® 555	1:1000	A32732	ThermoFisher Scientific, Germany

2.1.7.3. ANTIBODIES FOR FLOW CYTOMETRY

Table 12: List of fluorochrome-conjugated antibodies used for flow cytometry

Antibody (Clone)	Fluorochrome	Dilution	Company
Anti-mouse CD11b (M1/70)	APC	1:200	eBioscience™, USA
Anti-mouse CD11b (M1/70)	Brilliant Violet™ 605	1:80	BioLegend, USA
Anti-mouse CD45 (30-F11)	eFluor™ 450	1:200	BioLegend, USA
Anti-mouse CD80 (16-10A1)	PerCP/Cy5.5	1:66	BioLegend, USA
Anti-mouse CD86 (GL-1)	Brilliant Violet™ 421	1:50	BioLegend, USA
Anti-mouse CX3CR1 (SA011F11)	PE/Cy7	1:1333	BioLegend, USA
Anti-mouse F4/80 (BM8)	Brilliant Violet™ 510	1:50	BioLegend, USA
Anti-mouse F4/80 (BM8)	Brilliant Violet™ 605	1:66	BioLegend, USA
Anti-mouse FcγIII/II receptor (93)	-	1:50	BioLegend, USA
Anti-mouse MHC I (28-14-8)	FITC	1:200	eBioscience™, USA
Anti-mouse MHC II (I-A/I-E) (M5/114.15.2)	PE/Dazzle594™	1:500	BioLegend, USA

2.1.7.4. ANTIBODIES FOR FLOW SYNAPTOMETRY

Table 13: List of primary antibodies used for flow synaptometry

Primary Antibody	Dilution	Reference	Company
Anti-mouse Gephyrin	1:50	ab136343	Abcam, UK
Anti-mouse GluR1	1:500	ABN241	Sigma-Aldrich, Germany
Anti-mouse Homer1	1:200	MAB6889	R&D Systems, USA
Anti-mouse Synaptophysin	1:2000	101 004	Synaptic Systems, Germany
Anti-mouse VGLUT1	1:1000	135 303	Synaptic Systems

Table 14: List of secondary antibodies used for flow synaptometry

Secondary Antibody	Fluorochrome	Dilution	Reference	Company
Goat anti-chicken	AlexaFluor® 546	1:1000	A11040	ThermoFisher Scientific, Germany
Goat anti-guinea pig	AlexaFluor® 647	1:200	A21450	ThermoFisher Scientific, Germany
Goat anti-mouse	AlexaFluor® 405	1:200	A31553	ThermoFisher Scientific, Germany
Goat anti-rabbit	AlexaFluor® 488	1:4000	ab150081	Abcam, UK

2.1.8. SOFTWARE

Table 15: List of software used for data processing, graphical illustration and statistical analysis

Software	Version	Company
Adobe Illustrator	25.4.1	Adobe Inc., USA
Adobe InDesign	16.4	Adobe Inc., USA
Adobe Photoshop	22.5.1	Adobe Inc., USA
Attune NxT Software	3.1.2	ThermoFisher Scientific, Germany
DigitalMicrograph®	2.5	Gatan Inc., USA
FlowJo	10.5.3	FlowJo LLC., USA
GraphPad Prism	7.04	GraphPad Software, USA
ImageJ with FIJI distribution	1.53c	NIH, USA
LAS X Life Science	3.4.2.18368	Leica Microsystems, Germany
LEGENDplex™ Data Analysis Software	8.0	BioLegend, USA
Lightcycler 96 Software	1.1.0.1320	Roche Diagnostics International Ltd., Switzerland
Olympus VS-ASW	2.9.2 Build 17565	Olympus Life Science, USA
Quantity One	4.2	Bio-Rad, Germany
R	4.0.3	The R Foundation for Statistical Computing, Austria
R Studio	1.2.5042	RStudio Inc., USA
Softmax Pro	4.0	Molecular Devices LLC., USA
Sony Spectra Analyzer Software	2.0.2.14140	Sony Biotechnology, USA

2.2. METHODS

2.2.1. ANIMAL HUSBANDRY

All experiments were conducted with female 8 weeks-old, specific-pathogen-free C57BL/6JRj mice purchased from Janvier Labs (France). Groups of 4 to 5 animals were housed in individually ventilated cages with a 12-hour day/night cycle and access to food and water ad libitum. All animal care was in accordance with institutional guidelines and experimental protocols were approved by the Landesverwaltungsamt of Saxony-Anhalt, Germany.

2.2.2. ANIMAL MODEL OF INFLUENZA VIRUS INFECTION

The murine model of Influenza A virus infection was established by infection of mice with the mouse-adapted, laboratory IAV strain PR8/A/34(H1N1) kindly provided for this study by Prof. Dr. Dunja Bruder. In brief, Madin-Darby canine kidney cells were inoculated with the virus and incubated at 35 °C and 5 % CO_2 for 24 hours. Then, the cell culture supernatant was collected, centrifuged at 14,000 x *g* for 10 min to remove cell fragments and debris, aliquoted and stored in -80 °C until use [132].

C57BL/6JRj mice were deeply anesthetized by intraperitoneal injection of ketamine (1 %)-xylazine (10 mg/ml) and ointment was applied to keep eyes hydrated. Next, each mouse was held with the ventral side up, the head tilted back slightly, and intranasally infected dropwise into each nostril. The experimental group received a 0.32-fold of the median tissue culture infection dose $(TCID)_{50}$ of IAV that was determined elsewhere [133], diluted in 25 µl of phosphate-buffered saline (PBS) using a microliter pipette. Animals of the control group received 25 µl of PBS only.

2.2.3. COLLECTION OF BLOOD SERUM

To collect blood serum, mice were first deeply anesthetized with isoflurane and fixed to a dissection board with the ventral side up. Next, the peritoneal cavity was opened by an incision that was further extended anteriorly to the sternum and transversally to the lateral costal arch. Then, blood was taken from the inferior vena cava using a 1 ml syringe with 26G cannula and

incubated at 37 °C for 10 minutes (min). Subsequently, samples were centrifuged at 1,500 x *g* for 10 min, the serum supernatant was collected and stored at -80 °C.

2.2.4. COLLECTION OF BRONCHOALVEOLAR LAVAGE FLUID

Following the collection of blood serum, bronchoalveolar lavage (BAL) fluid was isolated by puncturing the trachea and careful insertion of a vein catheter. BAL was performed by injection of 1 ml ice-cold PBS through the catheter with a 1 ml syringe and subsequent collection of the lavage fluid. The BAL fluid was spun down at 420 x *g* for 10 min and stored at -80 °C until further use.

2.2.5. BRAIN COLLECTION

For brain extraction, the diaphragm was carefully punctured and removed to expose the thoracic cavity. The right atrium was cut open and the mice were perfused intracardially through the left ventricle with 60 ml of ice-cold Dulbecco's phosphate-buffered saline (DPBS) with Ca^{2+}/Mg^{2+}. Then, animals were decapitated, the skull exposed carefully, and opened using chirurgical scissors. The brain was extracted and placed on petri dishes before dissection into olfactory bulb, cortex (CTX), and hippocampal formation (HPF) according the Allen Mouse Brain Atlas [134]. Samples were stored either in PBS-filled reaction tubes and placed on ice for subsequent cell isolation, or reaction tubes filled with 1 ml RNAlater solution for isolation of ribonucleic acid (RNA). Samples designated for Western blot analysis or isolation of synaptosomes were snap frozen in liquid nitrogen. Brain tissue stored in RNAlater solution or snap frozen samples were kept at -80 °C until further use.

To collect brains designated for histopathological or immunofluorescence (IF) microscopical examination, mice were anesthetized and processed as described above. Perfusion was performed through the left ventricle of the heart with 40 ml sterile PBS followed by 20 ml of 4 % paraformaldehyde (PFA) solution. After decapitation, brains were extracted carefully and post-fixed in 4 % PFA (see 2.1.3) for 4 h (IF) or 24 h (histopathology) before being transferred to 30 % sucrose solution (see 2.1.5). After 48 h, brain samples for histopathology were moved to PBS + 0.1 % NaN_3, whereas samples for IF were placed in embedding molds and covered with Tissue-Tek® O.C.T.™ compound. Finally, brains within embedding molds were slowly frozen

in 2-methylbutane previously pre-cooled in liquid nitrogen and frozen samples were kept in -80 °C until processing.

2.2.6. IMMUNE CELL ISOLATION FROM BRAIN TISSUE

Freshly isolated brain samples were minced with a scalpel and mechanically homogenized in a 2 ml dounce homogenizer with 2 ml of dissection buffer (see 2.1.5). The cell suspension was then sieved through a 70-µm cell strainer placed on a 50 ml centrifugation tube. Subsequently, the dounce homogenizer was rinsed twice with 1 ml dissection buffer, the rinse fluid collected and added to the sample homogenate before centrifugation with 400 x *g* at 4 °C for 20 min. Next, the supernatant was discarded and the cell pellet resuspended in 10 ml of 70 % isotonic Percoll (see 2.1.5). Carefully, 10 ml of 30 % isotonic Percoll (see 2.1.5) were layered on top of the cell suspension followed by 5 ml of DPBS without Ca^{2+}/Mg^{2+}. The samples were then centrifuged in swing-out buckets with 800 x *g* at 4 °C for 35 min using the lowest acceleration and no brake, thus allowing the separation of cellular debris and cells along the discontinuous Percoll gradient. After centrifugation, remaining erythrocytes will be on the bottom of the centrifugation tube, whereas leukocytes and brain resident immune cells can be found in the 30 %/70 % isotonic Percoll interphase. Myelin, which resides at the DPBS/30 % isotonic Percoll interphase was then first removed with a pipette to facilitate the subsequent collection of cells from the 30 %/70 % Percoll interphase. Harvested cells were transferred to 50 ml centrifugation tubes and washed once with 30 ml of DPBS, followed by an additional washing step with 5 ml fluorescence-activated cell sorting (FACS) buffer (see Table 5 in 2.1.5) at 400 x *g*, 4 °C for 10 min. Finally, the cell count was determined using a Neubauer counting chamber and immune cells were immediately processed further for flow cytometric analysis.

2.2.7. CYTOKINE IMMUNOASSAY

Cytokine levels in blood serum and BAL fluid samples were analyzed in collaboration with the research group of Prof. Dr. Dunja Bruder at the HZI Braunschweig (Germany) using the LEGENDplex™ Mouse Inflammation Panel (see 0) according to the manufacturer's instructions. Samples were acquired with a LSR Fortessa flow cytometer and resulting data were further analyzed with the LEGENDplex™ Data Analysis Software 8.0 (see 2.1.8).

2.2.8. ISOLATION OF RIBONUCLEIC ACID

Tissue samples in RNAlater solution were transferred to BashingBeads lysis tubes filled with lysis buffer of the AllPrep DNA/RNA Mini Kit (see 0) and subsequently homogenized in the BeadBug benchtop homogenizer (three sets of 30 s shaking with 4350 bpm followed by 30 s pause). Tissue homogenate was then further processed according to the manufacturer's instructions and concentration of isolated RNA was determined using a NanoDrop 2000 spectrophotometer. Sample aliquots were diluted to a concentration of 30 ng/ml in RNase-free water and stored at -80 °C until further use.

2.2.9. QUANTITATIVE REVERSE TRANSCRIPTION PCR

Semi-quantitative reverse transcription polymerase chain reaction (RT-qPCR) was used to determine the gene expression levels of cytokines, inflammatory mediators, tight junction proteins, neurotrophins as well as neurotrophin receptors, synapse-associated proteins, and complement system proteins. Samples were analyzed in duplicates using 30 ng of isolated RNA with either TaqMan® gene expression assays (see Table 6 in 2.1.6.1) or Power SYBR® Green and self-designed primer pairs (see Table 7 in 2.1.6.2). Primer pairs were initially designed using the open Primer-BLAST tool [135] provided by the National Center for Biotechnology Information (Bethesda, MD, USA). Search for Optimal primers was carried out based on final PCR product size, spanning of an exon-exon junction, and minimal unintended mismatches. Selected primers were synthesized by TIB MOLBIOL (Berlin, Germany) and initially tested for successful amplification. Finally, primers were used in a final concentration of 100 nM. PCR was carried out using a LightCycler® 96 set to the following configuration of thermal-cycling parameters shown in Table 16 below:

Table 16: Thermal-cycling parameters for RT-qPCR

	Temperature	**Duration**	
Reverse transcription	48 °C	30 min	
Polymerase activation	95 °C	10 min	
Denaturation	95 °C	15 s	55 cycles
Annealing / Extension	60 °C	60 s	

In case of the SYBR® green RT-qPCR, amplification was followed by a melting curve analysis. Gene expression of hypoxanthine phosphoribosyltransferase 1 (*Hprt*) was used as reference and

relative target gene mRNA levels were calculated by the ratio target gene / reference gene and subsequently normalized to mean values of the control group.

2.2.10. QUANTIFICATION OF VIRAL NUCLEOPROTEIN

The amount of viral mRNA copies of IAV nucleoprotein in brain samples was determined by RT-qPCR using 600 ng of isolated RNA and Power SYBR® Green with self-designed primers (see Table 7 in 2.1.6.2). To allow the absolute quantification of viral load, a standard curve was first generated using a reference plasmid standard with known numbers of IAV NP copies per microliter (1.5×10^1 to 1.5×10^9) [133]. PCR was carried out using a LightCycler® 96 set to the configuration of thermal-cycling parameters shown in Table 17 below and the reaction was followed by a melting curve analysis.

Table 17: Thermal-cycling parameters for quantification of IAV nucleoprotein

	Temperature	**Duration**	
Reverse transcription	48 °C	30 min	
Polymerase activation	95 °C	10 min	
Denaturation	95 °C	5 s	55 cycles
Annealing	60 °C	10 s	
Extension	72 °C	5 s	

2.2.11. HISTOPATHOLOGY AND IMMUNOFLUORESCENCE MICROSCOPY

2.2.11.1. HISTOPATHOLOGY

Histopathology of mouse brains was carried in collaboration with Synaptic Systems (Göttingen, Germany) and samples were isolated and prepared as stated in section 2.2.5. Using an automatic tissue processor, brains were first dehydrated in 1X Zinc fixative for 4 h followed by incubation in ethanol at concentrations increasing from 70 % to 100 % and Roti Histol for 2 h, respectively. Subsequently, brains were embedded in paraffin and sagittal sections were cut at 3-µm thickness. Next, brain slides were mounted on microscopic slides and de-paraffinized using Roti Histol and alcohol at concentrations decreasing from 100 % to 70 % for 2 h respectively, followed by washing steps in distilled water and PBS. After antigen retrieval at 97 °C for 30 min and blocking of unspecific binding and endogenous peroxidase activity with blocking and permeabilization buffer (see Table 5 in section 2.1.5) supplemented with 3 % hydrogen peroxide,

slides were washed three times with washing solution and stained with primary antibodies against CD11b, IBA1, MAP2, and NeuN (see Table 8 in section 2.1.7.1) in primary antibody staining buffer (see Table 5 in section 2.1.5) at room temperature for 1 h. Subsequently, slides were washed three times and incubated with matching, biotinylated secondary antibodies at room temperature for 30 min (see Table 9 in 2.1.7.1). After a final washing step, slides were developed using VECTASTAIN® ABC-HRP Kit (see Table 4 in 0). The reaction was stopped by three washing steps in distilled water and samples were counterstained with hematoxylin before another washing step with tap water and distilled water. Finally, samples were dehydrated in alcohol at increasing concentrations, propanol, and Roti Histol for 2 h, respectively, before mounting of the cover slip. For histological examination, sections were imaged and analyzed using an Olympus VS120 virtual-slide-microscope equipped with an Olympus VC50 camera and a 40X objective, and Olympus VS-ASW imaging software (see Table 15 in 2.1.8).

2.2.11.2. IMMUNOFLUORESCENCE

For the preparation of cryosections from frozen brain samples embedded in Tissue-Tec® O.C.T.™ compound, samples were first placed in a cryostat set to a working temperature of -12 °C at least 24 h prior to sectioning. Then, sagittal sections of 20-µm thickness were transferred to SuperFrost Plus™ microscopy slides, air-dried for 1 h and fixed in acetone at -20 °C for 8 min. Subsequent antigen retrieval was performed as described above (see 2.2.11.1) and slides were then incubated with blocking and permeabilization buffer (see Table 5 in section 2.1.5) supplemented with unconjugated F(ab´)2 goat anti-mouse IgG (H+L) antibody (see Table 11 in section 2.1.7.2) at 4 °C for 2 h. Slides were rinsed three times with washing solution for 10 min and incubated with primary antibodies against IBA1 and TMEM119 (see Table 10 in section 2.1.7.2) in primary antibody staining buffer at 4 °C overnight. On the next day, slides were rinsed again three times with washing solution and incubated with matching secondary antibodies (see Table 11 in section 2.1.7.2) in secondary antibody staining buffer (see Table 5 in section 2.1.5) protected from light at room temperature for 1 h. After final a washing step, coverslips were mounted using ProLong™ Gold antifade mountant with 4′,6-diamidino-2-phenylindole (DAPI), dried in the dark for 24 h and the borders sealed with nail polish. To image immune cells in the brain tissue, z-stacks of 1-µm step length were generated with a Leica TSC SP8 confocal laser scanning microscope equipped with a 20X objective. Composite images were generated using ImageJ with Fiji distribution [136] (see Table 15 in section 2.1.8).

2.2.12. FLOW CYTOMETRY

Immune cells were isolated from cortex and hippocampal formation as described in the text (see 2.2.6) and immediately processed further for flow cytometric analysis. First, cells of each sample were plated in a 96-well plate with FACS buffer and incubated with anti-FcγIII/II receptor antibody to block unspecific antibody binding, combined with Zombie NIR™ fixable dye (see Table 12 in section 2.1.7.3) for discrimination of dead cells at 4 °C for 20 min. Without washing, cells were stained in the dark with fluorochrome-conjugated antibodies (see Table 12) at 4 °C for 30 min. Accordingly, Fluorescence-Minus-One (FMO) controls were implemented to determine the level of autofluorescence for each fluorochrome-conjugated antibody. Following the incubation, the wells were filled up with 150 µl FACS buffer and the plate was centrifuged at 400 x *g*, 4 °C for 10 min. The supernatant was discarded and cells were fixed in the dark using 4 % PFA at 4 °C for 20 minutes. Next, cells were washed again with 200 µl FACS buffer and centrifuged at 400 x *g*, 4 °C for 10 min. Finally, cells were resuspended in 110 µl FACS buffer and stored at 4 °C until flow cytometric analysis. Samples were acquired using a Sony SP6800 spectral flow cytometer.

2.2.13. SYNAPTOSOME PREPARATION

2.2.13.1. ISOLATION AND STORAGE

Synaptosomes were isolated from cortex and hippocampal formation according to previous protocols but with minor modifications [137]. First, snap frozen tissue samples were thawed on ice in 1 ml of buffer A solution (see Table 5 in section 2.1.5) with protease inhibitors. Thereafter, samples in buffer A solution were transferred to a 17 ml dounce homogenizer and filled up a total of 5 ml buffer A solution. Then, samples were homogenized with 5 to 7 strokes using a matching pestle attached to a drilling machine set to 500 to 700 rpm. The homogenate was then placed in a 12 ml centrifugation tube (*tube A*) and centrifuged at 1,000 x *g*, 4 °C for 10 min. After collecting the supernatant from *tube A* in a new 12 ml centrifugation tube (*tube B*), the remaining pellet in *tube A* was resuspended in 5 ml buffer A, homogenized again in a 17 ml dounce homogenizer and transferred back to *tube A*. Following another centrifugation at 1,000 x *g*, 4 °C for 10 min, the supernatant in *tube A* was combined with the supernatant in *tube B*, whereas the pellet was discarded. *Tube B* was then centrifuged at 12,000 x *g*, 4 °C for 15 min, the supernatant discarded and the pellet consisting of the crude membrane fraction was washed

in 5 ml of buffer A solution. The tube was centrifuged again at 12,000 x *g*, 4 °C for 15 min and the pellet resuspended in 700 µl of buffer A. A discontinuous sucrose gradient consisting of layers with 1 ml of 1.2 M, 1.0 M, and 0.85 M sucrose, respectively, was carefully set up in a fresh ultracentrifugation tube and the crude membrane pellet resuspended in buffer A solution was placed on top. Next, the ultracentrifugation tubes were sealed, inserted into a swing-out rotor and centrifuged without brake at 80,000 x *g*, 4 °C for 2 h. Thereafter, debris was first removed from the 0.85 M/1.0 M sucrose interphase. This step was followed by the collection of synaptic material from the 1.0 M/1.2 M sucrose interphase, which was placed into a new ultracentrifugation tube and filled up with 3 ml Sucrose-EDTA-Tris (SET) buffer [138] (see Table 5 in section 2.1.5). The tube was centrifuged at 100,000 x *g*, 4 °C for 1 h and the supernatant discarded. The remaining pellet was washed again in 3 ml of SET buffer and centrifuged at 100,000 x *g*, 4 °C for 30 min. Finally, the supernatant was discarded, the pellet resuspended in 1000 ml Cryo buffer (see Table 5) and transferred to 1.5 ml safe-lock tubes. Synaptosome samples were placed into a Mr. Frosty™ isopropanol freezing container and slowly cooled to and stored in -80 °C until further use [138].

2.2.13.2. ELECTRON MICROSCOPY

In order to visualize isolated synaptosomes via transmission electron microscopy (EM), frozen synaptosome samples were prepared according to published protocols [139] but with slight modifications: Samples were thawed in a water bath at 37 °C and centrifuged at 14,000 x *g* for 10 min to remove sucrose-containing buffer. The supernatant was gently removed using a microliter pipette and the pellet subsequently resuspended in EM fixation buffer I (see Table 5 in section 2.1.5) and stored in the refrigerator overnight. On the next day, synaptosomes were centrifuged at 14,000 x *g* for 10 min, the supernatant gently removed and the pellet resuspended in EM fixation buffer II (see Table 5) and incubated for 30 min. Then, the pellet was centrifuged again at 14,000 x *g* for 10 min and washed with distilled water before being dehydrated stepwise in a graded series of ethanol ranging from 50 % to 100 % for 5 min, respectively. Finally, the synaptosomes were centrifuged at 14,000 x *g* for 10 min, the supernatant discarded and the pellet within the safe-lock tube embedded in Durcupan ACM dripped carefully into the tubes. The sample was allowed to polymerize at 70 °C for 3 days before being sectioned in an ultramicrotome. Here, the tip of the tube containing the complete block of Durcupan was cut to generate ultrathin slides of 50 to 70 nm that were collected on Formvar-coated slot grids of copper. The slides were then examined at the Leibniz Institute for Neurobiology (Magdeburg,

Germany) with a LEO 912 transmission electron microscope and the synaptosomes imaged with a MegaScan™ 2K CCD camera using the DigitalMicrograph® software (see Table 15 in section 2.1.8).

2.2.13.3. SDS-PAGE AND WESTERN BLOTTING OF SYNAPTIC PROTEINS

To quantify the abundance of synaptic proteins, aliquots of frozen synaptosomes were prepared for sodium dodecyl sulphate–polyacrylamide gel electrophoresis (SDS-PAGE) and subsequent Western blot analysis. First, samples were thawed in a water bath at 37 °C and centrifuged for 10 min at 14,000 x *g* to facilitate the removal of sucrose-containing buffer. The resulting pellets were resuspended in radio-immunoprecipitation assay (RIPA) lysis buffer (see Table 5 in section 2.1.5) containing protease inhibitors and lysed for 30 min at 37 °C. The homogenates were then centrifuged at 100,000 x *g*, 4 °C for 30 min, the supernatants collected, and the pellets discarded. Protein concentrations were determined by Bradford assay using 10 µl of sample lysate, the Protein assay dye reagent, and the SpectraMax M5 microplate reader. Then, 50 µg of protein per sample were incubated in SDS-PAGE loading buffer at 96 °C for 5 min and loaded onto a polyacrylamide gel. The electrophoresis was carried out at room temperature with a constant voltage of 80 V for the stacking gel (4 % polyacrylamide) and 120 V in the separating gel (10 % polyacrylamide) using a semi-dry electrophoresis chamber.

Table 18: Polyacrylamide gel composition used in SDS-PAGE

	4 % Stacking gel	**10 % Separating gel**
30 % acrylamide / bisacrylamide	335 µl	2000 µl
Stacking gel buffer	1250 µl	-
Separating gel buffer	-	3000 µl
dH_2O	845 µl	900 µl
10 % SDS solution	25	60
PER solution	20	30
TEMED	5	12

After a total of 2 h run time, gels were placed into a transfer chamber and separated proteins were transferred to nitrocellulose membranes with a pore size of 0.45 µm using a constant voltage of 15 V for 60 min. Next, membranes were stained with Ponceau S staining solution (Table 3 in 2.1.3) to verify the proper transfer of proteins, washed with acetic acid and subsequently incubated with 5 % skimmed milk powder in Tris-buffered saline (TBS, see Table 5 in section 2.1.5) for 60 min to block unspecific binding. Then, membranes were rinsed with TBST buffer

(see Table 5) and incubated with the primary antibody rabbit anti-mouse VGLUT1 (dilution 1:2000, #135 303, Synaptic Systems, Germany) at 4 °C overnight. Following incubation, membranes were rinsed again with TBST buffer and incubated with a matching HRP-conjugated secondary antibody goat anti-rabbit (dilution 1:20000, #111-035-144, Jackson ImmunoResearch Europe Ltd.) at room temperature for 2 h. Membranes were washed thoroughly with TBST buffer to remove unbound secondary antibodies and finally, protein bands were revealed by chemiluminescence assay in a ChemiDoc XRS+ imaging system. Densitometric analysis of blotted protein bands was performed using ImageJ with Fiji distribution [136] (denoted in Table 15 in section 2.1.8).

2.2.14. FLOW SYNAPTOMETRY

2.2.14.1. SAMPLE PREPARATION

Aliquots of frozen synaptosomes were thawed in a water bath at 37 °C and centrifuged for 10 min at 14,000 x *g* to remove sucrose-containing buffer. The supernatant was removed carefully using a microliter pipette and pellets were resuspended in 100 µl 1X Fixation buffer of the FoxP3/Transcription Factor Staining Kit (see Table 4 in section 0). Upon incubation on ice for 45 min, samples were centrifuged again for 10 min at 14,000 x *g* and the supernatant removed. The pellets were resuspended in 200 µl SET buffer (see Table 5 in section 2.1.5) and aliquots of 5 µl per sample were added to 45 µl of 1X Permeabilization buffer (of the FoxP3/Transcription Factor Staining Kit) supplemented with 10 % normal goat serum (NGS) and incubated in the refrigerator overnight. On the next day, primary antibodies against Gephyrin, glutamate receptor 1 (GluR1), Homer1, Synaptophysin, and VGLUT1 (see Table 13 in section 2.1.7.4) were added to the synaptosomes and incubated on ice for 45 min. Thereafter, 200 µl of 1X Permeabilization buffer supplemented with 10 % NGS were added to the tubes which were then centrifuged at 14,000 x *g*, 4 °C for 10 min. The supernatants were carefully aspirated and the synaptosomes resuspended in 50 µl of 1X Permeabilization buffer supplemented with 10 % NGS. Matching secondary antibodies were added (see Table 14) and the tubes incubated on ice in the dark for 45 min. Accordingly, Fluorescence-Minus-One (FMO) and isotype controls were implemented to determine the level of autofluorescence for each fluorochrome-conjugated antibody. Secondary antibody staining was stopped by addition of 200 µl of 1X Permeabilization buffer supplemented with 10 % NGS and samples were centrifuged with 14,000 x *g* at 4 °C for

10 min. Supernatants were aspired and synaptosomes resuspended in 100 µl SET buffer. Finally, the styryl dye FM4-64 was added to a final concentration of 0.2 µg/ml [138] and the synaptosomes were stored on ice in the dark until measurement.

2.2.14.2. ADJUSTMENT OF FLOW CYTOMETER

Synaptosomes were acquired with the Attune NxT Flow Cytometer (ThermoFisher) equipped with 405 (violet), 488 (blue), 561 (yellow-green), and 633 nm (red) lasers. Voltages for forward-scatter light (FSC), side-scatter light (SSC) and fluorescence detection channels were set as follows: FSC 400 V, SSC 500 V, violet laser detection channel (VL)-1 400 V, blue laser detection channel (BL)-1 400 V, BL- 3 380 V, yellow-green laser detection channel (YL)-1 400 V, red laser detection channel (RL)-1 440 V, whereas not required detection channels remained de-activated. To allow the optimal acquisition of synaptosomes, less sensitive FSC-triggered detection of events was replaced by fluorescence-triggered detection of FM4-64 in BL3 with a threshold level set to 0.3 x 10^3 to neglect FM4-64-negative events [138]. To reduce coincident particle detection, the flow cytometer was operated at the lowest flow rate with 12.5 µl/min combined with adequate dilution of samples in SET buffer prior to the acquisition to establish an event rate below 300 events/s. Furthermore, red-fluorescent silica beads with a diameter of 300 nm and 1000 nm were measured to allow a size discrimination of FM4-64-positive events in the FSC channel during data analysis using FlowJo software (see Table 15 in section 2.1.8).

2.2.15. STATISTICAL ANALYSIS

Relative bodyweight between groups was compared by multiple *t*-test with Holm-Sidac *post-hoc* correction. Cytokine concentrations in BAL fluid and blood serum were compared by one-way ANOVA with Holm-Sidak *post-hoc* correction. Data from flow cytometry, flow synaptometry, and RT-qPCR were compared by Student's *t*-test with Welch's correction and multiple *t*-test with Holm-Sidac *post-hoc* correction. Statistical analysis of Western blot data was performed by one-way ANOVA with Holm-Sidak *post-hoc* correction. All tests were carried out in GraphPad Prism 7 (GraphPad Software, CA, USA) and R (version 4.0.3) [140] with "lattice" package [141] (see Table 15 in section 2.1.8). Data shown is representative of three independent experiments. In all cases, results are presented as arithmetic mean and were considered significant, with $p < 0.05$.

3. RESULTS

3.1. INFLUENZA A VIRUS INFECTION CAUSES A STRONG INFLAMMATION IN THE LUNGS

In order to characterize the effect of peripheral infection on the homeostasis of the CNS in detail, mice were infected with a sublethal dose of the non-neurotropic, mouse-adapted influenza A virus strain H1N1/PR8/34 as described elsewhere [133]. Over the course of infection, the relative bodyweight of animals was monitored. BAL fluid was taken for cytokine measurement 0, 1, 2, 3, 4, 5, 7, 9, and 11 days post-infection (dpi), whereas blood serum was collected 0, 2, 4, 6, 9, and 11 dpi (Figure 3). Brains of infected mice were isolated on 7, 10, 14, and 21 dpi and used for FACS, histopathological and IF microscopy, RNA isolation with subsequent PCR, and synaptosome isolation for Western blotting and flow synaptometry (FSM) (as described with more detail in chapter 2.2).

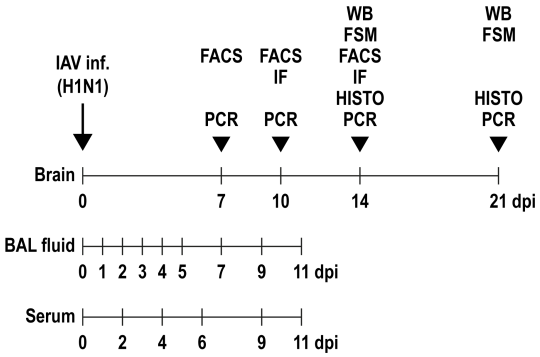

Figure 3: Experimental design of murine IAV infection model.
In this study, female 8 weeks-old C57BL/6JRj mice were infected intranasally with a sub-lethal dose of influenza A/PR8/A/34(H1N1) and sampled between 7, 10, 14, and 21 post-infection (dpi) for PCR, flow cytometry (FACS), histopathological (HISTO) and immunofluorescence (IF) microscopy, Western blot (WB) or flow synaptometry (FSM) analysis. Furthermore, cytokine concentrations in blood serum and BAL fluid were determined between 0 and 11 dpi. (adapted from [142])

When compared the relative bodyweight of non-infected controls, IAV-infected mice started to lose weight between 4 and 5 dpi (Figure 4). By day 7 (non-infected 100.8 ± 0.7 % vs. IAV-infected 89.8 ± 1.9 %, $p < 0.05$) and day 8 (non-infected 102.2 ± 0.6 % vs. IAV-infected 86.7 ± 2.5 %, $p < 0.001$) there was a significant decrease in bodyweight of H1N1-infected mice compared to the mock-infected control group. Starting 9 dpi, infected mice recovered, as indicated by increasing relative bodyweight that reached initial values by 14 dpi (non-infected 107.9 ± 0.7 % vs. IAV-infected 102.9 ± 1.9 %, $p < 0.81$).

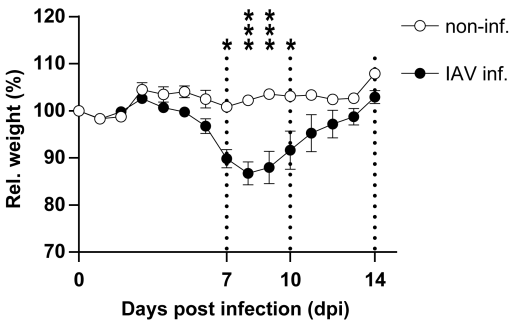

Figure 4: Course of relative bodyweight throughout IAV infection.
Relative bodyweight was determined for non-infected (white dots) and IAV-infected C57BL/6JRj mice (black dots) over the first 2 weeks of infection. Dashed vertical lines indicate the time points of experiments in line with the experimental model depicted in Figure 3. After 7 dpi, IAV-infected mice displayed a significantly reduced relative bodyweight compared to non-infected controls. 9 dpi, infected mice started to recover and reached initial values by 14 dpi. Data are shown as mean ± SEM and datapoints between groups were compared by multiple Student's *t*-tests with Holm-Sidak *post-hoc* correction. Significant differences are indicated by * ($p < 0.05$, *** $p < 0.001$). (adapted from [142])

Next to the course of bodyweight, the levels of cytokines and chemokines were monitored in the BAL fluid of non-infected and IAV-infected C57BL/6JRj mice (Figure 5a-h).

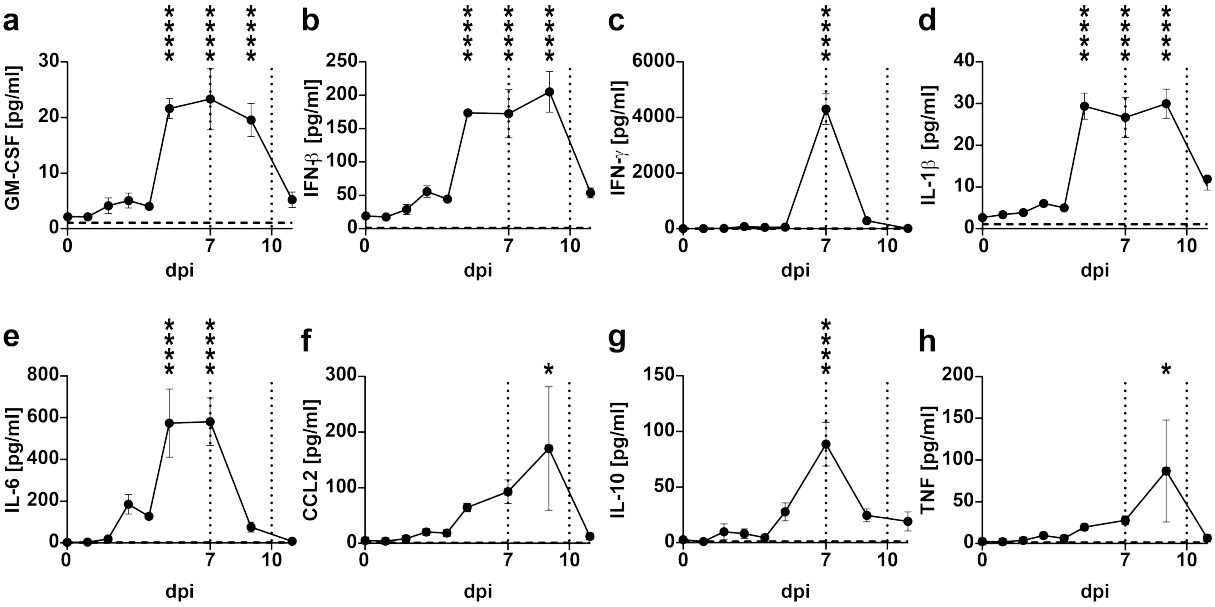

Figure 5: Cytokine levels in bronchoalveolar lavage fluid increase upon IAV infection in mice.
Cytokine levels in BAL fluid collected from lungs of IAV-infected C57BL/6JRj mice on 0, 1, 2, 3, 4, 5, 7, 9, and 11 dpi were determined by cytokine immunoassay. Upon 5 dpi, significantly increased concentrations of GM-CSF, IFN-β, IL-1β, and IL-6 were observed in the BAL fluid of IAV-infected mice. Upon 11 dpi, cytokines sharply declined. Graphs depict the cytokine concentration in pg/ml on each sampling day. Dashed vertical lines indicate the time points of flow cytometric analysis. Dashed horizontal lines indicate the detection limit of each cytokine in the cytokine immunoassay, respectively. Statistical analysis was performed using one-way ANOVA with Holm-Sidak *post-hoc* correction and data are shown as mean ± SEM. Significant differences are indicated by * ($p < 0.05$, **** $p < 0.0001$). (adapted from [142])

Here, IFN-β (Figure 5b, 55.7 ± 8.9 pg/ml, 3 dpi, $p < 0.50$) and IL-6 (Figure 5e, 185.1 ± 46.7 pg/ml, 3 dpi, $p < 0.35$) already showed an increase 3 dpi while a significant increase ($p < 0.0001$) was observed for GM-CSF, IFN-β, IL-1β, and IL-6 5 dpi, indicating the

onset of inflammation and adaptive immunity in the lungs. In this context, GM-CSF (Figure 5a, 23.3 ± 5.5 pg/ml, 7 dpi, $p < 0.0001$), IFN-γ (Figure 5c, 4297.4 ± 558.4 pg/ml, 7 dpi, $p < 0.0001$), IL-6 (Figure 5e, 580.6 ± 113.8 pg/ml, 7 dpi, $p < 0.0001$), and IL-10 (Figure 5g, 88.5 ± 19.7 pg/ml, 7 dpi, $p < 0.0001$) reached their maximum concentration 7 dpi, whereas IFN-β (Figure 5b, 204.9 ± 30.6 pg/ml, 9 dpi, $p < 0.0001$), IL-1β (Figure 5d, 30.0 ± 3.5 pg/ml, 9 dpi, $p < 0.0001$), CCL2 (Figure 5f, 170.6 ± 111.2 pg/ml, 9 dpi, $p < 0.05$), and TNF (Figure 5h, 86.8 ± 61.0 pg/ml, 9 dpi, $p < 0.05$) peaked on 9 dpi. Upon 11 dpi, the cytokine concentrations in the BAL fluid displayed a sharp decline to their initial values.

3.2. PERIPHERAL IAV INFECTION ALTERS HOMEOSTASIS OF BBB AND CNS

Next to the BAL fluid, cytokine levels were further determined in the blood serum during the course of IAV infection (Figure 6a-h). Here, concentrations of IFN-γ (Figure 6c, 156.0 ± 34.4 pg/ml, 6 dpi, $p < 0.0001$) and IL-6 (Figure 6e, 37.7 ± 11.5 pg/ml, 6 dpi, $p < 0.003$) were found significantly elevated 6 dpi. Similar to the observations made in the BAL fluid, levels of TNF (Figure 6h, 5.4 ± 1.1 pg/ml, 9 dpi, $p < 0.0582$) displayed an increase upon IAV infection that was close to significance 9 dpi. However, when compared to the magnitude of cytokine concentrations observed in the BAL fluid, overall levels of IFN-γ, IL-6, and TNF in the blood serum remained at much lower values. Although deviations from their baseline values were observed, serum concentrations of GM-CSF (Figure 6a), IFN-β (Figure 6b), IL-1β (Figure 6c), CCL2 (Figure 6f), and IL-10 (Figure 6g) did not correlate with their levels in the BAL fluid and remained without significant difference. Finally, all monitored concentrations returned to their steady state 11 dpi.

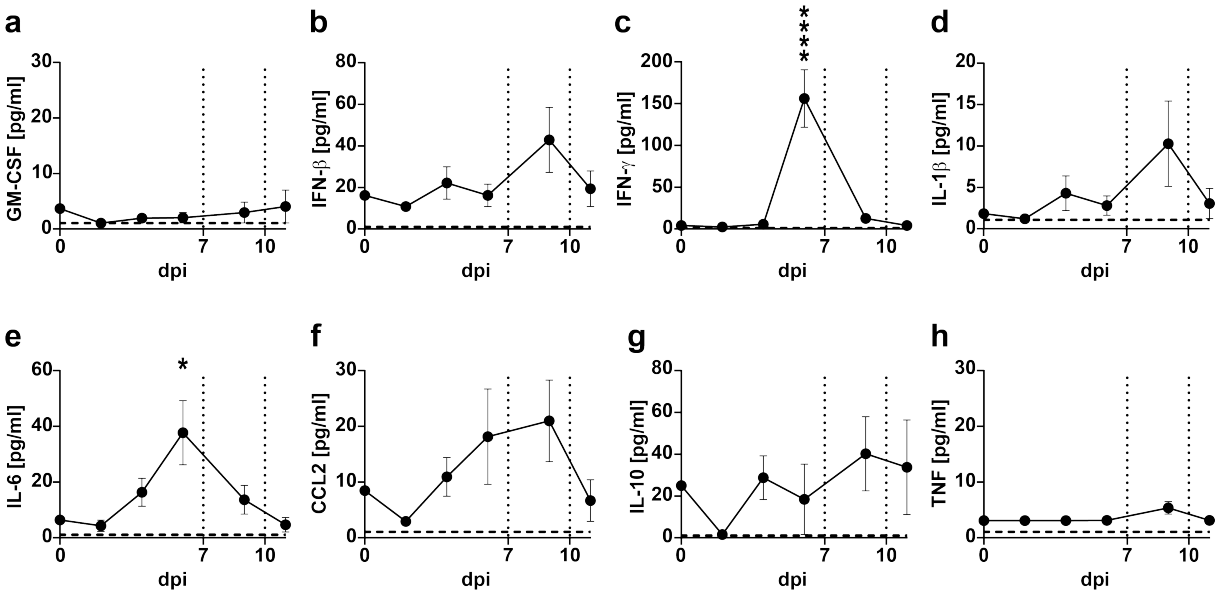

Figure 6: Cytokine levels in blood serum of IAV-infected mice.
Cytokine levels in blood serum of IAV-infected C57BL/6JRj mice were determined by cytokine immunoassay on 0, 2, 4, 6, 9, and 11 dpi. Upon 6 days post IAV infection, significantly increased cytokine concentration in the serum could be observed for IFN-γ and IL-6. Graphs depict the cytokine concentration in pg/ml on each sampling day. Dashed vertical lines indicate the time points of flow cytometric analysis. Dashed horizontal lines indicate the detection limit of each cytokine in the cytokine immunoassay, respectively. Statistical analysis was performed using one-way ANOVA with Holm-Sidak *post-hoc* correction and data are shown as mean ± SEM. Significant differences are indicated by * ($p < 0.05$, **** $p < 0.0001$). (adapted from [142])

Previously, numerous studies have highlighted the ability of systemic infections, or simply the administration of pathogen-mimicking endotoxin or polyinosinic:polycytidylic acid (poly[I:C]), to alter the homeostasis of the brain and induce sickness behavior [130, 143–145]. Due to the observed increase in cytokine levels in BAL fluid and blood serum, this study aimed to investigate related effects in the CNS. Thus, different time points were chosen based on initial results: 7 dpi (first day of significantly different relative bodyweight), 10 dpi (last day of significantly different relative bodyweight), 14 dpi (restoration of initial relative bodyweight), and 21 dpi (to evaluate potential long-term effects of IAV infection). First, gene expression of cytokines *Il1b* (IL-1β), *Il6* (IL-6), *Tnf* (TNF), and *Ccl2* (CCL2) in the cortex (CTX) and hippocampal formation (HPF) during the acute phase of IAV infection was measured by reverse transcription qPCR (RT-qPCR) analysis (Figure 7a-d). In comparison to non-infected controls, no significant differences were observed in either of the examined brain regions.

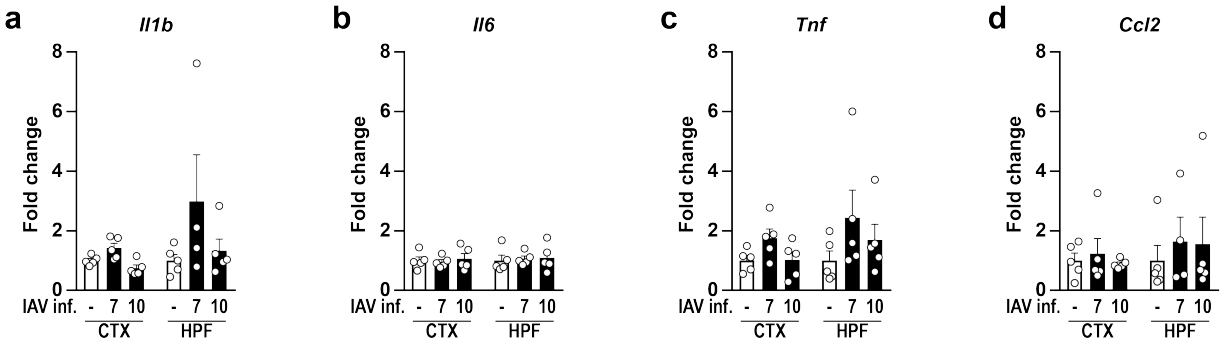

Figure 7: Cytokine and chemokine gene expression levels in cortex and hippocampus of IAV-infected mice. Brains were isolated from non-infected (white bars) and infected mice (black bars) as described above and dissected into cortex (CTX) and hippocampal formation (HPF) according to the Allen Mouse Brain Atlas [134]. RNA was isolated and used to analyze gene expression levels of IL-1β (*Il1b*), IL-6 (*Il6*), TNF (*Tnf*), and CCL2 (*Ccl2*) during the acute and late phase of IAV infection (7-10 dpi). No significant differences in the gene expression of the analyzed genes were observed during the course of infection. Relative gene expression was examined by RT-qPCR as described above and expression of target genes was normalized to the expression level of *Hprt*. Subsequently, normalization of the relative expression was performed to the means of non-infected animals and is indicated as fold change. Data are shown as mean ± SEM and groups were compared via Student's *t*-test with Welch's correction. (adapted from [142])

Next, the presence of viral nucleoprotein as an indicator for its replication was assessed in cortex, hippocampus, and olfactory bulb 7 and 10 dpi to exclude direct viral effects in the CNS of IAV-infected mice (Figure 8a). Noteworthy, viral nucleoprotein was not detectable in the examined brain regions, which is in line with previous reports that have shown IAV/PR8/34 to be non-neurotropic [130, 131]. In contrast, gene expression levels of *Ifnb1* (IFN-β) were elevated in the cortex 10 dpi ($p < 0.055$) and significantly increased by 14 dpi (Figure 8b). Similarly, mRNA levels of *Ifng* (IFN-γ) showed a trend towards an increase in the cortex of IAV-infected animals10 dpi, albeit without reaching significance (Figure 8c, $p < 0.18$). Typically, the induction of interferons often results in a plethora of immune responses ranging from the establishment of an anti-viral state in neighboring cells to modulation of the adaptive immunity. To test whether the observed alterations of IFN-β and IFN-γ gene expression accumulated in induction of ISGs, RT-qPCR was utilized to assess mRNA levels of the guanosine triphosphate (GTP) hydrolase enzymes (GTPases) *Irgm1* (IRGM1) and *Igtp* (IGTP) next to antiviral *Mx2* (MX2) or *Rsad2* (RSAD2) (Figure 8d-g). No differences were observed in *Mx2* and *Rsad2* gene expression in the cortex and hippocampus of IAV-infected mice. However, gene expression levels of *Irgm1* displayed a significant increase in the cortex 10 dpi, thus supporting previous findings of an *Ifng* induction upon IAV infection in this brain region.

a

IAV infection	Cortex	Hippo-campus	Olfactory bulb
-	not detected	not detected	not detected
7 dpi	not detected	not detected	not detected
10 dpi	not detected	not detected	not detected

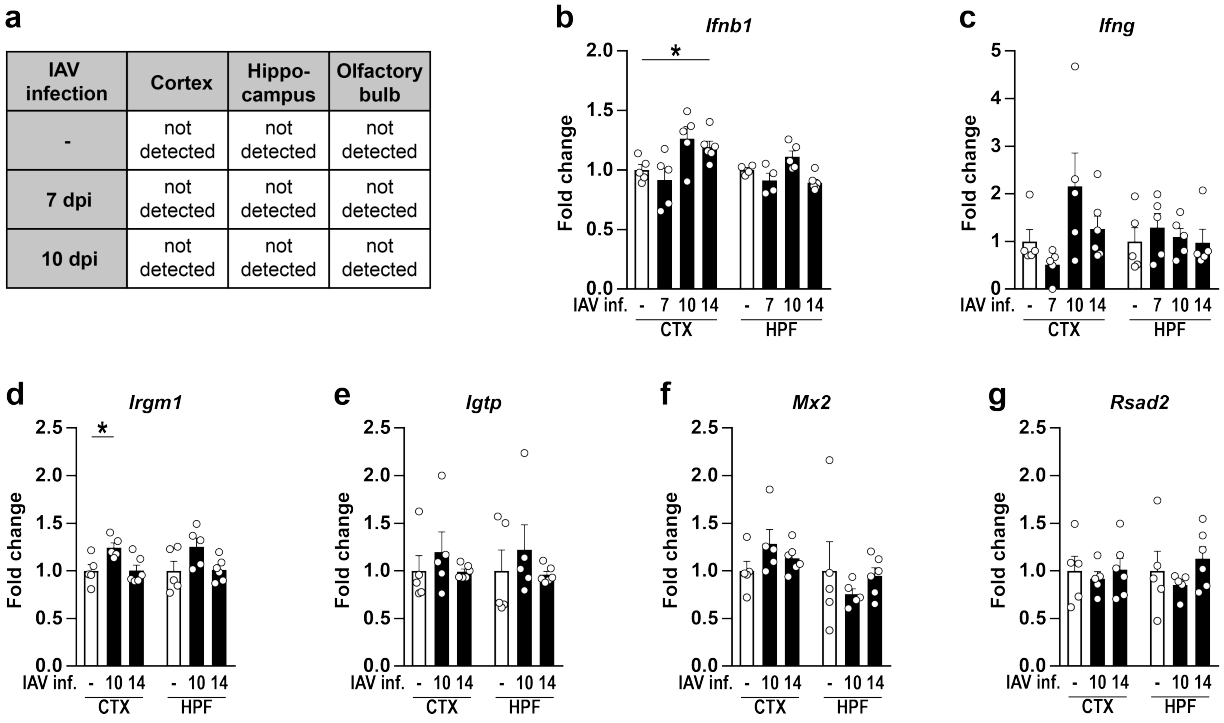

Figure 8: Gene expression levels of interferons and interferon-stimulated genes are altered in brains of IAV-infected mice.
Cortex (CTX), hippocampal formation (HPF), and olfactory bulb were isolated from non-infected (white bars) and IAV-infected mice (black bars) and used for gene expression analysis. (a) Brain regions were tested for the presence of IAV nucleoprotein mRNA during the acute (7 dpi) and late phase of IAV infection (10 dpi). Viral nucleoprotein remained undetectable at all time points. (b, c) Gene expression levels of type I (*Ifnb1*) and type II interferons (*Ifng*) were examined by RT-qPCR during IAV infection (7-14 dpi) and revealed a significant upregulation in the cortex 14 dpi. (d-g) Induction of interferon-stimulated genes was analyzed during the late phase of IAV infection (10-14 dpi). In the cortex of IAV-infected mice, levels of *Irgm1* were significantly elevated 10 dpi. Data are shown as mean ± SEM and groups were compared via Student's *t*-test with Welch's correction. Significant differences are indicated by * ($p < 0.05$). (adapted from [142])

Under homeostatic conditions, trafficking of nutrients, metabolites, leukocytes, or pathogens to the CNS is highly regulated by its barriers, such as the BBB, or BCSFB located in the CP [18, 107]. The expression of tight junction proteins such as ZO-1, Claudin-1, and Claudin-5 [22, 146] allow the formation of a tightly sealed, continuous layer of endothelial cells that forms the BBB [16] with low paracellular and transcellular permeability [20, 147, 148].

Previous studies have shown, that in addition the induction of an anti-viral state, type I and type II interferons can have stabilizing and destabilizing effects on the barrier properties of the BBB by modulating the expression, downregulation, or internalization of tight junction proteins [149–151]. Moreover, IFN-γ signaling promotes the expression of lymphocyte chemoattractants by endothelial cells of the BBB. Therefore, gene expression of barrier-associated tight junction proteins *Cldn1* (Claudin-1), *Cldn5* (Claudin-5), *Tjp1* (ZO-1), and the chemokines CXCL9 and CXCL10 was examined in brains of mice during the acute phase of IAV infection

(Figure 9a-e) [152–154]. Although levels of *Cldn1* (Figure 9a, CTX, $p < 0.25$, 10 dpi) and of the chemokines *Cxcl9* and *Cxcl10* did not show a clear trend towards IAV infection-induced changes, *Cldn5* and *Tjp1* displayed a significant reduction in cortex and hippocampus 7 dpi.

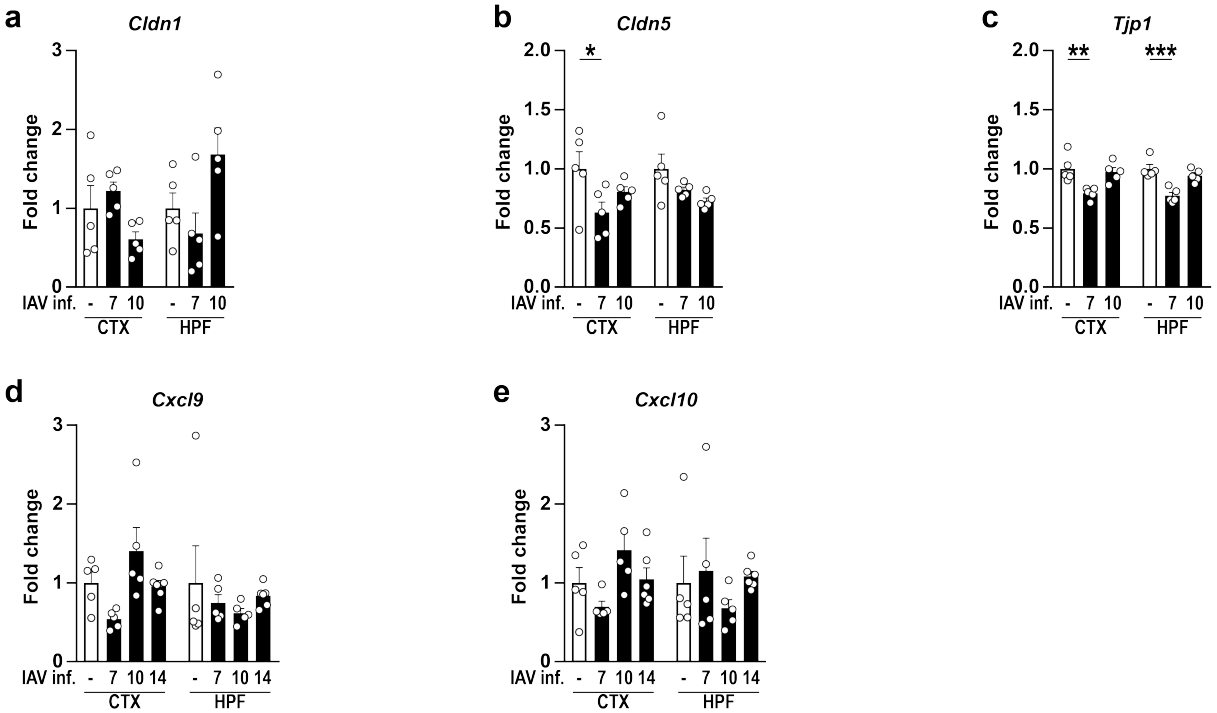

Figure 9: Gene expression levels of blood-brain barrier-associated proteins are temporally reduced upon IAV infection.
(a-c) Gene expression of blood-brain barrier-associated proteins Claudin-1 (*Cldn1*), Claudin-5 (*Cldn5*) and ZO-1 (*Tjp1*) was examined in cortex (CTX) and hippocampus (HPF) of non-infected (white bars) and IAV-infected animals (black bars) during the acute (7 dpi) and late phase of IAV infection (10 dpi). Here, a significant reduction in the expression level was determined for Claudin-5 and ZO-1 7 dpi. (d, e) Level of chemokine mRNA expression was assessed for *Cxcl9* and *Cxcl10* during the course of IAV infection (7-14 dpi) but displayed not alteration. Data are shown as mean ± SEM and groups were compared via Student's *t*-test with Welch's correction. Significant differences are indicated by ** ($p < 0.01$, *** $p < 0.001$). (adapted from [142])

Taken together, peripheral infection with the influenza A virus led to high local concentrations of GM-CSF, IFN-β, IFN-γ, IL-1β, IL-6, IL-10, CCL2, and TNF in the lungs and high levels of IFN-γ and IL-6 in the blood serum. This observation was followed by an increased gene expression of IFN-β and IFN-γ in the brain combined with a reduction of tight junction proteins Claudin-5 and ZO-1, suggesting an impaired functionality of the BBB and BCSFB and a neuroinflammatory response.

3.3. HISTOPATHOLOGY DOES NOT REVEAL CHANGES IN BRAINS OF MICE INFECTED WITH IAV

Consecutively, histopathological examination was conducted using sagittal paraffin sections prepared from non-infected and IAV-infected animals in order to evaluate the inflammatory condition of the CNS. First, paraffin sections were stained against the cytoskeleton-associated protein microtubule associated protein 2 (MAP2) being localized in the dendrites of healthy neurons [155]. Previously, several studies have highlighted its rapid degradation upon brain injury, thus making it a common marker used to study neurodegeneration [156, 157]. When compared to non-infected controls, no structural differences of neuronal cells or appearance of damaged areas were detectable in the brains of IAV-infected mice 14 or 21 dpi (Figure 10a, c). These initial observations were confirmed by detailed examination of the cortex and hippocampus regions with higher magnification (Figure 10c). In addition, paraffin sections were stained against the neuronal nuclei (NeuN) protein, which shows high immunoreactivity to most post-mitotic neuronal cell types [158], hence representing an established and widely used biomarker for diagnostic histopathology [159] (Figure 10b, d). In line with the previous observations of MAP2 staining, no obvious structural differences were observed in mouse brains upon peripheral IAV infection (Figure 10b). Further, both cortex and hippocampus revealed no changes in the density of neuronal nuclei 14 or 21 dpi when compared to non-infected controls (Figure 10d).

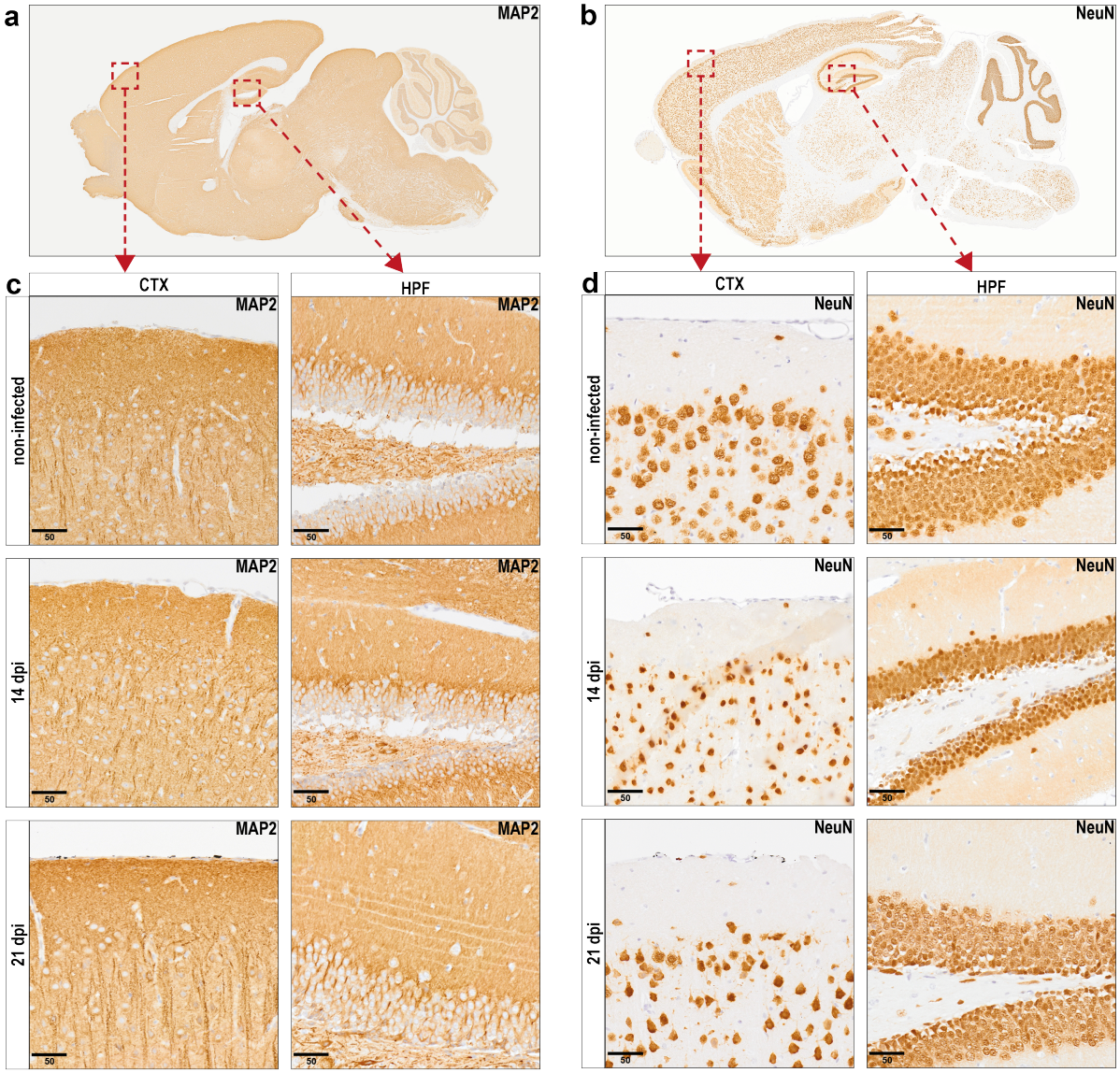

Figure 10: Histopathological examination of neuronal cells in brain tissue upon IAV infection.
Sagittal paraffin sections from brains of non-infected and IAV-infected mice were prepared as described above and examined upon immunohistochemical staining against neuronal markers MAP2 (a) or NeuN (b). No obvious changes or neuronal lesions were detectable upon IAV infection. (c, d) Left panels show the cortex (CTX) and right panels display the hippocampus (HPF) upon 40X magnification. Scale bars = 50 µm. (adapted from [142])

Of note, neuronal damage upon brain injury often elicits activation of microglial cells [160]. Under homeostatic conditions, microglial cells represent the majority of the brain's immune cell population and perform a variety of tasks in order to shape the neuronal network and maintain tissue homeostasis [83, 161, 162]. During steady state, microglia can be characterized by a highly ramified morphology with numerous thin processes continuously surveilling the brain parenchyma and intensely interacting with neighboring cells [79, 84]. When encountering path-

ogen- or damage-associated molecular patterns, these cells become activated, retract their extensions and become highly mobile while migrating towards the sites of inflammation [83] where they accumulate and efficiently phagocytose dead cells or debris [82, 160].

In order to visualize changes in microglia homeostasis and localization, paraffin sections were stained against ionized calcium binding adapter molecule 1 (IBA1) and the CR3 subunit CD11b, both well-known to label microglial surfaces and to be upregulated upon their activation [69, 162, 163] (Figure 11). In line with the previous analysis of neuronal markers MAP2 and NeuN, no differences were observed in histopathological examination of microglia in brains of IAV-infected mice: $IBA1^+$ cells retained a ramified morphology in the cortex and hippocampus and no formation of inflammatory foci was detectable (Figure 11a, c) 14 or 21 dpi. Similarly, $CD11b^+$ cells in brains of infected mice did not differ in morphology and size when compared to non-infected controls (Figure 11b, d).

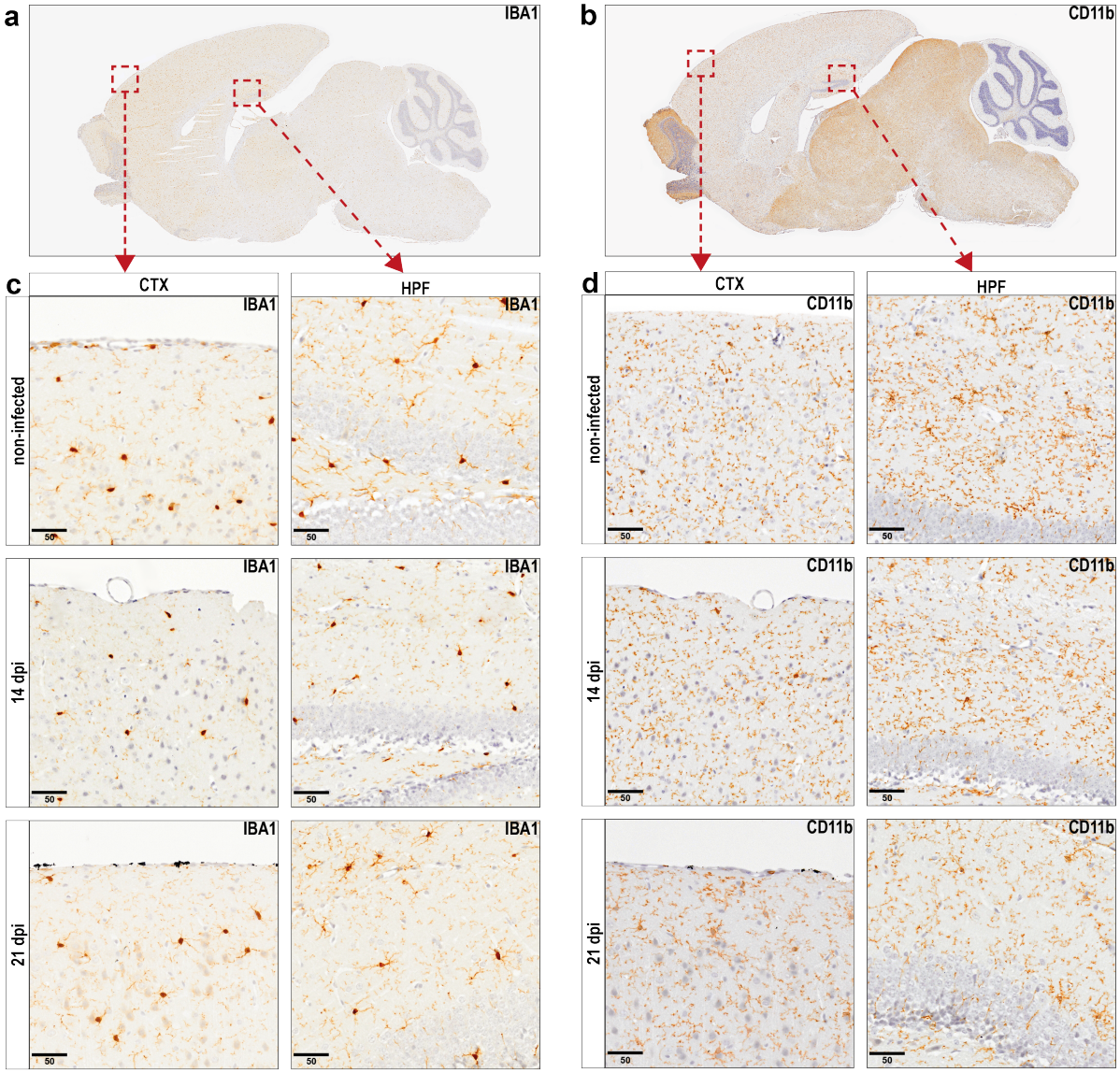

Figure 11: Histopathological examination of microglial cells in brain tissue upon IAV infection.
Sagittal paraffin sections from brains of non-infected and IAV-infected mice were used for histopathological examination upon immunohistochemical staining against immunological markers IBA1 (a) or CD11b (b). No differences were observed in the number and morphology of IBA1- and CD11b-positive cells. (c, d) Left panels show the cortex (CTX) and right panels display the hippocampus (HPF) upon 40X magnification. Scale bars = 50 µm. (adapted from [142])

Nonetheless, surface expression of IBA1 and CD11b is not exclusive to microglial cells only but also a feature of infiltrating monocytes or border-associated macrophages. Therefore, a previous study suggested the cell surface protein transmembrane protein 119 (TMEM119) as a new microglia-specific marker that is not expressed by perivascular macrophages or infiltrating myeloid cells [164]. In the light of decreased gene expression of barrier-associated proteins, this study aimed to confirm whether the cells observed during histopathological examination

indeed represent microglia. Thus, immunofluorescence microscopy of cryosections was employed together with co-staining for TMEM119 and IBA1 (Figure 12a).

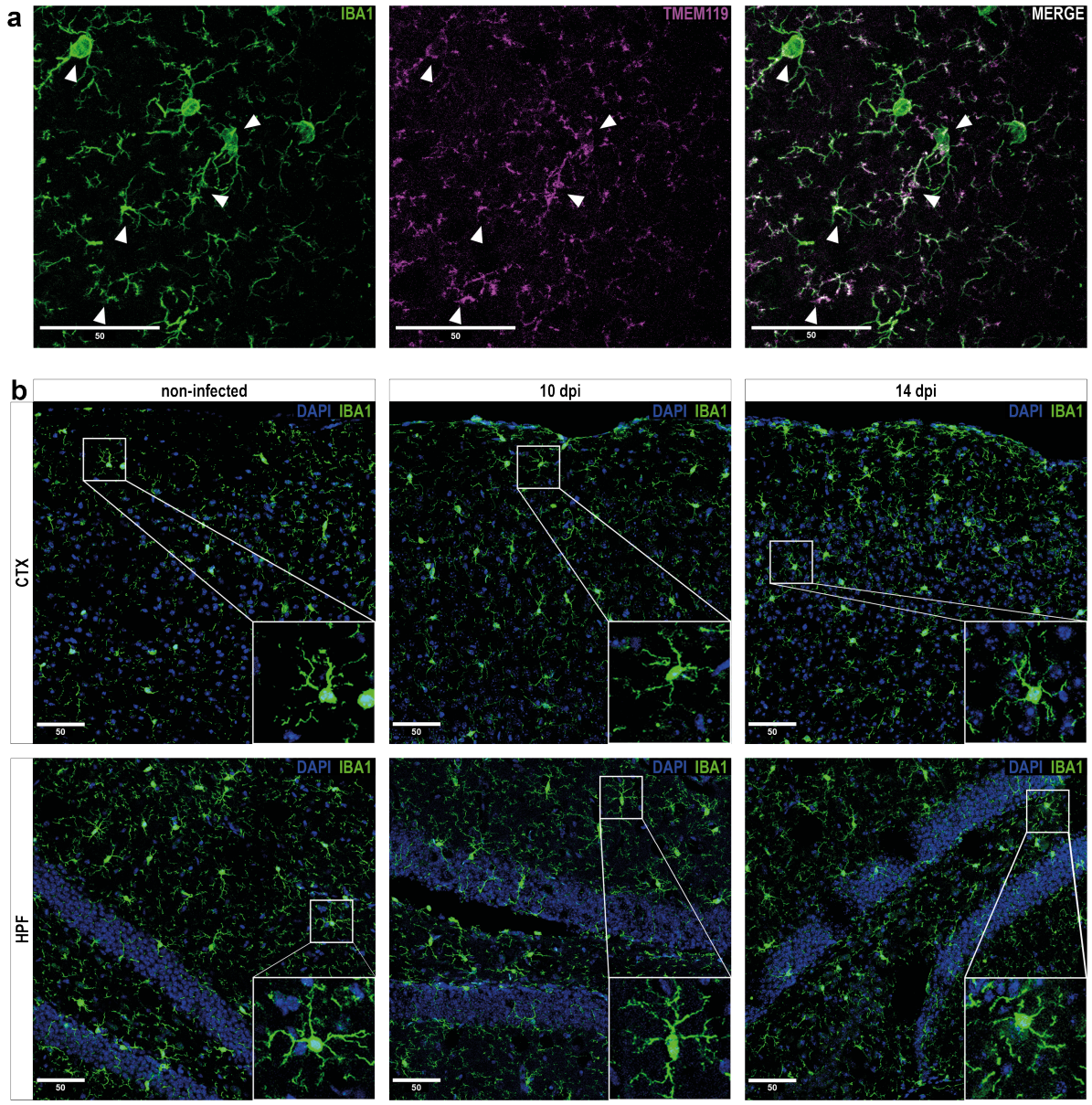

Figure 12: Immunofluorescence microscopical analysis of microglia morphology.
Cryosections of brains from non-infected and IAV-infected mice were prepared and stained against IBA1 and TMEM119 prior to fluorescence microscopy. (a) Panels show representative images of microglial cells co-stained with IBA1 and TMEM119 upon 20X magnification. White arrows indicate strongly overlapping signals of cellular processes in both detection channels. However, signal intensity was stronger for IBA1 and allowed a more detailed morphological evaluation than TMEM119. (b) Microglial cell morphology was investigated by staining of cryosections from non-infected (top panels) and IAV-infected mice (middle and bottom panels) against IBA1 in cortex (CTX, left panels) and hippocampus (HPF, right panels) using a 20X objective. Inserts on bottom right corners show selected microglial cells with higher detail. In non-infected controls and infected animals 10 and 14 dpi, microglia morphology and ramification remained unchanged. Scale bar = 50 µm. (adapted from [142])

Although a robust expression of TMEM119 and a substantial overlap of signal between IBA1 and TMEM119 were detected, TMEM119 did not allow a detailed evaluation of microglia morphology as it was rather present on their cellular processes but not the soma. However, it allowed for the conclusion that the majority of IBA1-positive cells in the investigated samples constitute of microglia. Hence, cryosections from non-infected and IAV-infected mice were further used to compare microglia morphology in the cortex and hippocampus with more detail (Figure 12b). Coherent with the previous histological observations of paraffin sections, microglia in the cortex and hippocampus retained their ramified morphology with thin extensions after 10 and 14 dpi.

In summary, histopathology and IF microscopy revealed no obvious evidence of pathological changes in neuronal or microglial cells in the brain 10, 14, and 21 dpi.

3.4. FLOW CYTOMETRIC CHARACTERIZATION OF IMMUNE CELLS IN THE CNS REVEALED DISTINCT ALTERATIONS UPON IAV INFECTION

In the last decades, microglial cells were described to switch from a resting and anti-inflammatory phenotype to a proinflammatory, activated phenotype upon sensing inflammatory stimuli. However, a growing body of evidence generated from transcriptome and proteome analyses has shown that transformation of microglia occurs as a continuum [79] and that these cells possess a much more diverse phenotypic spectrum with multidimensional activation profiles that manifest depending on the surrounding microenvironment [165, 166]. In this context, post-mortem analysis of microglial morphology from cortex samples revealed the simultaneous presence of ramified, primed, reactive, and amoeboid phenotypes in the absence of neurological or inflammatory illness [167], thus raising the question about a direct correlation of morphology and activation of microglial cells during pathology [79]. In order to characterize the influence of peripheral IAV-infection on microglial activation in more detail, immune cells were isolated from brains of non-infected and IAV-infected mice and their phenotypes were analyzed via multiparametric flow cytometry (Figure 13). First, the overall immune cell subsets in the brain were subjected to unsupervised *t*-distributed stochastic neighbor embedding (*t*-SNE) to obtain an unbiased impression on the present cell populations. This algorithm utilizes machine learning and probability distribution to perform a nonlinear reduction of dimensions in order to allow

the visualization of high-dimensional flow cytometric data in a two-dimensional plot. In brief, similar datapoints will be clustered together, whereas different datapoints will be mapped further apart [168, 169]. For cells isolated from brains of non-infected and IAV-infected mice, this process ultimately resulted in three major clusters (Figure 13a) that displayed distinct surface expression levels of CD45, CD11b, CX_3CR1, and MHC class II as indicated by a yellow-to-orange color code and showed minor differences in the expression of MHC class I, CD80, CD86, and F4/80.

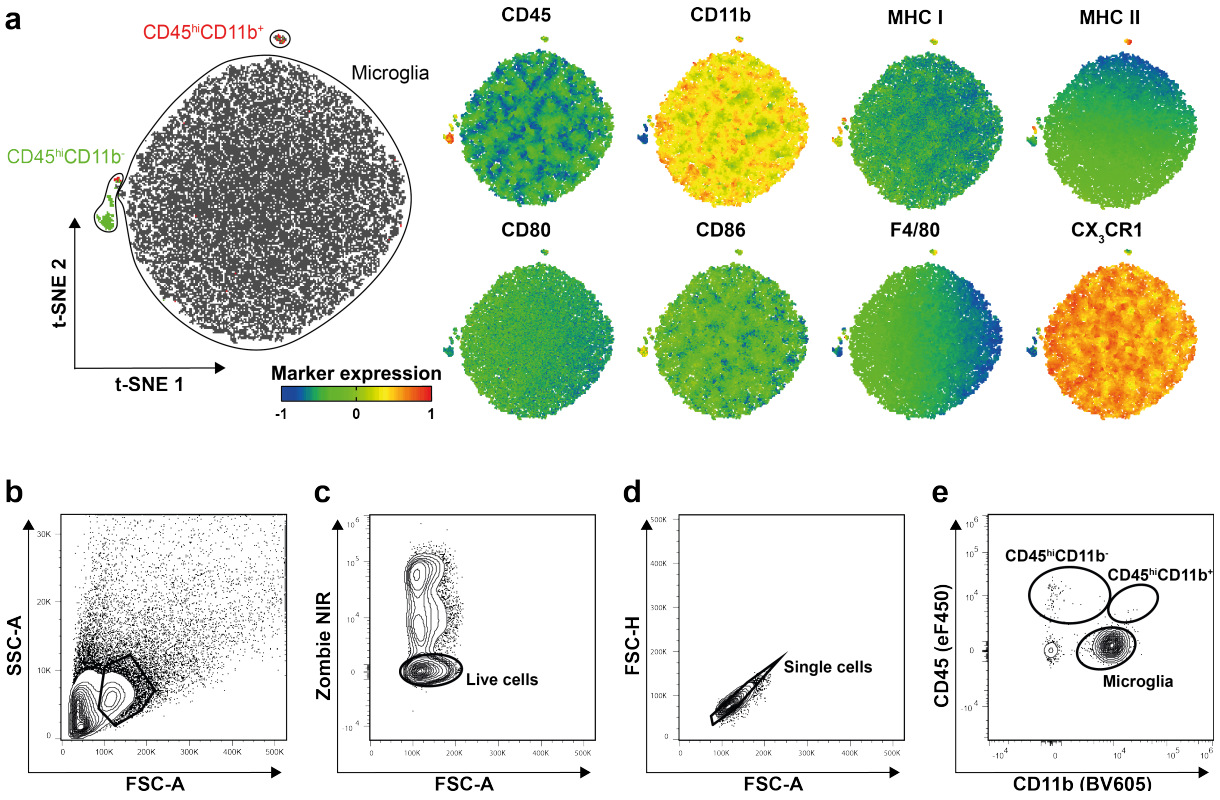

Figure 13: Unsupervised clustering reveals three major immune cell subsets in brains of IAV-infected mice. Immune cells from cortex and hippocampus of non-infected and IAV-infected mice were isolated as described above. Cells were analyzed by flow cytometry and subsequently subjected to unsupervised clustering using the *t*-distributed stochastic neighbor embedding (*t*-SNE). The clustering resulted in three distinct populations. (a) Clusters formed by *t*-SNE were first identified by manual gating (see panels [b-e] below) and further compared for the surface expression of different markers. Differences were observed in the surface expression of CD45, CD11b, CX_3CR1, and MHC class II. (b-e) Representative gating strategy used to identify previously generated clusters. First, cells were selected based on their size and granularity in the forward scatter (FSC-A) and side scatter (SSC-A) plot (b). Then, dead cells were excluded by only selecting events negative for the live/dead dye Zombie NIR (c) and living cells were further compared by FSC-H and FSC-A to discriminate the singlets (d). (e) Finally, single cells were separated by their expression of CD45 and CD11b into brain-resident $CD45^{low}CD11b^{+}$ microglial cells, recruited $CD45^{hi}CD11b^{+}$, and $CD45^{hi}CD11b^{-}$ immune cells. (adapted from [142])

In accordance with previously published data [170], a subsequent manual gating approach revealed that cells within the three different clusters consisted of brain-resident microglial cells ($CD45^{low}CD11b^{+}$) and peripheral immune cell subsets of lymphoid $CD45^{hi}CD11b^{-}$ and myeloid

$CD45^{hi}CD11b^{+}$ origin (Figure 13b). Further, applying the manual gating provided information on the frequency of each cell population within the different brain regions and samples. When comparing the frequencies of microglial cells, $CD45^{hi}CD11b^{-}$, and $CD45^{hi}CD11b^{+}$ cells between non-infected and IAV-infected animals 7 dpi, a significant increase was detected for $CD45^{hi}CD11b^{+}$ cells (Figure 14b, non-infected: 0.58 ± 0.18 %, IAV-infected: 1.41 ± 0.24 %). With progressing infection, this difference manifested for $CD45^{hi}CD11b^{+}$ cells in the cortex (Figure 14e, non-infected: 0.06 ± 0.02 %, IAV-infected: 0.12 ± 0.02 %) and became also apparent for $CD45^{hi}CD11b^{-}$ in the hippocampus (Figure 14f, non-infected: 0.5 ± 0.19 %, IAV-infected: 1.13 ± 0.13 %) of IAV-infected mice 10 dpi. Upon 14 dpi, the fraction of $CD45^{hi}CD11b^{+}$ cells returned to levels of non-infected controls in cortex (Figure 14h, non-infected: 0.12 ± 0.02 %, IAV-infected: 0.14 ± 0.02 %) and hippocampus (non-infected: 0.2 ± 0.04 %, IAV-infected: 0.25 ± 0.07 %), whereas the $CD45^{hi}CD11b^{-}$ cell population remained elevated in the cortex (Figure 14i, non-infected: 0.24 ± 0.03 %, IAV-infected: 0.4 ± 0.02 %) of infected mice. Nevertheless, microglial cells constituted by far the largest population of immune cells at all time points and thus confirmed previous data obtained by immunofluorescence microscopy and histopathology.

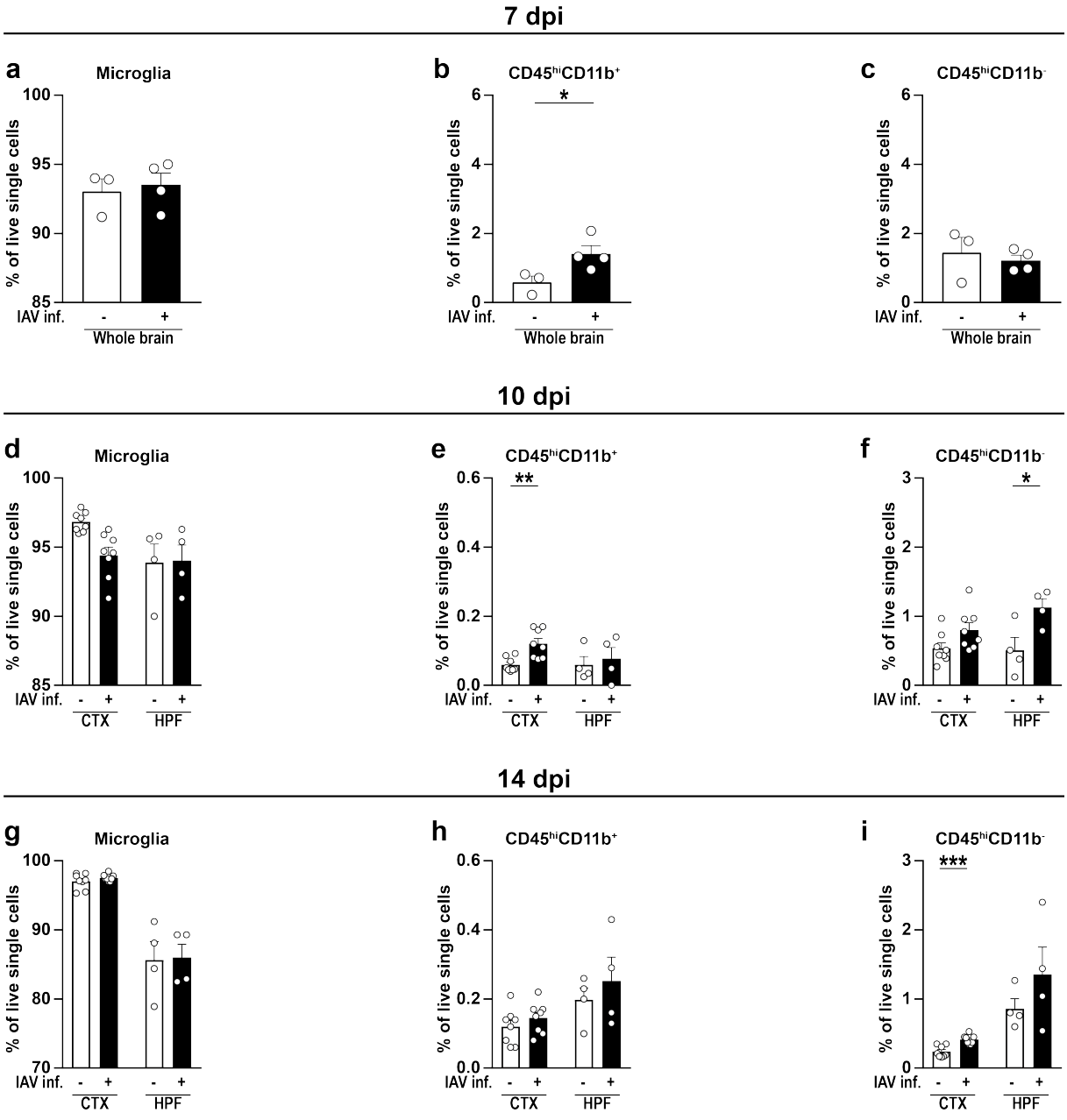

Figure 14: Frequency of immune cell subsets is altered upon IAV infection.
(a-c) Bar charts show the frequencies of isolated immune cells from whole brains of non-infected (white bars) and IAV-infected mice (black bars) 7 dpi. (d-i) Plots depict the region-specific immune cell frequencies in cortex (CTX) and hippocampus (HPF) of non-infected (white bars) and IAV-infected mice 10 and 14 dpi. Upon IAV infection, a significant increase in $CD45^{hi}CD11b^{+}$ and $CD45^{hi}CD11b^{-}$ immune cells was observed in the brain. Data are shown as mean ± SEM and groups were compared via multiple *t*-tests with Holm-Sidac *post-hoc* correction. Significant differences are indicated by * ($p < 0.05$, ** $p < 0.01$, *** $p < 0.001$). (adapted from [142])

Next to the differentiation of immune cell subsets by flow cytometry, the surface expression of immunological markers was analyzed for microglial cells in the cortex and hippocampus 10 and 14 dpi (Figure 15). Here, median fluorescence intensities (MFI) of several immunological markers were found at different levels 10 dpi, translating into an overall increased microglia activation. Microglial cells of infected mice expressed higher levels of MHC I and II, CD80,

and F4/80, whereas expression of the fractalkine receptor CX_3CR1 was reduced. Upon 14 dpi, microglial activation was still evident in both examined brain regions with significantly increased MFIs of MHC I and F4/80 and decreased MFIs of CX_3CR1, respectively. However, the alterations were not as pronounced as before, suggesting a return to baseline levels after resolution of peripheral IAV infection.

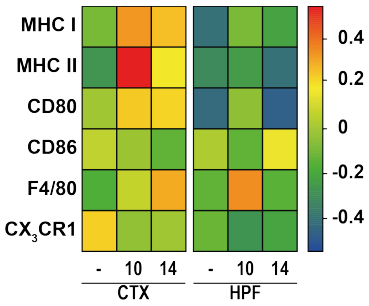

Figure 15: Flow cytometric characterization of microglial cells reveals increased activation status in IAV-infected mice.
Microglial surface expression of MHC I, MHC II, CD80, CD86, F4/80, and CX_3CR1 was determined by flow cytometry in cortex (CTX) and hippocampus (HPF) of non-infected and mice infected with IAV on 10 and 14 dpi. Data indicate an increased surface expression of MHC I and II, CD80, and F4/80 by microglial cells 10 and 14 days after IAV infection. Relative expression was calculated by normalizing the median fluorescence intensity of respective markers to their overall mean and the resulting heatmap plot was created using R with "lattice" package. (adapted from [142])

In addition to the analysis of MFIs, percental changes in the fractions of microglia expressing the measured surface markers were determined (Figure 16). Similar to the previously observed alterations upon infection, significantly more microglia expressed MHC I and II, CD80, and F4/80 in the cortex, whereas in the hippocampus MHC I and F4/80 increased 10 dpi (Figure 16a-f). Thereafter, frequencies of activated microglia declined 14 dpi and only remained significantly changed for F4/80-expressing microglia in the cortex of IAV-infected mice (Figure 16k).

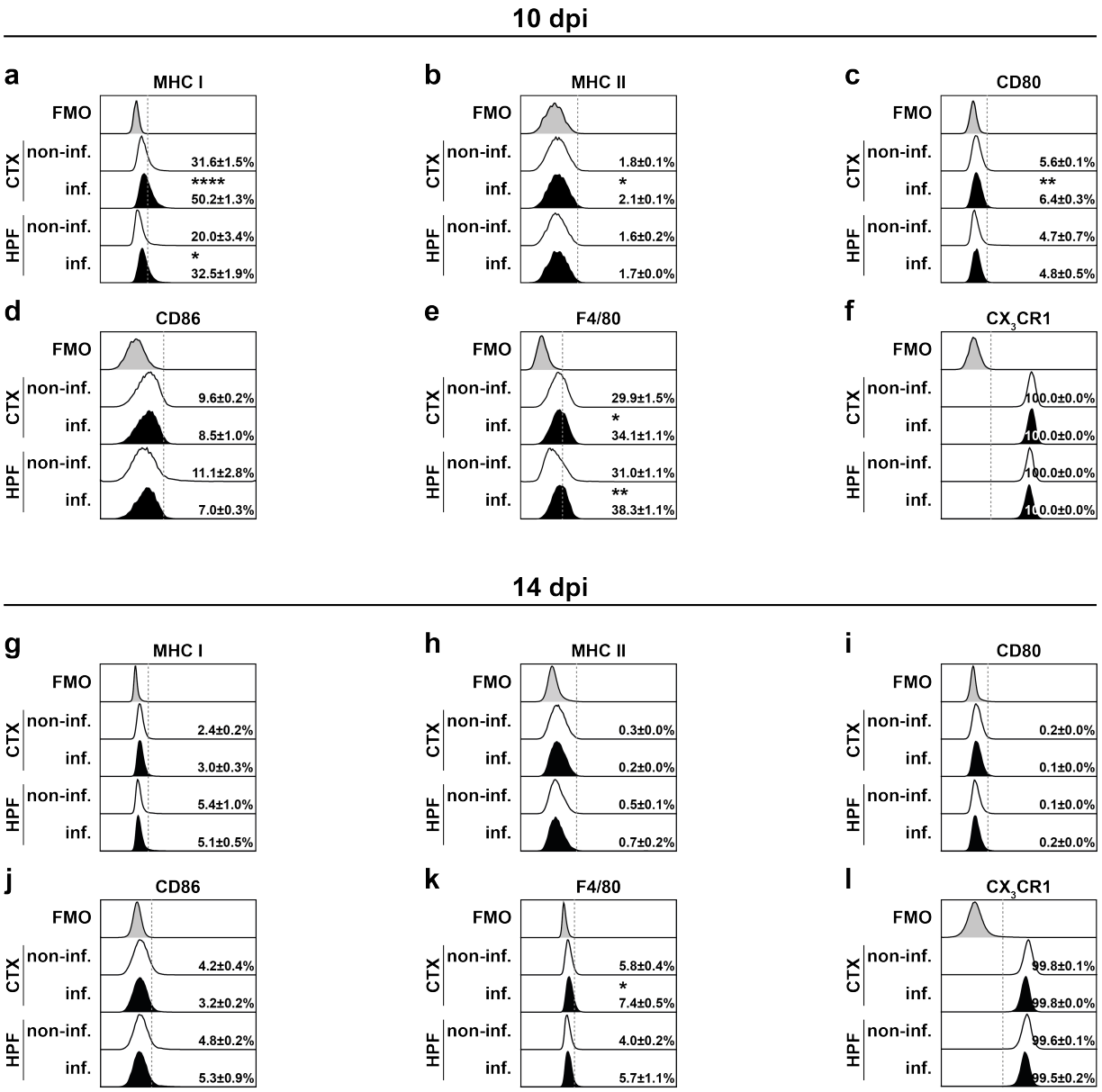

Figure 16: Detailed phenotypical characterization of microglial cells.
Histogram plots display the frequencies of microglial cells expressing MHC I, MHC II, CD80, CD86, F4/80, and CX_3CR1 in cortex (CTX) and hippocampus (HPF) of non-infected (without tint) and IAV-infected mice (black tint) 10 dpi (a-f) and 14 dpi (g-l) in correspondence to fluorescence-minus-one (FMO) controls (grey tint). In line with the higher MFIs shown above, a larger fraction of microglial cells expressed MHC I and II, CD80, and F4/80 upon IAV infection. Dashed vertical lines indicate cutoff of background fluorescence and numbers show percentage of cells expressing the surface marker. Data are shown as mean ± SEM and groups were compared via Student's *t*-test with Welch's correction. Significant differences are indicated by * ($p < 0.05$, ** $p < 0.01$, **** $p < 0.0001$). (adapted from [142])

Taken together, multiparametric flow cytometric analysis of immune cells from brains of IAV-infected mice supported the previous findings of an altered BBB by revealing an elevated number of recruited peripheral immune cells in the brain parenchyma. Furthermore, activation of brain-resident microglia was increased upon IAV infection and remained elevated until 14 dpi.

3.5. DYSREGULATION OF SYNAPTIC PRUNING UPON IAV INFECTION-INDUCED MICROGLIA ACTIVATION

Microglial cells have been described to shape neuronal connections via pruning of excessive synapses [84, 89], a process which several studies have highlighted to be a hallmark of different neurological disorders [69, 171, 172]. Here, the phagocytosis of synapses by microglia is mediated by “eat me” signals expressed by neurons, that tag synapses for microglial engulfment [69, 161]. Interestingly, inflammatory stress has been hypothesized to increase exposure of such signals by neurons [89]. In this context, it remains noteworthy that influenza infection has been shown to cause cognitive dysfunction, leading to an altered neuronal architecture in mice [130]. Given the increased microglial activation observed in brains of IAV-infected mice, the question arose whether microglia-mediated synaptic pruning could also be reactivated. Therefore, the gene expression of phagocytosis-associated receptors was analyzed in the cortex and hippocampus upon influenza infection (Figure 17).

Upon 10 dpi, the gene expression of the scavenger receptor *Cd36* and lysosomal-associated protein *Cd68* remained unaffected in both cortex and hippocampus, however, their expression was significantly increased upon sustained pro-inflammatory triggers seen 14 dpi (Figure 17a, b). Next to the upregulation of specific microglial receptors, synaptic pruning further requires expression of complement components to tag synapses [173]. Hence, mRNA levels of *C1qa* and *C3* were assessed consequently. Similar to phagocytosis-associated receptors, complement factors showed a likewise increase 14 dpi in cortex and hippocampus, providing the prerequisites for synapse elimination (Figure 17e, f). In contrast, mRNA levels of *Trem2*, an innate immune receptor implicated in cell activation and phagocytosis [174], and the inducible nitric oxide synthase (*Nos2*) remained unaffected upon IAV infection (Figure 17c, d).

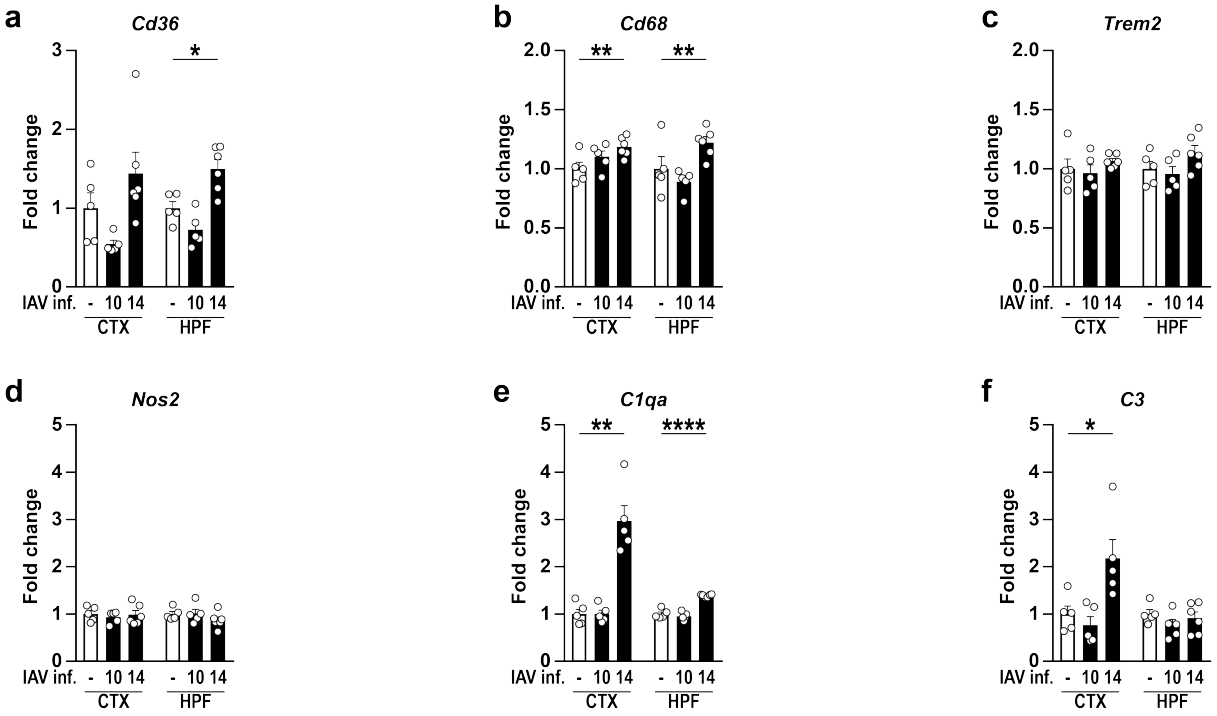

Figure 17: Expression levels of phagocytosis-associated genes and complement factors is increased upon IAV infection.
Gene expression of phagocytosis-associated genes (a-c), inducible nitric oxide synthetase (d), and complement factors was measured by RT-qPCR in cortex (CTX) and hippocampus (HPF) of non-infected (white bars) and IAV-infected mice (black bars) during the late phase of infection (10-14 dpi). Upon 14 dpi, a significant increase in the gene expression of *Cd36*, *Cd68*, *C1qa*, and *C3* was observed in the brain. Data are shown as mean ± SEM and groups were compared via Student's *t*-test with Welch's correction. Significant differences are indicated by * ($p < 0.05$, ** $p < 0.01$, **** $p < 0.0001$). (adapted from [142])

In conclusion, the data presented suggest the dysregulation of synaptic pruning and altered synaptic function following IAV infection.

3.6. TEMPORALLY DYSREGULATED GLUTAMATERGIC SYNAPSE TRANSMISSION AND NEUROTROPHIN GENE EXPRESSION FOLLOWING RESOLUTION OF PERIPHERAL IAV INFECTION

Besides the dysregulation of synaptic pruning, neuroinflammation is linked to the release of cytokines such as IFN-γ which is capable of interfering with cellular homeostasis of neurons and even neurotransmission [175]. Due to the significant increase of interferon-stimulated genes in the brains of IAV-infected mice, it remained to be determined whether peripheral infection with IAV may also affect synapse function. To this end, the gene expression of the presynaptic VGLUT1 (*Slc17a7*) was characterized over the course of infection (Figure 18). When

compared to non-infected samples, gene expression of VGLUT1 did not differ significantly 10 and 14 dpi, however, mRNA levels tended to decrease 14 dpi ($p < 0.29$). When assessing the expression levels 21 dpi to address possible long-term effects of IAV infection, the expression of *Slc17a7* significantly increased, indicating an overcompensatory response.

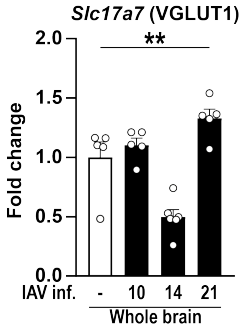

Figure 18: Gene expression of VGLUT1 is disturbed upon IAV infection.
Gene expression of the pre-synaptic VGLUT1 (*Slc17a7*) was assessed by RT-qPCR in brains of non-infected (white bars) and IAV-infected mice (black bars) during the late phase of infection (10-14 dpi) and 21 dpi. Data are shown as mean ± SEM and groups were compared via Student's *t*-test with Welch's correction. Significant differences are indicated by ** ($p < 0.01$). (adapted from [142])

To further assess whether the altered VGLUT1 gene expression negatively affects glutamatergic synapse transmission, this study directly addressed VGLUT1 protein levels at the synapse level by taking advantage of synaptosomes, i.e. sealed pre-synaptic nerve terminals often containing opposite post-synaptic elements. Upon adaption of pre-existing synaptosome isolation protocols using discontinuous density gradient centrifugation [137], the isolated synaptosomes were first pictured via transmission electron microscopy (Figure 19a, b): The imaged synaptosomes show single fragments of membranes and intact pre-synapses adjacent to thickened post-synapses with total diameters of 350-700 nm. Furthermore, pre-synaptic sides contain zero to one mitochondrion and many small, clear synaptic vesicles, whereas post-synaptic densities and the synaptic cleft are well noticeable. Next, proteins were isolated from synaptosome samples of non-infected and IAV-infected animals to determine protein levels of VGLUT1 by Western blot analysis (Figure 19c, d). Here, levels of VGLUT1 were diminished 14 dpi ($p < 0.09$) and significantly reduced 21 dpi, thus confirming previous findings by RT-qPCR.

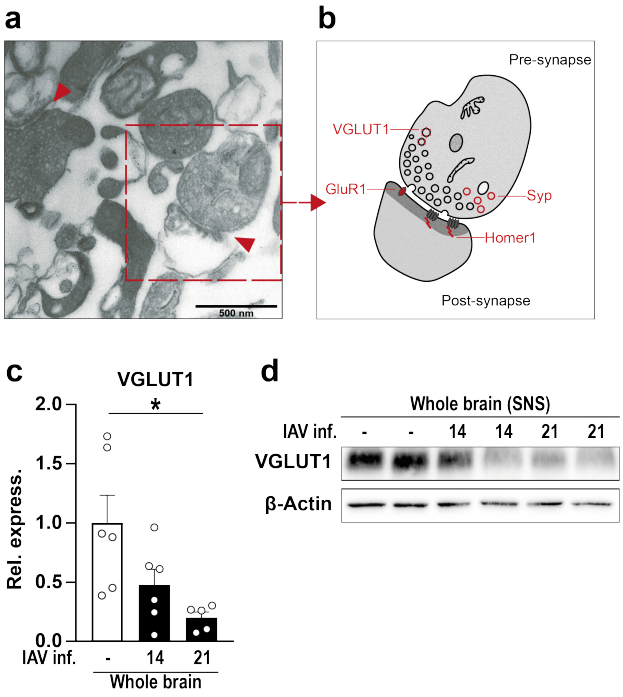

Figure 19: Western blot analysis of VGLUT1 from isolated synaptic particles.
Synaptosomes were isolated from whole brain homogenate of non-infected and IAV-infected mice as described above and used for further analysis. (a) Panel shows representative picture of isolated synaptosomes captured via transmission electron microscopy. Red arrows indicate intact synapses consisting of pre- and post-synaptic compartments. Scale bar = 500 nm. (b) Graphical illustration of selected synaptosome in (a). Pre-synaptic compartment contains synaptic vesicles and mitochondria, post-synaptic domain harbors the region of high post-synaptic density with different structural proteins. Highlighted structures aim to visualize localization of different synaptic proteins under physiological conditions. (c-d) Western blot analysis of pre-synaptic vesicular glutamate transporter VGLUT1 in synaptosomal fractions of whole brain homogenate from non-infected and IAV-infected mice 14 and 21 dpi. Bar charts display the relative optical density of the protein bands in (d) upon normalization to abundance of β-Actin. Values were further normalized to the mean of the non-infected group and compared by one-way ANOVA with Holm-Sidak *post-hoc* correction. Data are shown as mean ± SEM and significant difference is indicated by * ($p < 0.05$). (adapted from [142])

Thus far, protein levels in synaptosomes have been mostly analyzed in batches [138] and only few studies are known to employ quantitative approaches [176, 177]. To allow the quantitative comprehension of synaptic protein abundance within individual synapses, flow synaptometry was established as a novel, flow cytometry-based approach to perform high-throughput analysis of synaptosomes.

Reportedly, synaptosomes are rather small with diameters from 0.5-2 µm [178, 179]. In the light of conventional flow cytometers displaying poor resolution of forward-scatter light signals for objects of such small scale, certain measures became necessary to allow the detection and size discrimination of synaptosomal events (Figure 20). First, a size gate ranging from 300-1000 nm was established by utilizing red-fluorescent silica beads with defined diameters (Figure 20a). To overcome the limitations caused by low detector sensitivity, the lipophilic styryl dye FM4-64 that becomes highly fluorescent when bound to lipid bilayers was used to label cellular components (Figure 20b). Thus, signal noise caused by inorganic residues in the buffer and objects small enough to pass through the 0.22-µm pores of conventional sterile filters could be excluded by replacing the standard FSC-triggered detection with a fluorescence-triggered detection in BL3 of the flow cytometer (Figure 20c) [138]. Subsequently, only FM4-64-stained events within the established size gate were examined for the presence of VGLUT1

(Figure 20d). Finally, synaptosomes isolated from whole brains of non-infected and IAV-infected mice were compared and revealed a significant reduction of VGLUT1$^+$ events 21 dpi, whereas no differences appeared 14 dpi (Figure 20e).

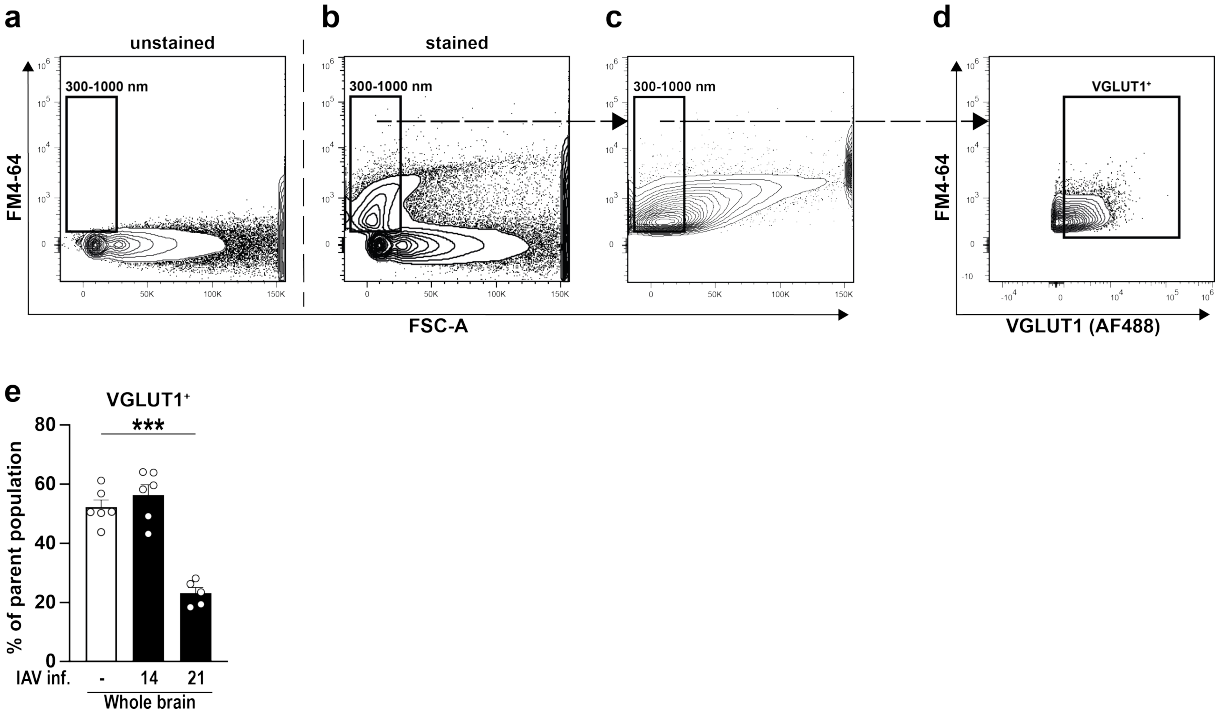

Figure 20: Characterization of pre-synaptic VGLUT1 in IAV-infected mice by flow synaptometry.
Synaptosomes from whole brain homogenate of non-infected and IAV-infected animals were subjected to flow synaptometry which revealed a significant reduction of VGLUT1$^+$ events 21 dpi when compared to non-infected controls. (a-d) Panels depict the basic flow cytometer settings and the representative gating strategy used. (a) At first, a size gate of 300-1000 nm was established in the FSC channel by utilizing fluorescent silica beads with specific diameters. (b) Then, the styryl dye FM4-64 was applied to synaptosomal preparations to label biological membranes, thus allowing the replacement of FSC-triggered detection by fluorescence-triggered detection in BL3 with a threshold set to 0.3×10^3 (c). (d) Events positive for the dye FM4-64 and within the size range of 300-1000 nm were then gated for their signal of VGLUT1. (e) Bar charts show the frequency of VGLUT1$^+$ events in the brains of non-infected (white bars) and IAV-infected animals (black bars) 14 and 21 dpi. Upon 21 dpi, the frequency of VLGUT1$^+$ synaptosomes was significantly reduced. Data are shown as mean ± SEM and groups were compared via Student's *t*-test with Welch's correction. Significant differences are indicated by *** ($p < 0.001$). (adapted from [142])

Thus, these findings confirmed the previous Western blot analysis results that also indicated a significant reduction of VGLUT1 in IAV-infected mice 21 dpi, but at higher sensitivity and a reduced variance between samples. Given the substantial changes of VGLUT1, the next step was to narrow down the synaptosome analysis onto the specific brain regions of cortex and hippocampus of IAV-infected mice (Figure 21). Therefore, the staining panel was expanded by specific markers for the pre-synapse (Syp, Figure 21b) and post-synapse to allow the analysis of intact synaptosomes while simultaneously differentiating between excitatory (Homer1) and

inhibitory synapses (Gephyrin) (Figure 21c). When compared to non-infected mice, no differences in the frequency of excitatory Syp$^+$Homer1$^+$ or inhibitory Syp$^+$Gephyrin$^+$ synaptosomes were observed in cortex and hippocampus of infected animals 14 dpi (Figure 21d, e).

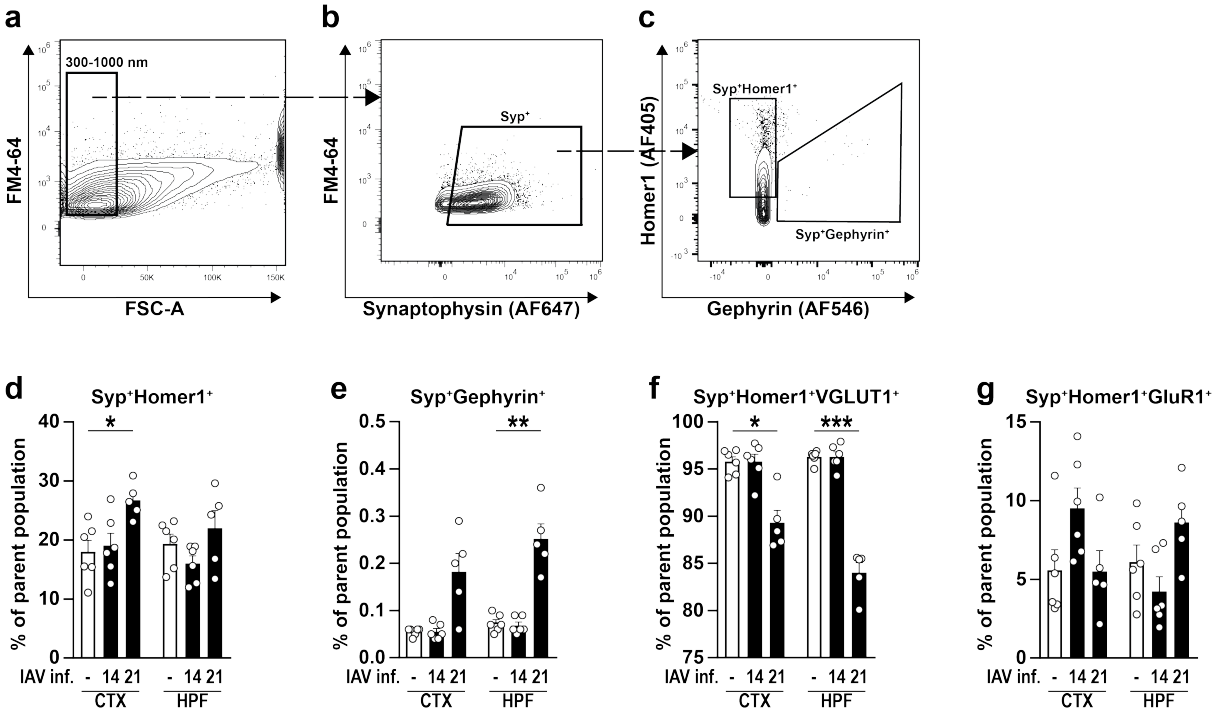

Figure 21: Flow synaptometry reveals altered glutamatergic signaling upon IAV infection.
Synaptosomes were isolated and analyzed by flow synaptometry to reveal a significant loss of Syp$^+$Homer1$^+$VGLUT1$^+$ synaptosomes in the cortex and hippocampus 21 dpi. (a-c) Panels show representative gating strategy used for synaptosome samples. (a) First, FM4-64$^+$ events were gated for 300-1000 nm size in the FSC channel. (b) Next, only Synaptophysin$^+$ (Syp$^+$) objects were selected and further discriminated by their expression of post-synaptic Homer1 (Syp$^+$Homer1$^+$, i.e. excitatory synapses) or Gephyrin (Syp$^+$Gepyhrin$^+$, i.e. inhibitory synapses) to ensure analysis of intact synaptosomes (c). (d-f) Bar charts display the frequencies of synaptosomes from cortex (CTX) and hippocampus (HPF) of non-infected (white bars) and IAV-infected animals (black bars) 14 and 21 dpi. Upon 21 dpi, the frequency of Syp$^+$Homer1$^+$ synaptosomes was significantly increased in the cortex of infected mice, whereas the frequency of Syp$^+$Gepyhrin$^+$ synaptosomes from inhibitory synapses was increased in the hippocampus. (f-g) Synaptosomes from excitatory synapses were further characterized by their expression of pre-synaptic VGLUT1 (Syp$^+$Homer1$^+$VGLUT1$^+$) and post-synaptic AMPA receptor subunit GluR1 (Syp$^+$Homer1$^+$GluR1$^+$). In line with the findings shown in Figure 20 above, the frequency of Syp$^+$Homer1$^+$VGLUT1$^+$ synaptosomes was strongly reduced in the cortex and hippocampus upon IAV infection. In contrast, no differences were observed for Syp$^+$Homer1$^+$GluR1$^+$ synaptosomes. Data are shown as mean ± SEM and groups were compared via Student's *t*-test with Welch's correction. Significant differences are indicated by * ($p < 0.05$, ** $p < 0.01$, *** $p < 0.001$). (adapted from [142])

Upon 21 dpi, an increased frequency of Syp$^+$Homer1$^+$ synaptosomes was detected in Cortices of infected mice, whereas Syp$^+$Gephyrin$^+$ synaptosomes from inhibitory synapses were significantly more abundant in the hippocampus. Moreover, the fractions of excitatory synapses positive for either VGLUT1 or AMPA receptor subunit GluR1 were determined among the population of Syp$^+$Homer1$^+$ synaptosomes to evaluate whether IAV infection affects glutamatergic

signaling at both pre- and post-synapses (Figure 21f, g). Here, results from the cortex and hippocampus of IAV-infected animals 14 dpi were consistent with previous findings in Western blot analysis (see Figure 19) or flow synaptometry of whole brain homogenate (see Figure 20) and did not differ from non-infected controls. In contrast, a substantial loss of $Syp^+Homer1^+VGLUT1^+$ synaptosomes was detected in the cortex and hippocampus 21 dpi, whereas frequencies of $Syp^+Homer1^+GluR1^+$ synaptosomes from either cortex or hippocampus were not significantly altered in the course of an IAV infection.

Previously, studies using the viral mimic poly(I:C) to induce peripheral inflammation have discovered changes in the glutamatergic signaling and synapse transmission [180] with analogies to pathophysiological inflammation-induced depression, where low levels of the neurotransmitter serotonin are assumed to play a major role. As serotonin levels mainly rely on tryptophan availability which is in turn limited by the activity of indoleamine 2,3-dioxygenase (IDO) as a part of the kynurenine pathway [181, 182], and IDO being inducible via IFN-γ, IL-1β, and IL-6 [183–185], or upon IAV infection [186], this study aimed to characterize mRNA levels of *Ido* in brains of mice upon IAV infection (Figure 22). In the cortex and hippocampus, abundance of *Ido* mRNA transcripts did not show an increase upon IAV infection and remained below the detection limit in particular samples.

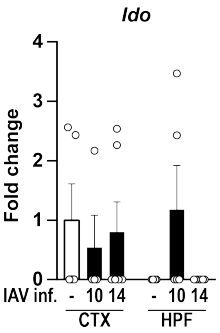

Figure 22: Gene expression of indoleamine 2,3-dioxygenase is not altered in brains upon IAV infection.
Gene expression of indoleamine 2,3-dioxygenase (*Ido*) was determined by RT-qPCR in cortex (CTX) and hippocampus (HPF) of non-infected (white bars) and IAV-infected mice (black bars) during the late phase of infection (10-14 dpi). Data are shown as mean ± SEM and groups were compared via Student's *t*-test with Welch's correction.

Finally, the question remained to be addressed whether the evident synaptic changes might, at least in part, be the result of impaired neurotrophin levels. These proteins act as important mediators of neuronal survival and differentiation in the CNS and therefore play a crucial role during the development of the brain and in synaptic plasticity [54, 187]. Previously, it has been shown that neuroinflammation is able to alter the levels of neurotrophins and patients with neurodegenerative disorders often display reduced neurotrophin concentrations in their brain [188]. Hence, neurotrophin gene expression was determined by RT-qPCR in cortex and hippocampus 0, 10, 14, and 21 dpi (Figure 23**)**. The levels of brain-derived neurotropic factor (*Bdnf*) and

nerve growth factor (*Ngf*), both important mediators of neuronal differentiation and survival, remained unchanged until 14 dpi (Figure 23a, b). Upon 21 dpi, expression of *Bdnf* showed a substantial reduction in cortex and hippocampus, whereas mRNA levels of *Ngf* were significantly increased in the hippocampus. Furthermore, the expression of the BDNF-specific neurotrophin receptor TrkB (*Ntrk2*) was significantly elevated in both brain regions 21 dpi (Figure 23c). The pan-neurotrophin receptor $p75^{NTR}$ (*Ngfr*), known to be differentially expressed during various neurodegenerative diseases [50, 189], remained unaltered throughout the course of IAV infection (Figure 23d).

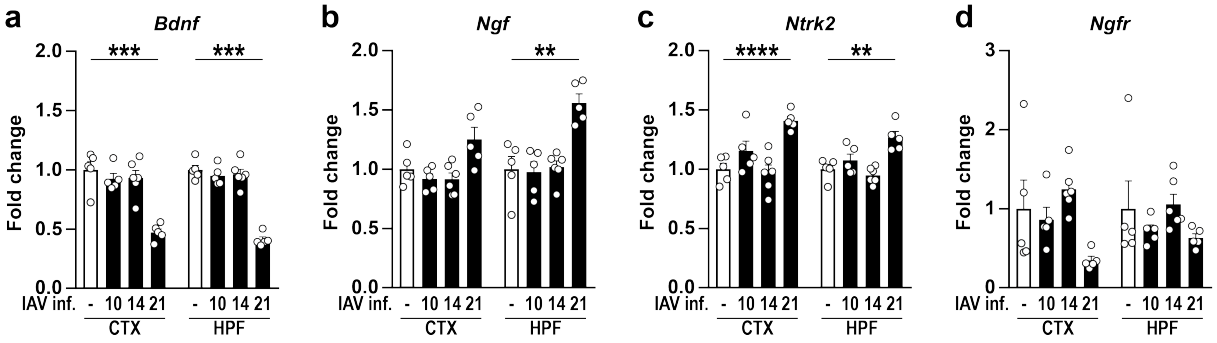

Figure 23: Gene expression of neurotrophins upon IAV infection.
(a, b) Gene expression levels of neurotrophins BDNF (*Bdnf*) and NGF (*Ngf*) as well as neurotrophin receptors TrkB (*Ntrk2*) and $p75^{NTR}$ (*Ngfr*) were analyzed in cortex (CTX) and hippocampus (HPF) of non-infected (white bars) and IAV-infected animals (10-21 dpi). Upon 21 dpi, a significant reduction of BDNF mRNA levels was detected in the cortex and hippocampus of IAV-infected animals. In contrast, gene expression levels of NGF and TrkB were substantially increased. Data are shown as mean ± SEM and groups were compared via Student's *t*-test with Welch's correction. Significant differences are indicated by ** ($p < 0.01$, *** $p < 0.001$, **** $p < 0.0001$). (adapted from [142])

Altogether, this work is able to demonstrate the change in mRNA levels of type I interferons and BBB-associated proteins, such as Claudin-5 and ZO-1, upon peripheral inflammation caused by IAV infection. In addition, flow cytometric characterization of microglial cells revealed an increased surface expression of MHC I and II, CD80, and F4/80, whereas no obvious morphological differences were detected in histopathological examination of sagittal brain sections. Moreover, an altered microglia activation status was further indicated by elevated gene expression levels of phagocytosis-associated proteins CD36 and CD68, and complement factors C1Qa and C3. By establishing a new high-throughput approach to analyze and quantify protein levels in single synapses, this study revealed an increased frequency of inhibitory synapses, and diminished VGLUT1 in excitatory synapses following IAV infection. Finally, the detection of a disturbed gene expression of the neurotrophins BDNF and NGF, and the neurotrophin receptor TrkB further pointed towards an altered homeostasis of the CNS upon IAV infection.

4. DISCUSSION

Infections with influenza A virus affect all age groups and accumulate in annual epidemics. Usually, the infection is associated with "flu symptoms" including fever, cough, and a sore throat but also induces symptoms of sickness behavior such as reduced social interactions, anorexia and weight loss [121, 190]. Accordingly, several studies utilizing models of LPS-induced sepsis or the application of the viral mimic poly(I:C) have ascribed this altered behavior and disturbed brain homeostasis to pyrogenic cytokines released during the acute phase response [122, 130, 143–145]. In contrast to infections with neurotropic pathogens that have been shown to induce neuroinflammation and neurological manifestations, such as *Plasmodium falciparum* [191], *Toxoplasma gondii* [192, 193], or West Nile virus [194], neuroinflammatory effects of respiratory IAV infection remain largely elusive. Previously, cases of behavioral alterations in the form of narcolepsy [195] and the development of major depression [129] have been linked to IAV infection in humans, while animal experiments further complemented the picture by illustrating an impaired hippocampal neuron morphology and cognition in the presence of neuroinflammation in mice [130, 131]. Overall, various findings suggest the body-brain axis as link between peripheral infection and the development of neuropsychiatric disorders, however, the underlying mechanisms remain unknown.

4.1. INDUCTION OF SYSTEMIC INFLAMMATION BY IAV CAUSES DISTURBANCE OF BBB AND BRAIN HOMEOSTASIS

Therefore, this study aimed to investigate alterations in the CNS upon mild infection with IAV, representing the majority of human cases. To this end, the murine experimental model in combination with the mouse-adapted laboratory strain PR8/A/34(H1N1) was utilized during the experiments. Previously, the genetic host background has been demonstrated to be crucial for the susceptibility against influenza virus infection [196]. The report further indicated that C57BL/6J mice, although lacking the important host defense gene *Mx1*, are resistant to infection with PR8/A/34(H1N1) and consequently, suitable to mimic a human course of infection.

Accordingly, an elevated concentration of cytokines in lungs and sera was monitored during the first days of infection. Particularly, increased levels of IFN-β, IL-1β, and IL-6 in the lungs 5 dpi point out a strong activation of the innate immune response followed by high levels of IFN-γ 7 dpi, which coincided with a prominent loss of bodyweight indicating sickness behavior in these mice. These data are in line with previous observations [133] and are the result of a cellular and humoral immune response by the adaptive immune system, facilitated by cytotoxic $CD8^+$ T cells, and IFN-γ-producing natural killer and $CD4^+$ T helper cells that lead to diminished viral burden in the lungs [197].

In addition, enhanced cytokine levels were detected in the blood serum of mice during the course of IAV infection. Although the magnitude was lower when compared to cytokine concentrations in the lungs, IFN-γ and IL-6 displayed significant increases when compared to non-infected controls. This observation confirms, that the inflammatory effects of an IAV-mediated infection of the respiratory tract are not restricted to this local environment alone but cumulate in a systemic inflammation. Similarly, the induction of peripheral inflammation through administration of LPS, poly(I:C) or IAV has been shown to cause elevated serum levels of IL-6 and TNF, which led to increased expression of inflammatory cytokines in the brain [130, 198–200]. This immune-to-brain signaling is thought to be dependent on the vagus nerve, CVOs, or endothelial cells of the BBB that transport cytokines into the CNS [123, 124, 127, 128]. In addition, a recent study has demonstrated that cerebral endothelial cells are early responders to acute systemic inflammation and display the induction of immediate early response genes and the NF-κB pathway [201]. Altogether, it is hypothesized that high serum titers of pro-inflammatory cytokines IL-1β, IL-6, and TNF may induce a mirrored response in the brain via the activation of astrocytes and microglial cells [202, 203] which are then able to release IL-1β, IL-6, and TNF in return [75, 79]. Consequently, mRNA levels of *Il1b*, *Il6*, *Tnf*, and *Ccl2* were assessed in brains of mice during the course of IAV infection. Here, cytokine gene expression did not differ in cortex or hippocampus when compared to non-infected controls. However, the assays performed are representative for brain homogenate and thus do not translate into cell-specific activation of astrocytes or microglia. In addition, microglial cells have been shown to form a spatially heterogeneous population in the adult brain [204] and this study investigated the cortex and hippocampus. Hence, it remains to be addressed if microglia and astrocyte subsets respond differently to acute systemic inflammation in other brain regions upon IAV infection.

Although no change in the gene expression of pyrogenic cytokines was detected, a moderate but significant increase of type I interferons (*Ifnb1*) and the IFN-γ-inducible GTPase *Irgm1* was

found in the cortex of infected mice 10 dpi. Of note, the present data and other previous studies could show that IAV PR8/A/34(H1N1) lacks the ability to infect the brain [130, 131]. Previous reports have demonstrated that microglia are producers of type I interferons upon activation [202, 203]. Noteworthy, the magnitude of *Ifnb1* expression levels remained considerably low and did not lead to a more restricted permeability of the BBB as observed in other studies [205, 206]: Here, treatment of brain capillary endothelial cells with IFN-β *in vitro* increased the transendothelial electrical resistance while inhibiting paracellular diffusion of inulin and sucrose [205]. Similarly, intraperitoneal injection of IFN-β prevented infiltration of neutrophils and decreased gene expression of matrix metalloproteinase 9 in a model of ischemic brain injury [206]. In contrast, the gene expression of BBB-associated tight junction proteins Claudin-5 and ZO-1 was diminished in IAV-infected mice 7 dpi, shortly after serum levels of IFN-γ peaked. The dysregulated state of BBB and BCSFB was further indicated by the marginally increased frequencies of peripheral immune cells that were detected in cortex and hippocampus between 7 and 14 dpi. These results are in line with a recent report demonstrating the ability of exogenous IFN-γ to induce the internalization of Occludin by epithelial cells *in vitro* [207]. Similarly, a different study assigned IFN-γ a central role in the cytokine network in rabies virus-infected mouse brains, leading to enhanced BBB permeability via downregulation of Claudin-5, Occludin, and ZO-1 gene expression upon infection [208]. Although IFN-γ is further able to promote the expression of chemokines CXCL9 and CXCL10 by the BBB and BCSFB [175, 209], gene expression of *Cxcl9* or *Cxcl10* in the brain homogenate of IAV-infected mice revealed no difference in contrast to a previous report on poly(I:C)-induced release of CXCL10 by brain endothelial cells. In the latter study the authors associated the induction of sickness behavior in mice with BBB- and BCSFB-derived CXCL10, further leading to aggravated hippocampal synaptic plasticity via CXCR3 signaling in neurons [145]. Of note, both poly(I:C) and IAV infection result in RIG-I signaling cascade induction with downstream activation of MAVS and induction of NF-κB and IRF3 [116, 117]. However, only IAV is able to avoid immune responses by directly interfering with cellular signaling pathways or host gene expression that ultimately disturb induction of interferons and antiviral proteins. For example, the viral NS1 can interfere with RIG-I signal transduction and the resulting IFN-mediated antiviral response [210–212]. Thus poly(I:C)-induced inflammation can only partially translate into effects observed in the IAV infection model of this work. Altogether, further investigation of the contribution of brain endothelial and epithelial cells to chemokine and cytokine release upon IAV infection is required. In line with previous reports, such investigations could scrutinize transcriptome analysis

from primary or purified brain endothelial cells to disentangle their role in transducing peripheral inflammation into the brain upon IAV infection [145].

4.2. IAV INFECTION DOES NOT RESULT IN OBVIOUS HISTOPATHOLOGICAL CHANGES

Although the altered expression of IFN-β and ISGs in the brain could suggest the onset of neuroinflammatory processes upon peripheral infection with IAV, histological examination using IBA1, CD11b, NeuN or Synaptophysin did not show noticeable inflammatory foci in cortex and hippocampus of infected mice. Still, it is noteworthy to mention, that the use of other antibodies might allow the visualization of microglial activation via microscopy. In this respect, microglia number and their ramified morphology remained unaltered throughout the course of IAV infection which partially collides with data of Jurgens et *al.* [130] showing increased IBA1 staining and reduced ramification of microglia already 7 dpi. However, those findings may just be the result of a different genetic background (BALB/c *vs.* C57BL/6JRj) and a higher IAV inoculation dose as both loss of bodyweight and locomotive activity of mice appeared at least 2 days earlier than in the present study, using only 0.32 $TCID_{50}$ of IAV to induce the infection. Presumably, the immune system responds proportionally to the infection dose and in the experiments of this work, animals had only a mild loss of bodyweight and did not succumb to the infection. However, whether the indirect activation of brain-resident cells by peripheral challenge is similarly proportional to the severity of the acute systemic inflammation, i.e. a higher inoculation dose, is an interesting point that awaits further elucidation. Noteworthy, astrocytes can also respond to inflammatory stimuli and astrogliosis indicated by increased expression of glial fibrillary acidic protein is a hallmark of various CNS pathologies [213]. Furthermore, astrocytes have been proposed to quickly react to LPS-induced systemic inflammation given that their end-feet, being in close proximity of blood vessels, express cytokine receptors [214]. In addition, a previous report has shown that intracellular Ca^{2+} levels in astrocytes increase upon stimulation with prostaglandin E2 [215], which is produced and released by BBB endothelial cells in response to pyrogenic cytokines [122]. Therefore, the time and extent of astrocyte activation may precede microglia activation and thus represent an important question to be addressed in future studies. To this end, astrocytes may be either characterized by IF microscopy using anti-GFAP staining, or as recently described, by flow cytometry using GFAP in combi-

nation with C3 and glutamate-aspartate transporter [216]. Altogether, a more quantitative analysis of the astrocyte activation state during the initial and acute phase of IAV could help to expand the existing paradigm of systemic inflammation-induced alteration of CNS homeostasis.

4.3. SYSTEMIC INFLAMMATION INDUCES DELAYED MICROGLIAL CELL ACTIVATION

Besides morphological changes, microglia activation can appear on multidimensional scale [165, 166] and includes a continuum of altered gene expression, migration, metabolism, and functional changes, such as phagocytosis [79]. Indeed, detailed investigation via flow cytometry detected no difference in microglia frequency upon IAV infection, arguing against microglia proliferation as the result of reactive microgliosis and further supporting the previous observations from histological examination. However, a significant region-specific activation of microglia was observed as indicated by increased surface expression of MHC I and F4/80 10 dpi and 14 dpi. Altogether, these results support a delayed onset of microglia activation following a peripheral immune response. Moreover, the data suggest that IAV infection induces a rather subtle and short-term inflammation in the brain, which might remain unnoticed using common histopathological approaches. Intriguingly, when mice infected with IAV PR8/A/34(H1N1) were assessed for possible long-term effects 30 dpi, no signs of neuroinflammation were apparent at all [131]. Similar observations have been made in a recent study where the transcriptome of activated microglia in an LPS-induced sepsis model was indistinguishable from microglia of PBS-treated controls when compared four weeks after treatment [217].

Yet, the number of markers used within this work to determine the microglial activation status via flow cytometry was limited and does not allow a comprehensive evaluation with respect to the proposed continuum of microglia activation. In this context, a study using the combination of single-cell RNA sequencing and multicolor flow cytometry to detect downregulated homeostatic features and upregulation of inflammatory genes in microglia upon LPS treatment revealed unexpected heterogeneity in their transcriptomes [170]. Although all microglial cells responded similarly to acute systemic inflammation with increased expression of *Ccl2*, *Tnf* or G protein-coupled receptor 84 (*Gpr84*), *t*-SNE clustering revealed a microglia subset less sensitive to inflammatory stimuli, an observation that was not made in the present study. However,

in contrast to a single-dose LPS, IAV infection yields in a multi-facetted, ongoing systemic inflammation that could lead to a more homogeneous activation pattern of microglia. Therefore, a multi-omics characterization of microglial cells across different brain regions would provide more detailed information to this question by addressing either the transcriptome, cell surface properties, or the extent of epigenetic modification in order to unravel the high dimensionality of microglia activation upon IAV infection.

4.4. MICROGLIAL ACTIVATION COULD LEAD TO INCREASED SYNAPTIC PRUNING

A growing body of evidence has emphasized the connection between inflammation-induced activation of microglia and the recurring pruning of synapses in neurological disorders [69, 171, 172]. Therefore, the expression of genes related to phagocytosis and synaptic pruning was analyzed in this study. In brains of IAV infected mice, mRNA levels of *Cd36* and *Cd68* were found upregulated, proposing a higher phagocytic capacity of microglial cells. Besides the prerequisite of activated microglia, synaptic pruning is depending on components of the classical complement cascade which tag synapses for a possible elimination [173, 218]. For example, complement factors can bind to extracellular phosphatidyl serine on neurons which is exposed at higher levels upon stress [219, 220]. In this context, a previous study has shown that microglial engulfment of synapses is particularly dependent on the phagocytic receptor CR3 binding to its ligand C3 and disruption of CR3 signaling in microglia resulted in impaired remodeling of developing synapses [221]. In line with increased mRNA levels of phagocytosis-associated genes, gene expression of complement components *C1qa* and *C3* was also found increased in IAV-infected animals, altogether suggesting the dysregulation of synaptic pruning. Of note, experimental approaches utilizing cell-specific genetic ablation have recently identified microglial cells as the main source of C1QA in the CNS in a mouse model of AD [222]. Thus, the data presented by this work furthermore illustrate the activation microglia but moreover highlight the contribution of astrocytes which have been associated with the release of C3 upon induction of NF-κB signaling [223]. Intriguingly, these results were apparent only 14 dpi, indicating once again temporary repercussions in the nervous system upon peripheral inflammation. Still, whether neuronal morphology and the number of synapses is indeed impaired in brains of IAV-infected mice cannot be answered by gene expression analysis alone but requires additional and more sophisticated experimental approaches. For example, whether synapses indeed

undergo recurring pruning by activated microglia may be analyzed via co-staining of phagocytosis-associated proteins, such as CD68, with microglial cell markers and synaptic proteins, and the consequent IF microscopical analysis of overlapping signals. Alternatively, microglial engulfment of synapses can be studied using experimental *ex vivo* phagocytosis assays, e.g. by incubating microglia isolated from brains of IAV-infected mice with fluorescence-labeled synaptosomes and subsequent flow cytometric analysis. Furthermore, it remains important to confirm the tagging of synapses by components of the complement system, such as C1QA and C3, using either microscopic or flow synaptometric approaches. Finally, changes in neuronal morphology in the course of mild IAV infection as seen in this work could be addressed by Sholl analysis to quantify the number of dendritic branches at a given distance from the soma in order to better evaluate alterations in the dendritic complexity.

4.5. ESTABLISHMENT OF FLOW SYNAPTOMETRY

The elevated mRNA levels of *Irgm1* in combination with reduced gene expression of *Slc17a7* implied adverse effects of IAV infection on synapse integrity. In this regard, recent reports have demonstrated impairment of synaptic function upon infection-induced neuroinflammation. Here, the immune response in the brain was accompanied by the release of pro-inflammatory cytokines IL-1β, IL-6, TNF, but also IFN-γ, which subsequently resulted in diminished levels of Synaptophysin, EAAT2 as well as AMPA and NMDA receptor subunits [224, 225]. To gather more detailed information about synaptic alterations, this work focused on studying the properties of synapses themselves and detected a significant loss of pre-synaptic VGLUT1 in isolated synaptosomes from whole brain homogenate 21 dpi, suggesting that the systemic inflammation driven by peripheral IAV infection causes a functional disturbance in excitatory neurons in mice. This assumption is supported by previous reports showing altered hippocampal neuron morphology and cognitive impairment, as indicated by decreased dendritic spine density and spatial learning in the Morris water maze [130, 131]. However, Western blot analysis only revealed a holistic view on total protein levels but did not allow a comprehensive and quantitative analysis of individual events. Therefore, a novel flow cytometry-based approach to analyze synaptosomes derived from cortices and hippocampi was established in this study, allowing the quantification of the composition of individual, intact synapses.

To date, investigation of isolated synaptosomes represents a convenient tool to study the function and physiology of synapses freed from their surrounding environment [178]. However,

only few studies have utilized flow cytometric approaches to assess synaptosomes and in most cases only make use of one synaptic component [177, 226, 227]. Other reports focused on sorting of synaptosomes derived from fluorescent neurons [176] or applying mass cytometry and mass-coupled antibodies [228]. However, the profound technique presented in this study offers an easy-to-use alternative to previous approaches as it demonstrates that simple multiplexing is feasible using a conventional isolation procedure and standard flow cytometer. To this day, no other studies have shown to extend previous attempts of flow synaptometry by simultaneously quantifying the relative abundance of pre- and post-synaptic components in synaptosomes from different types of neurons and different brain regions. Moreover, choosing flow synaptometry over conventional Western blot enables to focus specifically on intact synapses, resulting in a high sensitivity while requiring only small amounts of sample material. In addition, high-throughput acquisition allows the characterization of a large number of samples within the same session and thus facilitates a high robustness of data compared to Western blot analysis.

4.6. SYSTEMIC INFLAMMATION CAUSES ALTERED NEUROTRANSMISSION

Consequently, flow synaptometry was able to detect compelling effects on pre-synaptic glutamatergic signaling in both cortex and hippocampus 21 dpi, while the proportion of inhibitory synapses was increased in the hippocampus. Of note, disturbance of the excitatory/inhibitory balance has been proposed to be a crucial feature in schizophrenia [69] but so far, the impact of local inflammation on the balance of excitatory/inhibitory neurotransmission has not been fully elucidated. Recently, *in vitro* studies have either reported decreased glutamatergic but not GABAergic neurotransmission [229, 230], or only decreased GABAergic neurotransmission in response to application of pro-inflammatory cytokines [231]. In this context, a report has demonstrated that LPS-induced neuroinflammation in aged mice resulted in the delayed loss of $VGLUT2^{+}PSD\text{-}95^{+}$ excitatory synaptic puncta in the hippocampus while $VGAT^{+}Gephyrin^{+}$ puncta remained unaffected, suggesting a response specific to excitatory synapses only [232]. In contrast, a different report using treatment of primary hippocampal neurons with conditioned medium obtained from poly(I:C)-stimulated microglia discovered a reduction of $VGAT^{+}$ synapses and strong disruption of perineuronal nets [233]. Altogether, the data gathered thus far are conflicting and require further elucidation. Hence, it remains to be addressed, whether the increased frequency of inhibitory synaptosomes detected in the brains of IAV-infected mice in

this work could reflect a loss of glutamatergic synapses as described before. Moreover, the results obtained in this study only reflect the relative abundance of Gephyrin^{+} synapses but not their functional properties with respect to VGAT protein levels or $GABA_A$ receptor expression. To this end, future studies addressing the balance of excitatory/inhibitory neurotransmission upon IAV infection require further analysis of VGAT levels in synaptosomes upon IAV infection using flow synaptometry, but also electrophysiological recordings to assess possible differences in the neuronal network activity. In addition, the determination of a total synapse abundance via analysis of dendritic spine density is necessary to evaluate changes in synaptic plasticity upon IAV infection.

Similar to the effect of inflammation-induced changes on the homeostasis of inhibitory synapses, little is known about the direct consequences of peripheral infections or inflammation on glutamate homeostasis. A recent report utilizing the viral mimic poly(I:C) discovered elevated extracellular glutamate levels and synaptic transmission in the hippocampus, suggesting a dysregulation of excitatory synaptic transmission as cause for the development of hippocampal hyperexcitability [180]. Alternatively, different underlying mechanisms have been associated with respect to pathophysiological inflammation-induced depression. Here, low levels of the neurotransmitter serotonin are assumed to play a major role and rely mainly on tryptophan availability which is in turn limited by the activity of indoleamine 2,3-dioxygenase (IDO) as a part of the kynurenine pathway [181, 182]. IDO is inducible via IFN-γ, IL-1β, and IL-6 [183–185], as well as upon IAV infection [186]. Degradation of tryptophan occurs through IDO in peripheral organs such as liver, intestine, and spleen [234] but also in brain-resident microglia, astrocytes or recruited monocytes [190, 235]. Additionally, altered levels of serotonin have been associated with a modulation of glutamatergic and GABAergic neurotransmission by altering the release of glutamate and GABA at the pre-synaptic side while further suppressing long-term potentiation (LTP) via inhibition of NMDA glutamate receptor activation [236]. Although an upregulation of IDO mRNA levels in the brains of IAV-infected mice was not detectable in this work, studies using LPS-induced depressive-like behavior models pointed towards a particular role of the kynurenine pathway metabolites rather than altered brain levels of serotonin [237]. Blood-derived metabolites of the kynurenine pathway can enter the brain via large neutral amino acid transporter and cause excitotoxic effects [238]. For example, levels of quinolinic acid, which functions as NMDA agonist, are elevated upon peripheral inflammation [190] and were found responsible for LPS-induced depression [239]. Thus, the observed change

in glutamatergic neurotransmission in the presented study might be a consequence of dysregulated serotonin levels or the underlying tryptophan metabolism.

Next to adverse effects on glutamatergic neurotransmission, IAV infection led to an altered expression of neurotrophins and their receptors. In line with these observations, previous reports also discovered reduced expression levels of BDNF and glia cell-derived neurotrophic factor in brains of IAV-infected mice [130, 240], as well as models of poly(I:C) and LPS administration demonstrating reduced expression of BDNF, TrkB, and NGF in hippocampi and cortices of mice [200, 241]. BDNF has been shown to be an important trophic factor that mediates neuronal survival, dendrite development, and synaptogenesis in an autocrine manner [242, 243]. Unsurprisingly, decreased BDNF levels are associated with the development of depressive symptoms [244–247] and have been further shown to modulate glutamatergic synaptic transmission by affecting pre-synaptic Ca^{2+} levels and glutamate release as well as phosphorylation of post-synaptic NMDA receptors [248]. Of note, studies have shown that glutamate receptor activity has a reciprocal effect on neurotrophin production, indicating a strongly intertwined relationship [200]. Besides its effect on neurons, aggravated BDNF signaling has been moreover implied with reduced microglial cell proliferation and overall density [249]. In the present work, changes in BDNF gene expression remained undetected until 21 dpi, however, this late disturbance may cause sustained interference with microglia homeostasis. As a result, the increased mRNA levels of TrkB could act as a countermeasure to the reduced BDNF levels in order to maintain sufficient BDNF signaling. Next to BDNF, expression of NGF has also been shown to be influenced by inflammation and several studies have reported increased levels of NGF at sites of inflammation [250–252]. In this context, the role of NGF signaling appears to be polyvalent: On the one hand, NGF can potentiate the endogenous expression of pro-inflammatory cytokines and induce survival of immune cells, such as monocytes, neutrophils, and B cells. On the other hand, NGF promotes tissue repair and enhanced production of anti-inflammatory IL-10 [252]. Hence, the increased levels of NGF that were observed in the brains of mice could act as another indicator of the subtle and short-term inflammation caused by IAV infection.

In line with this, gene expression levels of $p75^{NTR}$ remained unchanged in brains of IAV-infected mice. Previously, several reports have shown upregulation of the $p75^{NTR}$ upon neuroinflammation [50, 189, 192]. Yet, the detrimental effects of $p75^{NTR}$-mediated signaling are dependent on pro-neurotrophins, such as proNGF and proBDNF. Under homeostatic conditions

and subsequent to initial synthesis, pro-neurotrophins become processed by protein convertases, Furin, and matrix metalloproteases [54, 189] which have not been studied in this work. Thus, the effect of IAV infection-induced respiratory inflammation on the neurotrophin/pro-neurotrophin balance awaits further elucidation in future studies.

4.7. DISTURBANCE OF GLUTAMATERGIC NEUROTRANSMISSION IS LINKED TO PATHOPSYCHOLOGICAL CHANGES

Notably, inflammation-mediated dysbalance of glutamatergic signaling has been described as a central mechanism in several neurologic disorders such as schizophrenia [253], ASD [254], obsessive-compulsive disorder [255] or mood disorders, and further as a comorbidity in atherosclerosis or rheumatoid arthritis [256]. Overall, the present study shows that peripheral IAV infection is followed by temporal effects (disturbed expression of BBB-associated genes, activation of microglia, increased gene expression of complement components, dysbalanced glutamatergic neurotransmission and neurotrophin gene expression) in the brain, however, without direct manifestation in neurodegenerative processes, as shown by histopathological examination of neuronal markers. Nevertheless, these findings contribute to the understanding how peripheral inflammation affects CNS integrity. Of note, re-infection of humans with influenza is likely to occur in intervals of 10 to 20 years [257] and accumulating effects in the brain could result in neurological implications [258]. In this respect, a growing body of evidence supports the connection between systemic inflammation and epigenetic changes in microglia [259], however with different possible outcomes. On the one hand, repeated LPS treatment of mice induced a sustained inflammatory phenotype in microglia involving the classical complement system and its associated phagosome pathway, finally culminating in the loss of dopaminergic neurons in the substantia nigra as a hallmark of PD [260, 261]. On the other hand, studies reported the induction of immune tolerance in microglial cells upon repeated LPS administration, which resulted in reduced deposition of amyloid-β in AD transgenic mice [262] and the down-regulation of inflammatory NF-κB signaling [217]. Yet, how LPS administration compares to ongoing peripheral inflammation caused by IAV infection with orchestrated secretion of cytokines by innate and adaptive immune cells is not known. Furthermore, it remains to be addressed whether priming and activation by microglia via peripheral stimulation is beneficial or detrimental. It still appears plausible that, as a consequence, synergistic effects of multiple pe-

ripheral infections acquired throughout life could lead to a previously unappreciated contribution in the development of chronic neuroinflammation, contributing to the initiation and progression of neuropsychiatric or neurodegenerative diseases such as major depression, AD or PD [263, 264]. Studies on sickness behavior in humans have shown that these behavioral alterations overlap with symptoms of inflammation-induced depression, suggesting that maladaptive, chronic immune activation can precede depression [265, 266]. Correspondingly, previous reports identified IAV infection as a risk factor for PD or the development of PD-like symptoms [267–269].

5. SUMMARY AND OUTLOOK

Infections with influenza A virus can re-occur throughout life and are accompanied by inflammation of the respiratory tract and the periphery, and further include symptoms of sickness behavior. In addition to previous observations, this work has demonstrated that respiratory infection with IAV PR8/A/34(H1N1) results in the chronologically separated disturbance of the BBB and BCSFB, distinct activation of microglia, dysbalanced glutamatergic neurotransmission and neurotrophin gene expression (Figure 24).

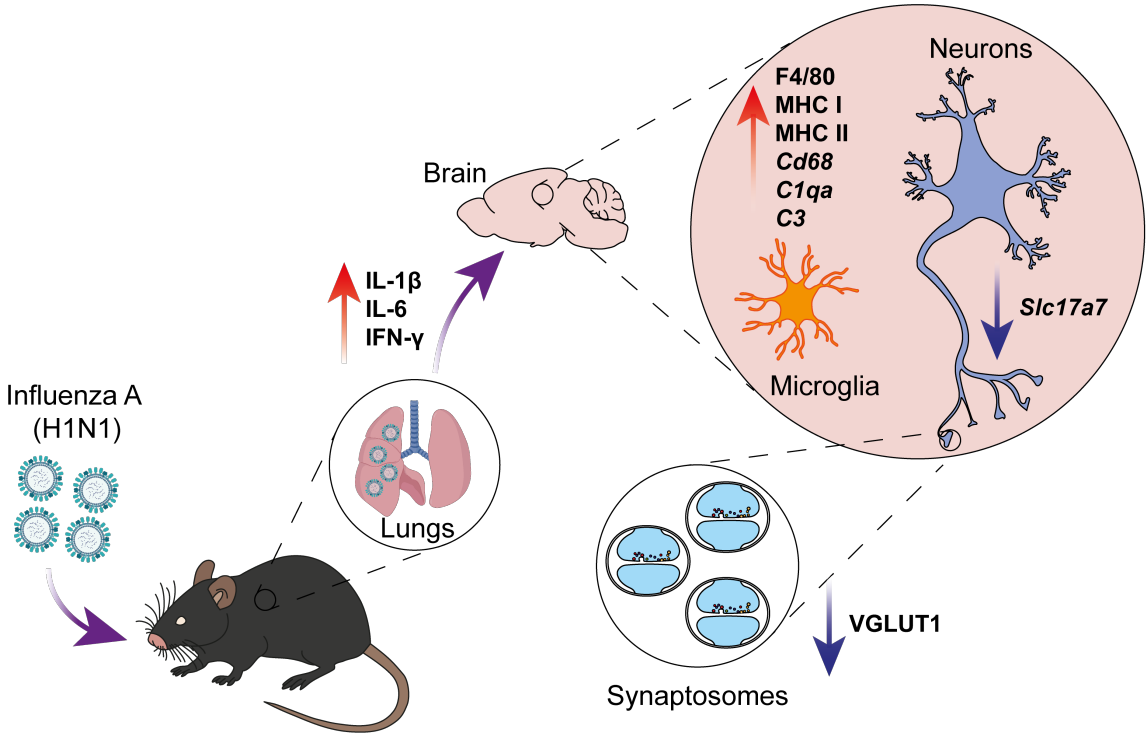

Figure 24: Graphical summary.
In mice, infection with IAV leads to inflammation in the respiratory tract and shortly after to increased serum levels of pro-inflammatory cytokines IL-1β, IL-6, and IFN-γ. The systemic inflammation is accompanied by a temporally disturbed gene expression of BBB-associated proteins. In the CNS, microglial cells upregulate the cell surface markers F4/80, MHC I, and MHC II, indicating the activation of the brain-resident macrophages upon IAV infection. In addition, increased gene expression of *Cd68*, *C1qa*, and *C3* suggests dysregulated synaptic pruning while reduced mRNA levels of *Slc17a7* point towards altered synapse properties. Analysis of synaptosomes via flow synaptometry detected a significant reduction of VGLUT1 in the pre-synaptic terminals of excitatory synapses, thereby revealing detrimental effects of IAV infection on glutamatergic synapse transmission.

Furthermore, these data highlight the connection between peripheral inflammation and the immune cell homeostasis of the brain as a result of the body-brain axis, which in turn may influence neuronal integrity. The characterization of synaptosomes via flow synaptometry as a novel approach enabled to gain further insight into the mechanisms involved in the development of neuronal alterations described by previous studies before. In addition, flow synaptometry may be applied to various other research domains in a future perspective, thus offering an additional tool, besides immunofluorescence microscopy and histological examination, to quantitatively assess the synapse integrity.

Still, some questions remain unanswered and should be addressed by future studies. For once, the role of brain endothelial and epithelial cells as transducers of inflammation from the periphery to the brain upon IAV infection is still unclear. Moreover, the contribution of astrocytes needs to be explored with greater detail with respect to their time and extent of activation. As it appears plausible that astrocytes may become activated during the initial phase of IAV infection, earlier time points have to be considered. In addition, more knowledge is needed to understand the effects of re-infections, even with multiple pathogens acquired over a lifetime, on the homeostasis of microglial cells and their epigenetic changes. Although no pathological short-term effects were noticeable, long-term effects could include a more responsive microglial phenotype and thus need to be elaborated with focus on neuronal alterations. Finally, gaining more insight into the underlying mechanisms of the body-brain axis will provide further understanding of the development of certain neuropsychiatric diseases and neurodegenerative disorders.

6. LIST OF ABBREVIATIONS

%	Percent
°C	Degree Celsius
µl	Microliter
µm	Micrometer
AD	Alzheimer's disease
ALS	Amyotrophic lateral sclerosis
AMPA	α-amino-3-hydroxy-5-methyl-4-isoxazolepropionic acid
ANOVA	Analysis of variance
ASD	Autism spectrum disorder
ATP	Adenosine triphosphate
BAL	Bronchoalveolar lavage
BAM(s)	Border-associated macrophage(s)
BBB	Blood-brain barrier
BCSFB	Blood-cerebrospinal fluid barrier
BDNF	Brain-derived neurotropic factor
BL	Blue laser detection channel
BLAST	Basic Local Alignment Search Tool
bpm	Beats per minute
BSA	Bovine serum albumin
CCL2	C-C motif ligand 2
CD	Cluster of differentiation
CNS	Central nervous system
CP	Choroid Plexus
CR3	Complement receptor 3
CSF	Cerebrospinal fluid
CTX	Cortex
CVO(s)	Circumventricular organ(s)
CX_3CL1	C-X_3-C motif ligand 1

CX_3CR1	C-X_3-C motif receptor 1
CXCL	C-X-C motif ligand
CXCR	C-X-C motif receptor
DAPI	4′,6-Diamidino-2-phenylindole
DNA	Deoxyribonucleic acid
DPBS	Dulbecco's phosphate-buffered saline
dpi	Days post-infection
e.g.	*Exempli gratia* ("for example")
EAAT	Excitatory amino acid carrier
EDTA	Ethylenediaminetetraacetic acid
EM	Electron microscopy
Etc.	*Et cetera*
FACS	Fluorescence-activated cell sorting
FBS	Fetal bovine serum
FMO	Fluorescence-Minus-One
FoxP3	Forkhead-Box-Protein P3
FSC	Forward-scatter light
FSC-A	Area of voltage pulse of FSC photomultiplier tube
FSC-H	Height of voltage pulse of FSC photomultiplier tube
FSM	Flow synaptometry
Fw	Forward
g	Gravity acceleration
GABA	Gamma-aminobutyric acid
GluR1	Glutamate Receptor 1
GM-CSF	Granulocyte-macrophage colony-stimulating factor
GPCR(s)	G-protein-coupled receptor(s)
GTP	Guanosine triphosphate
GTPase(s)	GTP hydrolase enzyme(s)
h	Hour(s)
HA	Haemagglutinin
HBSS	Hank's balanced salt solution
HEPES	4-(2-Hydroxyethyl)piperazine-1-ethane-sulfonic acid
HPF	Hippocampal formation

HRP	Horseradish peroxidase
i.e.	*Id est*, (“that is”)
IAV	Influenza A virus
IBA1	Ionized calcium binding adapter molecule 1
ICAM-1	Intercellular adhesion molecule-1
IDO	Indoleamine 2,3-dioxygenase
IF	Immunofluorescence
IFN(s)	Interferon(s)
IgG	Immunoglobulin G
IGTP	IFN-γ-inducible GTP-binding protein
IL	Interleukin
IRF(s)	Interferon regulatory factor(s)
IRGM1	Immunity-related GTPase family M protein 1
ISG(s)	Interferon-stimulated gene(s)
kDa	Kilodalton
LFA-1	Lymphocyte function-associated antigen-1
LGIC(s)	Ligand-gated ion channel(s)
LPS	Lipopolysaccharides
LRP1	Low density lipoprotein receptor-related protein 1
LTP	Long-term potentiation
M	Molarity in mol/liter
MAP2	Microtubule associated protein 2
MAVS	Mitochondrial antiviral-signaling protein
mBDNF	Mature brain-derived neurotrophic factor
MFI	Median fluorescence intensity
mg	Milligram
MHC	Major histocompatibility complex
min	Minute(s)
ml	Milliliter
mNGF	Mature nerve growth factor
mRNA	Messenger RNA
MS	Multiple sclerosis
NA	Neuraminidase

NeuN	Neuronal nuclei protein
NF-κB	Nuclear factor-κB
ng	Nanogram
NGF	Nerve growth factor
NGS	Normal goat serum
NIR	Near-infrared
NLRP3	NOD-, LRR- and pyrin domain-containing protein 3
nm	Nanometer
NMDA	N-methyl-D-aspartic acid
NOD	Nucleotide-binding oligomerization domain
NOS	Nitrogen species
NP	Nucleoprotein
NS1	Non-structural protein 1
NT	Neurotrophin
$p75^{NTR}$	p75 neurotrophin receptor
PAGE	Polyacrylamide gel electrophoresis
PBS	Phosphate-buffered saline
PD	Parkinson's disease
PER	Peroxidase
PFA	Paraformaldehyde
Poly(I:C)	Polyinosinic:polycytidylic acid
PRR(s)	Pattern recognition receptor(s)
PSD-95	Post-synaptic density protein 95
RIG-I	Retinoic acid inducible gene I
RIPA	Radio-immunoprecipitation assay
RL	Red laser detection channel
RNA	Ribonucleic acid
ROS	Reactive oxygen species
rpm	Revolutions per minute
RSAD2	Radical S-adenosyl methionine domain-containing protein 2
RT-qPCR	Semi-quantitative reverse transcription polymerase chain reaction
Rv	Reverse
SDS	Sodium dodecyl sulphate

SET	Sucrose-EDTA-Tris
SHANK2	Sarcoma homology 3 and multiple ankyrin repeat domains protein 2
SSC	Side-scatter light
Syp	Synaptophysin
TBS	Tris-buffered saline
TBST	Tris-buffered saline with Tween 20
$TCID_{50}$	Median tissue culture infection dose
TLR(s)	Toll-like receptor(s)
TMEM119	Transmembrane protein 119
TNF	Tumor necrosis factor
TREM(s)	Triggering receptor expressed on myeloid cells
TrkB	Tropomyosin-receptor kinase B
t-SNE	*t*-distributed stochastic neighbor embedding
V	Volt
VCAM-1	Vascular cell adhesion molecule-1
VGAT	Vesicular GABA transporter
VGLUT1	Vesicular glutamate transporter 1
VL	Violet laser detection channel
VLA-4	Very late antigen-4
YL	Yellow-green laser detection channel
ZO-1	Zonula occludens-1

All units are represented in SI units.

7. LIST OF FIGURES

8. LIST OF TABLES

9. BIBLIOGRAPHY

1. Thau L, Reddy V, Singh P (2022) StatPearls: Anatomy, Central Nervous System

2. Hofman MA (2014) Evolution of the human brain: when bigger is better. Front Neuroanat 8:15. https://doi.org/10.3389/fnana.2014.00015

3. Kandel ER (ed) (2013) Principles of neural science, 5. ed. McGraw-Hill medical. McGraw-Hill Medical, New York, London

4. Alves de Lima K, Rustenhoven J, Kipnis J (2020) Meningeal Immunity and Its Function in Maintenance of the Central Nervous System in Health and Disease. Annu Rev Immunol 38:597–620. https://doi.org/10.1146/annurev-immunol-102319-103410

5. Aurboonyawat T, Suthipongchai S, Pereira V, Ozanne A, Lasjaunias P (2007) Patterns of cranial venous system from the comparative anatomy in vertebrates. Part I, introduction and the dorsal venous system. Interv Neuroradiol 13:335–344. https://doi.org/10.1177/159101990701300404

6. Ransohoff RM, Engelhardt B (2012) The anatomical and cellular basis of immune surveillance in the central nervous system. Nat Rev Immunol 12:623–635. https://doi.org/10.1038/nri3265

7. Rua R, McGavern DB (2018) Advances in Meningeal Immunity. Trends Mol Med 24:542–559. https://doi.org/10.1016/j.molmed.2018.04.003

8. Louveau A, Smirnov I, Keyes TJ, Eccles JD, Rouhani SJ, Peske JD, Derecki NC, Castle D, Mandell JW, Lee KS, Harris TH, Kipnis J (2015) Structural and functional features of central nervous system lymphatic vessels. Nature 523:337–341. https://doi.org/10.1038/nature14432

9. Absinta M, Ha S-K, Nair G, Sati P, Luciano NJ, Palisoc M, Louveau A, Zaghloul KA, Pittaluga S, Kipnis J, Reich DS (2017) Human and nonhuman primate meninges harbor lymphatic vessels that can be visualized noninvasively by MRI. Elife 6. https://doi.org/10.7554/eLife.29738

10. Balin BJ, Broadwell RD, Salcman M, el-Kalliny M (1986) Avenues for entry of peripherally administered protein to the central nervous system in mouse, rat, and squirrel monkey. J Comp Neurol 251:260–280. https://doi.org/10.1002/cne.902510209

11. Furuse M (2010) Molecular basis of the core structure of tight junctions. Cold Spring Harb Perspect Biol 2:a002907. https://doi.org/10.1101/cshperspect.a002907

12. Derk J, Jones HE, Como C, Pawlikowski B, Siegenthaler JA (2021) Living on the Edge of the CNS: Meninges Cell Diversity in Health and

Disease. Front Cell Neurosci 15:703944. https://doi.org/10.3389/fncel.2021.703944

13. Ghannam JY, Al Kharazi KA (2021) StatPearls: Neuroanatomy, Cranial Meninges, Treasure Island (FL)

14. Lun MP, Monuki ES, Lehtinen MK (2015) Development and functions of the choroid plexus-cerebrospinal fluid system. Nat Rev Neurosci 16:445–457. https://doi.org/10.1038/nrn3921

15. Ross EC, Olivera GC, Barragan A (2022) Early passage of Toxoplasma gondii across the blood-brain barrier. Trends Parasitol 38:450–461. https://doi.org/10.1016/j.pt.2022.02.003

16. Daneman R, Prat A (2015) The blood-brain barrier. Cold Spring Harb Perspect Biol 7:a020412. https://doi.org/10.1101/cshperspect.a020412

17. Allen NJ, Lyons DA (2018) Glia as architects of central nervous system formation and function. Science 362:181–185. https://doi.org/10.1126/science.aat0473

18. Sweeney MD, Zhao Z, Montagne A, Nelson AR, Zlokovic BV (2019) Blood-Brain Barrier: From Physiology to Disease and Back. Physiol Rev 99:21–78. https://doi.org/10.1152/physrev.00050.2017

19. Iadecola C (2017) The Neurovascular Unit Coming of Age: A Journey through Neurovascular Coupling in Health and Disease. Neuron 96:17–42. https://doi.org/10.1016/j.neuron.2017.07.030

20. Zhao Z, Nelson AR, Betsholtz C, Zlokovic BV (2015) Establishment and Dysfunction of the Blood-Brain Barrier. Cell 163:1064–1078. https://doi.org/10.1016/j.cell.2015.10.067

21. Siegenthaler JA, Sohet F, Daneman R (2013) 'Sealing off the CNS': cellular and molecular regulation of blood-brain barriergenesis. Curr Opin Neurobiol 23:1057–1064. https://doi.org/10.1016/j.conb.2013.06.006

22. Tietz S, Engelhardt B (2015) Brain barriers: Crosstalk between complex tight junctions and adherens junctions. J Cell Biol 209:493–506. https://doi.org/10.1083/jcb.201412147

23. Armulik A, Genové G, Mäe M, Nisancioglu MH, Wallgard E, Niaudet C, He L, Norlin J, Lindblom P, Strittmatter K, Johansson BR, Betsholtz C (2010) Pericytes regulate the blood-brain barrier. Nature 468:557–561. https://doi.org/10.1038/nature09522

24. Liebner S, Dijkhuizen RM, Reiss Y, Plate KH, Agalliu D, Constantin G (2018) Functional morphology of the blood-brain barrier in health and disease. Acta Neuropathologica 135:311–336. https://doi.org/10.1007/s00401-018-1815-1

25. Alvarez JI, Dodelet-Devillers A, Kebir H, Ifergan I, Fabre PJ, Terouz S, Sabbagh M, Wosik K, Bourbonnière L, Bernard M, van Horssen J, Vries HE de, Charron F, Prat A (2011) The Hedgehog pathway promotes blood-brain barrier integrity and CNS immune quiescence. Science 334:1727–1731. https://doi.org/10.1126/science.1206936

26. Muoio V, Persson PB, Sendeski MM (2014) The neurovascular unit - concept review. Acta Physiol (Oxf) 210:790–798. https://doi.org/10.1111/apha.12250

27. Keaney J, Campbell M (2015) The dynamic blood-brain barrier. FEBS J 282:4067–4079. https://doi.org/10.1111/febs.13412

28. Gralinski LE, Ashley SL, Dixon SD, Spindler KR (2009) Mouse adenovirus type 1-induced breakdown of the blood-brain barrier. Journal of Virology 83:9398–9410. https://doi.org/10.1128/JVI.00954-09

29. Verma S, Kumar M, Gurjav U, Lum S, Nerurkar VR (2010) Reversal of West Nile virus-induced blood-brain barrier disruption and tight junction proteins degradation by matrix metalloproteinases inhibitor. Virology 397:130–138. https://doi.org/10.1016/j.virol.2009.10.036

30. Afonso PV, Ozden S, Cumont M-C, Seilhean D, Cartier L, Rezaie P, Mason S, Lambert S, Huerre M, Gessain A, Couraud P-O, Pique C, Ceccaldi P-E, Romero IA (2008) Alteration of blood-brain barrier integrity by retroviral infection. PLoS Pathog 4:e1000205. https://doi.org/10.1371/journal.ppat.1000205

31. Praetorius J, Damkier HH (2017) Transport across the choroid plexus epithelium. Am J Physiol Cell Physiol 312:C673-C686. https://doi.org/10.1152/ajpcell.00041.2017

32. Kaiser K, Bryja V (2020) Choroid Plexus: The Orchestrator of Long-Range Signalling Within the CNS. Int J Mol Sci 21. https://doi.org/10.3390/ijms21134760

33. Solár P, Zamani A, Kubíčková L, Dubový P, Joukal M (2020) Choroid plexus and the blood-cerebrospinal fluid barrier in disease. Fluids Barriers CNS 17:35. https://doi.org/10.1186/s12987-020-00196-2

34. Liddelow SA (2015) Development of the choroid plexus and blood-CSF barrier. Front Neurosci 9:32. https://doi.org/10.3389/fnins.2015.00032

35. Pakkenberg B, Gundersen HJ (1997) Neocortical neuron number in humans: effect of sex and age. J Comp Neurol 384:312–320

36. Stiles J, Jernigan TL (2010) The basics of brain development. Neuropsychol Rev 20:327–348. https://doi.org/10.1007/s11065-010-9148-4

37. Brown M, Keynes R, Lumsden A (2004) The developing brain, 1. publ., repr. Oxford Univ. Press, Oxford

38. Lovinger DM (2008) Communication networks in the brain: neurons, receptors, neurotransmitters, and alcohol. Alcohol Res Health 31:196–214

39. Missler M, Südhof TC, Biederer T (2012) Synaptic cell adhesion. Cold Spring Harb Perspect Biol 4:a005694. https://doi.org/10.1101/cshperspect.a005694

40. Südhof TC (2021) The cell biology of synapse formation. J Cell Biol 220. https://doi.org/10.1083/jcb.202103052

41. Laßek M, Weingarten J, Volknandt W (2015) The synaptic proteome. Cell Tissue Res 359:255–265. https://doi.org/10.1007/s00441-014-1943-4

42. Gundelfinger ED, Reissner C, Garner CC (2015) Role of Bassoon and Piccolo in Assembly and Molecular Organization of the Active Zone. Front Synaptic Neurosci 7:19. https://doi.org/10.3389/fnsyn.2015.00019

43. Monteiro P, Feng G (2017) SHANK proteins: roles at the synapse and in autism spectrum disorder. Nat Rev Neurosci 18:147–157. https://doi.org/10.1038/nrn.2016.183

44. Choii G, Ko J (2015) Gephyrin: a central GABAergic synapse organizer. Exp Mol Med 47:e158. https://doi.org/10.1038/emm.2015.5

45. Berke JD (2018) What does dopamine mean? Nat Neurosci 21:787–793. https://doi.org/10.1038/s41593-018-0152-y

46. Klein MO, Battagello DS, Cardoso AR, Hauser DN, Bittencourt JC, Correa RG (2019) Dopamine: Functions, Signaling, and Association with Neurological Diseases. Cell Mol Neurobiol 39:31–59. https://doi.org/10.1007/s10571-018-0632-3

47. Berger M, Gray JA, Roth BL (2009) The expanded biology of serotonin. Annu Rev Med 60:355–366. https://doi.org/10.1146/annurev.med.60.042307.110802

48. Iovino L, Tremblay ME, Civiero L (2020) Glutamate-induced excitotoxicity in Parkinson's disease: The role of glial cells. J Pharmacol Sci 144:151–164. https://doi.org/10.1016/j.jphs.2020.07.011

49. Huang Y, Thathiah A (2015) Regulation of neuronal communication by G protein-coupled receptors. FEBS Lett 589:1607–1619. https://doi.org/10.1016/j.febslet.2015.05.007

50. Ibáñez CF, Simi A (2012) p75 neurotrophin receptor signaling in nervous system injury and degeneration: Paradox and opportunity. Trends Neurosci 35:431–440. https://doi.org/10.1016/j.tins.2012.03.007

51. Mitre M, Mariga A, Chao MV (2017) Neurotrophin signalling: Novel insights into mechanisms and pathophysiology. Clin Sci 131:13–23. https://doi.org/10.1042/CS20160044

52. Gibon J, Barker PA (2017) Neurotrophins and Proneurotrophins. Neuroscientist:1073858417697037. https://doi.org/10.1177/1073858417697037

53. Wise BL, Seidel MF, Lane NE (2021) The evolution of nerve growth factor inhibition in clinical medicine. Nat Rev Rheumatol 17:34–46. https://doi.org/10.1038/s41584-020-00528-4

54. Chao MV (2003) Neurotrophins and their receptors: a convergence point for many signalling pathways. Nat Rev Neurosci 4:299–309. https://doi.org/10.1038/nrn1078

55. Nykjaer A, Willnow TE, Petersen CM (2005) p75NTR--live or let die. Curr Opin Neurobiol 15:49–57. https://doi.org/10.1016/j.conb.2005.01.004

56. Gibon J, Buckley SM, Unsain N, Kaartinen V, Séguéla P, Barker PA (2015) proBDNF and p75NTR Control Excitability and Persistent Firing of Cortical Pyramidal Neurons. J Neurosci 35:9741–9753. https://doi.org/10.1523/JNEUROSCI.4655-14.2015

57. Qiao H, An S-C, Xu C, Ma X-M (2017) Role of proBDNF and BDNF in dendritic spine plasticity and depressive-like behaviors induced by an animal model of depression. Brain Research 1663:29–37. https://doi.org/10.1016/j.brainres.2017.02.020

58. Xue Y, Liang H, Yang R, Deng K, Tang M, Zhang M (2021) The role of pro- and mature neurotrophins in the depression. Behavioural Brain Research 404:113162. https://doi.org/10.1016/j.bbr.2021.113162

59. Bartheld CS von, Bahney J, Herculano-Houzel S (2016) The search for true numbers of neurons and glial cells in the human brain: A review of 150 years of cell counting. J Comp Neurol 524:3865–3895. https://doi.org/10.1002/cne.24040

60. Baumann N, Pham-Dinh D (2001) Biology of oligodendrocyte and myelin in the mammalian central nervous system. Physiol Rev 81:871–927. https://doi.org/10.1152/physrev.2001.81.2.871

61. Elbaz B, Popko B (2019) Molecular Control of Oligodendrocyte Development. Trends Neurosci 42:263–277. https://doi.org/10.1016/j.tins.2019.01.002

62. Tiane A, Schepers M, Rombaut B, Hupperts R, Prickaerts J, Hellings N, van den Hove D, Vanmierlo T (2019) From OPC to Oligodendrocyte: An Epigenetic Journey. Cells 8. https://doi.org/10.3390/cells8101236

63. Stadelmann C, Timmler S, Barrantes-Freer A, Simons M (2019) Myelin in the Central Nervous System: Structure, Function, and Pathology. Physiol Rev 99:1381–1431. https://doi.org/10.1152/physrev.00031.2018

64. McTigue DM, Tripathi RB (2008) The life, death, and replacement of oligodendrocytes in the adult CNS. J Neurochem 107:1–19. https://doi.org/10.1111/j.1471-4159.2008.05570.x

65. Reich DS, Lucchinetti CF, Calabresi PA (2018) Multiple Sclerosis. N Engl J Med 378:169–180. https://doi.org/10.1056/NEJMra1401483

66. Freeman MR (2010) Specification and morphogenesis of astrocytes. Science 330:774–778. https://doi.org/10.1126/science.1190928

67. Molofsky AV, Deneen B (2015) Astrocyte development: A Guide for the Perplexed. Glia 63:1320–1329. https://doi.org/10.1002/glia.22836

68. Allen NJ, Eroglu C (2017) Cell Biology of Astrocyte-Synapse Interactions. Neuron 96:697–708. https://doi.org/10.1016/j.neuron.2017.09.056

69. Neniskyte U, Gross CT (2017) Errant gardeners: glial-cell-dependent synaptic pruning and neurodevelopmental disorders. Nat Rev Neurosci 18:658–670. https://doi.org/10.1038/nrn.2017.110

70. Sancho L, Contreras M, Allen NJ (2021) Glia as sculptors of synaptic plasticity. Neurosci Res 167:17–29. https://doi.org/10.1016/j.neures.2020.11.005

71. Mayorga-Weber G, Rivera FJ, Castro MA (2022) Neuron-glia (mis)interactions in brain energy metabolism during aging. J Neurosci Res 100:835–854. https://doi.org/10.1002/jnr.25015

72. Bak LK, Schousboe A, Waagepetersen HS (2006) The glutamate/GABA-glutamine cycle: aspects of transport, neurotransmitter homeostasis and ammonia transfer. J Neurochem 98:641–653. https://doi.org/10.1111/j.1471-4159.2006.03913.x

73. Khakh BS, McCarthy KD (2015) Astrocyte calcium signaling: from observations to functions and the challenges therein. Cold Spring Harb Perspect Biol 7:a020404. https://doi.org/10.1101/cshperspect.a020404

74. Acosta C, Anderson HD, Anderson CM (2017) Astrocyte dysfunction in Alzheimer disease. J Neurosci Res 95:2430–2447. https://doi.org/10.1002/jnr.24075

75. Singh A, Abraham WC (2017) Astrocytes and synaptic plasticity in health and disease. Exp Brain Res 235:1645–1655. https://doi.org/10.1007/s00221-017-4928-1

76. Pekna M, Pekny M (2021) The Complement System: A Powerful Modulator and Effector of Astrocyte Function in the Healthy and Diseased Central Nervous System. Cells 10. https://doi.org/10.3390/cells10071812

77. Croese T, Castellani G, Schwartz M (2021) Immune cell compartmentalization for brain surveillance and protection. Nat Immunol 22:1083–1092. https://doi.org/10.1038/s41590-021-00994-2

78. Ginhoux F, Lim S, Hoeffel G, Low D, Huber T (2013) Origin and differentiation of microglia. Front Cell Neurosci 7:45. https://doi.org/10.3389/fncel.2013.00045

79. Prinz M, Jung S, Priller J (2019) Microglia Biology: One Century of Evolving Concepts. Cell 179:292–311. https://doi.org/10.1016/j.cell.2019.08.053

80. Li Q, Barres BA (2018) Microglia and macrophages in brain homeostasis and disease. Nat Rev Immunol 18:225–242. https://doi.org/10.1038/nri.2017.125

81. Frost JL, Schafer DP (2016) Microglia: Architects of the Developing Nervous System. Trends Cell Biol 26:587–597. https://doi.org/10.1016/j.tcb.2016.02.006

82. Sierra A, Encinas JM, Deudero JJP, Chancey JH, Enikolopov G, Overstreet-Wadiche LS, Tsirka SE, Maletic-Savatic M (2010) Microglia shape adult hippocampal neurogenesis through apoptosis-coupled phagocytosis. Cell Stem Cell 7:483–495. https://doi.org/10.1016/j.stem.2010.08.014

83. Nimmerjahn A, Kirchhoff F, Helmchen F (2005) Resting microglial cells are highly dynamic surveillants of brain parenchyma in vivo. Science 308:1314–1318. https://doi.org/10.1126/science.1110647

84. Kettenmann H, Kirchhoff F, Verkhratsky A (2013) Microglia: new roles for the synaptic stripper. Neuron 77:10–18. https://doi.org/10.1016/j.neuron.2012.12.023

85. Li Y, Du X-F, Liu C-S, Wen Z-L, Du J-L (2012) Reciprocal regulation between resting microglial dynamics and neuronal activity in vivo. Dev Cell 23:1189–1202.

https://doi.org/10.1016/j.devcel.2012.10.027

86. Tremblay M-È, Lowery RL, Majewska AK (2010) Microglial interactions with synapses are modulated by visual experience. PLoS Biol 8:e1000527. https://doi.org/10.1371/journal.pbio.1000527

87. Parkhurst CN, Yang G, Ninan I, Savas JN, Yates JR, Lafaille JJ, Hempstead BL, Littman DR, Gan W-B (2013) Microglia promote learning-dependent synapse formation through brain-derived neurotrophic factor. Cell 155:1596–1609. https://doi.org/10.1016/j.cell.2013.11.030

88. Calovi S, Mut-Arbona P, Sperlágh B (2019) Microglia and the Purinergic Signaling System. Neuroscience 405:137–147. https://doi.org/10.1016/j.neuroscience.2018.12.021

89. Brown GC, Neher JJ (2014) Microglial phagocytosis of live neurons. Nat Rev Neurosci 15:209–216. https://doi.org/10.1038/nrn3710

90. Lehrman EK, Wilton DK, Litvina EY, Welsh CA, Chang ST, Frouin A, Walker AJ, Heller MD, Umemori H, Chen C, Stevens B (2018) CD47 Protects Synapses from Excess Microglia-Mediated Pruning during Development. Neuron 100:120-134.e6. https://doi.org/10.1016/j.neuron.2018.09.017

91. Tang G, Gudsnuk K, Kuo S-H, Cotrina ML, Rosoklija G, Sosunov A, Sonders MS, Kanter E, Castagna C, Yamamoto A, Yue Z, Arancio O, Peterson BS, Champagne F, Dwork AJ, Goldman J, Sulzer D (2014) Loss of mTOR-dependent macroautophagy causes autistic-like synaptic pruning deficits. Neuron 83:1131–1143. https://doi.org/10.1016/j.neuron.2014.07.040

92. Faust TE, Gunner G, Schafer DP (2021) Mechanisms governing activity-dependent synaptic pruning in the developing mammalian CNS. Nat Rev Neurosci 22:657–673. https://doi.org/10.1038/s41583-021-00507-y

93. Rodríguez-Gómez JA, Kavanagh E, Engskog-Vlachos P, Engskog MKR, Herrera AJ, Espinosa-Oliva AM, Joseph B, Hajji N, Venero JL, Burguillos MA (2020) Microglia: Agents of the CNS Pro-Inflammatory Response. Cells 9. https://doi.org/10.3390/cells9071717

94. Wolf SA, Boddeke HWGM, Kettenmann H (2017) Microglia in Physiology and Disease. Annu Rev Physiol 79:619–643. https://doi.org/10.1146/annurev-physiol-022516-034406

95. Heneka MT, Kummer MP, Stutz A, Delekate A, Schwartz S, Vieira-Saecker A, Griep A, Axt D, Remus A, Tzeng T-C, Gelpi E, Halle A, Korte M, Latz E, Golenbock DT (2013) NLRP3 is activated in Alzheimer's disease and contributes to pathology in APP/PS1 mice. Nature 493:674–678. https://doi.org/10.1038/nature11729

96. Gordon R, Albornoz EA, Christie DC, Langley MR, Kumar V, Mantovani S, Robertson AAB, Butler MS, Rowe DB, O'Neill LA, Kanthasamy AG, Schroder K, Cooper MA, Woodruff TM (2018) Inflammasome inhibition prevents α-synuclein pathology and dopaminergic neurodegeneration in mice. Sci Transl Med 10. https://doi.org/10.1126/scitranslmed.aah4066

97. Heneka MT (2019) Microglia take centre stage in neurodegenerative disease. Nat Rev Immunol 19:79–80. https://doi.org/10.1038/s41577-018-0112-5

98. Kipnis J (2016) Multifaceted interactions between adaptive immunity and the central nervous system. Science 353:766–771. https://doi.org/10.1126/science.aag2638

99. Mrdjen D, Pavlovic A, Hartmann FJ, Schreiner B, Utz SG, Leung BP, Lelios I, Heppner FL, Kipnis J, Merkler D, Greter M, Becher B (2018) High-Dimensional Single-Cell Mapping of Central Nervous System Immune Cells Reveals Distinct Myeloid Subsets in Health, Aging, and Disease. Immunity. https://doi.org/10.1016/j.immuni.2018.01.011

100. Mundt S, Greter M, Flügel A, Becher B (2019) The CNS Immune Landscape from the Viewpoint of a T Cell. Trends Neurosci 42:667–679. https://doi.org/10.1016/j.tins.2019.07.008

101. Tanabe S, Yamashita T (2018) B-1a lymphocytes promote oligodendrogenesis during brain development. Nat Neurosci 21:506–516. https://doi.org/10.1038/s41593-018-0106-4

102. Filiano AJ, Xu Y, Tustison NJ, Marsh RL, Baker W, Smirnov I, Overall CC, Gadani SP, Turner SD, Weng Z, Peerzade SN, Chen H, Lee KS, Scott MM, Beenhakker MP, Litvak V, Kipnis J (2016) Unexpected role of interferon-γ in regulating neuronal connectivity and social behaviour. Nature 535:425–429. https://doi.org/10.1038/nature18626

103. Derecki NC, Cardani AN, Yang CH, Quinnies KM, Crihfield A, Lynch KR, Kipnis J (2010) Regulation of learning and memory by meningeal immunity: a key role for IL-4. J Exp Med 207:1067–1080. https://doi.org/10.1084/jem.20091419

104. Marsh SE, Abud EM, Lakatos A, Karimzadeh A, Yeung ST, Davtyan H, Fote GM, Lau L, Weinger JG, Lane TE, Inlay MA, Poon WW, Blurton-Jones M (2016) The adaptive immune system restrains Alzheimer's disease pathogenesis by modulating microglial function. Proc Natl Acad Sci U S A 113:E1316-25. https://doi.org/10.1073/pnas.1525466113

105. Beers DR, Henkel JS, Zhao W, Wang J, Appel SH (2008) CD4+ T cells support glial neuroprotection, slow disease progression, and modify glial morphology in an animal model of inherited ALS. Proc Natl Acad Sci U S A 105:15558–15563. https://doi.org/10.1073/pnas.0807419105

106. Schwartz M, Kipnis J, Rivest S, Prat A (2013) How do immune cells support and shape the brain in health, disease, and aging? J Neurosci 33:17587–17596. https://doi.org/10.1523/JNEUROSCI.3241-13.2013

107. Schwartz M, Baruch K (2014) The resolution of neuroinflammation in neurodegeneration: leukocyte recruitment via the choroid plexus. EMBO J 33:7–22. https://doi.org/10.1002/embj.201386609

108. Russo MV, McGavern DB (2015) Immune Surveillance of the CNS following Infection and Injury. Trends Immunol 36:637–650.

https://doi.org/10.1016/j.it.2015.08.002

109. European Centre for Disease Prevention and Control Factsheet about seasonal influenza. https://www.ecdc.europa.eu/en/seasonal-influenza/facts/factsheet. Accessed 24 Apr 2022

110. Nüssing S, Sant S, Koutsakos M, Subbarao K, Nguyen THO, Kedzierska K (2018) Innate and adaptive T cells in influenza disease. Front Med 12:34–47. https://doi.org/10.1007/s11684-017-0606-8

111. The International Committee on Taxonomy of Viruses Virus Taxonomy: 2021 Release. https://talk.ictvonline.org/taxonomy/. Accessed 24 Apr 2022

112. Krammer F, Smith GJD, Fouchier RAM, Peiris M, Kedzierska K, Doherty PC, Palese P, Shaw ML, Treanor J, Webster RG, García-Sastre A (2018) Influenza. Nat Rev Dis Primers 4:3. https://doi.org/10.1038/s41572-018-0002-y

113. Goerlitz L, Dürrwald R, der Heiden M an, Buchholz U, Preuß U, Prahm K, Buda S Erste Ergebnisse zum Verlauf der Grippewelle in der Saison 2019/20: Mit 11 Wochen vergleichsweise kürzere Dauer und eine moderate Anzahl an Influenza-bedingten Arztbesuchen. In: Robert Koch-Institut (ed) Epidemiologisches Bulletin 16/2020

114. Medina RA, García-Sastre A (2011) Influenza A viruses: New research developments. Nat Rev Micro 9:590–603. https://doi.org/10.1038/nrmicro2613

115. Kim H, Webster RG, Webby RJ (2018) Influenza Virus: Dealing with a Drifting and Shifting Pathogen. Viral Immunol 31:174–183. https://doi.org/10.1089/vim.2017.0141

116. Mifsud EJ, Kuba M, Barr IG (2021) Innate Immune Responses to Influenza Virus Infections in the Upper Respiratory Tract. Viruses 13. https://doi.org/10.3390/v13102090

117. Iwasaki A, Pillai PS (2014) Innate immunity to influenza virus infection. Nat Rev Immunol 14:315–328. https://doi.org/10.1038/nri3665

118. Jansen JM, Gerlach T, Elbahesh H, Rimmelzwaan GF, Saletti G (2019) Influenza virus-specific CD4+ and CD8+ T cell-mediated immunity induced by infection and vaccination. J Clin Virol 119:44–52. https://doi.org/10.1016/j.jcv.2019.08.009

119. Takahashi Y, Onodera T, Adachi Y, Ato M (2017) Adaptive B Cell Responses to Influenza Virus Infection in the Lung. Viral Immunol 30:431–437. https://doi.org/10.1089/vim.2017.0025

120. Stebegg M, Kumar SD, Silva-Cayetano A, Fonseca VR, Linterman MA, Graca L (2018) Regulation of the Germinal Center Response. Front Immunol 9:2469. https://doi.org/10.3389/fimmu.2018.02469

121. Shattuck EC, Muehlenbein MP (2015) Human sickness behavior: Ultimate and proximate explanations. Am J Phys Anthropol 157:1–18. https://doi.org/10.1002/ajpa.22698

122. Krapić M, Kavazović I, Wensveen FM (2021) Immunological Mechanisms of Sickness Behavior in Viral Infection. Viruses 13. https://doi.org/10.3390/v13112245

123. Quan N (2014) In-depth conversation: spectrum and kinetics of neuroimmune afferent pathways. Brain Behav Immun 40:1–8. https://doi.org/10.1016/j.bbi.2014.02.006

124. Harden LM, Kent S, Pittman QJ, Roth J (2015) Fever and sickness behavior: Friend or foe? Brain Behav Immun 50:322–333. https://doi.org/10.1016/j.bbi.2015.07.012

125. Roth J, Harré E-M, Rummel C, Gerstberger R, Hübschle T (2004) Signaling the brain in systemic inflammation: role of sensory circumventricular organs. Front Biosci 9:290–300. https://doi.org/10.2741/1241

126. Poon DC-H, Ho Y-S, Chiu K, Chang RC-C (2013) Cytokines: how important are they in mediating sickness? Neurosci Biobehav Rev 37:1–10. https://doi.org/10.1016/j.neubiorev.2012.11.001

127. Banks WA, Erickson MA (2010) The blood–brain barrier and immune function and dysfunction. Neurobiology of Disease 37:26–32. https://doi.org/10.1016/j.nbd.2009.07.031

128. Dantzer R, O'Connor JC, Freund GG, Johnson RW, Kelley KW (2008) From inflammation to sickness and depression: when the immune system subjugates the brain. Nat Rev Neurosci 9:46–56. https://doi.org/10.1038/nrn2297

129. Bornand D, Toovey S, Jick SS, Meier CR (2016) The risk of new onset depression in association with influenza--A population-based observational study. Brain Behav Immun 53:131–137. https://doi.org/10.1016/j.bbi.2015.12.005

130. Jurgens HA, Amancherla K, Johnson RW (2012) Influenza infection induces neuroinflammation, alters hippocampal neuron morphology, and impairs cognition in adult mice. The Journal of neuroscience: the official journal of the Society for Neuroscience 32:3958–3968. https://doi.org/10.1523/JNEUROSCI.6389-11.2012

131. Hosseini S, Wilk E, Michaelsen-Preusse K, Gerhauser I, Baumgärtner W, Geffers R, Schughart K, Korte M (2018) Long-Term Neuroinflammation Induced by Influenza A Virus Infection and the Impact on Hippocampal Neuron Morphology and Function. J Neurosci 38:3060–3080. https://doi.org/10.1523/JNEUROSCI.1740-17.2018

132. Stegemann S, Dahlberg S, Kröger A, Gereke M, Bruder D, Henriques-Normark B, Gunzer M (2009) Increased susceptibility for superinfection with Streptococcus pneumoniae during influenza virus infection is not caused by TLR7-mediated lymphopenia. PLoS ONE 4:e4840. https://doi.org/10.1371/journal.pone.0004840

133. Sharma-Chawla N, Sender V, Kershaw O, Gruber AD, Volckmar J, Henriques-Normark B, Stegemann-Koniszewski S, Bruder D (2016) Influenza A Virus Infection Predisposes Hosts to Secondary Infection with Different Streptococcus pneumoniae Serotypes with Similar Outcome but Serotype-Specific Manifestation. Infect Immun 84:3445–3457. https://doi.org/10.1128/IAI.00422-16

134. Lein ES, Hawrylycz MJ, Ao N, Ayres M, Bensinger A, Bernard A, Boe AF, Boguski MS, Brockway KS, Byrnes

EJ, Chen L, Chen L, Chen T-M, Chin MC, Chong J, Crook BE, Czaplinska A, Dang CN, Datta S, Dee NR, Desaki AL, Desta T, Diep E, Dolbeare TA, Donelan MJ, Dong H-W, Dougherty JG, Duncan BJ, Ebbert AJ, Eichele G, Estin LK, Faber C, Facer BA, Fields R, Fischer SR, Fliss TP, Frensley C, Gates SN, Glattfelder KJ, Halverson KR, Hart MR, Hohmann JG, Howell MP, Jeung DP, Johnson RA, Karr PT, Kawal R, Kidney JM, Knapik RH, Kuan CL, Lake JH, Laramee AR, Larsen KD, Lau C, Lemon TA, Liang AJ, Liu Y, Luong LT, Michaels J, Morgan JJ, Morgan RJ, Mortrud MT, Mosqueda NF, Ng LL, Ng R, Orta GJ, Overly CC, Pak TH, Parry SE, Pathak SD, Pearson OC, Puchalski RB, Riley ZL, Rockett HR, Rowland SA, Royall JJ, Ruiz MJ, Sarno NR, Schaffnit K, Shapovalova NV, Sivisay T, Slaughterbeck CR, Smith SC, Smith KA, Smith BI, Sodt AJ, Stewart NN, Stumpf K-R, Sunkin SM, Sutram M, Tam A, Teemer CD, Thaller C, Thompson CL, Varnam LR, Visel A, Whitlock RM, Wohnoutka PE, Wolkey CK, Wong VY, Wood M, Yaylaoglu MB, Young RC, Youngstrom BL, Yuan XF, Zhang B, Zwingman TA, Jones AR (2007) Genome-wide atlas of gene expression in the adult mouse brain. Nature 445:168–176. https://doi.org/10.1038/nature05453

135. Ye J, Coulouris G, Zaretskaya I, Cutcutache I, Rozen S, Madden TL (2012) Primer-BLAST: a tool to design target-specific primers for polymerase chain reaction. BMC Bioinformatics 13:134. https://doi.org/10.1186/1471-2105-13-134

136. Schindelin J, Arganda-Carreras I, Frise E, Kaynig V, Longair M, Pietzsch T, Preibisch S, Rueden C, Saalfeld S, Schmid B, Tinevez J-Y, White DJ, Hartenstein V, Eliceiri K, Tomancak P, Cardona A (2012) Fiji: An open-source platform for biological-image analysis. Nat Methods 9:676–682. https://doi.org/10.1038/nmeth.2019

137. Smalla K-H, Klemmer P, Wyneken U (2013) Isolation of the Postsynaptic Density: A Specialization of the Subsynaptic Cytoskeleton. In: Dermietzel R (ed) The cytoskeleton: Imaging, isolation, and interaction, vol 79. Humana Press, New York, pp 265–280

138. Hobson BD, Sims PA (2019) Critical Analysis of Particle Detection Artifacts in Synaptosome Flow Cytometry. eNeuro 6. https://doi.org/10.1523/ENEURO.0009-19.2019

139. Breukel AI, Besselsen E, Ghijsen WE (1997) Synaptosomes. A model system to study release of multiple classes of neurotransmitters. Methods Mol Biol 72:33–47. https://doi.org/10.1385/0-89603-394-5:33

140. R Core Team (2020) R: A language and environment for statistical computing. R Foundation for Statistical Computing, Vienna, Austria

141. Sarkar D (2008) Lattice: Multivariate Data Visualization with R. Springer New York, New York, NY

142. Düsedau HP, Steffen J, Figueiredo CA, Boehme JD, Schultz K, Erck C, Korte M, Faber-Zuschratter H, Smalla K-H, Dieterich D, Kröger A, Bruder D, Dunay IR (2021) Influenza A Virus (H1N1) Infection Induces Microglial Activation and Temporal Dysbalance in Glutamatergic Synaptic Transmission. mBio 12:e0177621. https://doi.org/10.1128/mBio.01776-21

143. Layé S, Parnet P, Goujon E, Dantzer R (1994) Peripheral administration of lipopolysaccharide induces the expression of cytokine transcripts in the brain and pituitary of mice. Molecular Brain Research 27:157–162. https://doi.org/10.1016/0169-328X(94)90197-X

144. Dantzer R (2001) Cytokine-induced sickness behavior: mechanisms and implications. Annals of the New York Academy of Sciences 933:222–234. https://doi.org/10.1111/j.1749-6632.2001.tb05827.x

145. Blank T, Detje CN, Spieß A, Hagemeyer N, Brendecke SM, Wolfart J, Staszewski O, Zöller T, Papageorgiou I, Schneider J, Paricio-Montesinos R, Eisel ULM, Manahan-Vaughan D, Jansen S, Lienenklaus S, Lu B, Imai Y, Müller M, Goelz SE, Baker DP, Schwaninger M, Kann O, Heikenwalder M, Kalinke U, Prinz M (2016) Brain Endothelial- and Epithelial-Specific Interferon Receptor Chain 1 Drives Virus-Induced Sickness Behavior and Cognitive Impairment. Immunity 44:901–912. https://doi.org/10.1016/j.immuni.2016.04.005

146. Nitta T, Hata M, Gotoh S, Seo Y, Sasaki H, Hashimoto N, Furuse M, Tsukita S (2003) Size-selective loosening of the blood-brain barrier in claudin-5-deficient mice. J Cell Biol 161:653–660. https://doi.org/10.1083/jcb.200302070

147. Zlokovic BV (2008) The blood-brain barrier in health and chronic neurodegenerative disorders. Neuron 57:178–201. https://doi.org/10.1016/j.neuron.2008.01.003

148. Zlokovic BV (2011) Neurovascular pathways to neurodegeneration in Alzheimer's disease and other disorders. Nat Rev Neurosci 12:723–738. https://doi.org/10.1038/nrn3114

149. Daniels BP, Holman DW, Cruz-Orengo L, Jujjavarapu H, Durrant DM, Klein RS (2014) Viral pathogen-associated molecular patterns regulate blood-brain barrier integrity via competing innate cytokine signals. mBio 5:e01476-14. https://doi.org/10.1128/mBio.01476-14

150. Kraus J, Oschmann P (2006) The impact of interferon-beta treatment on the blood-brain barrier. Drug Discov Today 11:755–762. https://doi.org/10.1016/j.drudis.2006.06.008

151. Ni C, Wang C, Zhang J, Qu L, Liu X, Lu Y, Yang W, Deng J, Lorenz D, Gao P, Meng Q, Yan X, Blasig IE, Qin Z (2014) Interferon-γ safeguards blood-brain barrier during experimental autoimmune encephalomyelitis. The American Journal of Pathology 184:3308–3320. https://doi.org/10.1016/j.ajpath.2014.08.019

152. Dyrna F, Hanske S, Krueger M, Bechmann I (2013) The blood-brain barrier. J Neuroimmune Pharmacol 8:763–773. https://doi.org/10.1007/s11481-013-9473-5

153. Klein RS, Lin E, Zhang B, Luster AD, Tollett J, Samuel MA, Engle M, Diamond MS (2005) Neuronal CXCL10 directs CD8+ T-cell recruitment and control of West Nile virus encephalitis. Journal of Virology 79:11457–11466. https://doi.org/10.1128/JVI.79.17.11457-11466.2005

154. Zhang B, Chan YK, Lu B, Diamond MS, Klein RS (2008) CXCR3 mediates region-specific antiviral T cell trafficking within the central nervous system during West Nile virus encephalitis. J Immunol 180:2641–2649. https://doi.org/10.4049/jimmunol.180.4.2641

155. Caceres A, Banker G, Steward O, Binder L, Payne M (1984) MAP2 is localized to the dendrites of hippocampal neurons which develop in culture. Developmental Brain Research 13:314–318. https://doi.org/10.1016/0165-3806(84)90167-6

156. Matesic DF, Lin RC (1994) Microtubule-associated protein 2 as an early indicator of ischemia-induced neurodegeneration in the gerbil forebrain. J Neurochem 63:1012–1020. https://doi.org/10.1046/j.1471-4159.1994.63031012.x

157. Dawson DA, Hallenbeck JM (1996) Acute focal ischemia-induced alterations in MAP2 immunostaining: description of temporal changes and utilization as a marker for volumetric assessment of acute brain injury. J Cereb Blood Flow Metab 16:170–174. https://doi.org/10.1097/00004647-199601000-00020

158. Kim KK, Adelstein RS, Kawamoto S (2009) Identification of neuronal nuclei (NeuN) as Fox-3, a new member of the Fox-1 gene family of splicing factors. J Biol Chem 284:31052–31061. https://doi.org/10.1074/jbc.M109.052969

159. Wolf HK, Buslei R, Schmidt-Kastner R, Schmidt-Kastner PK, Pietsch T, Wiestler OD, Blümcke I (1996) NeuN: a useful neuronal marker for diagnostic histopathology. J Histochem Cytochem 44:1167–1171. https://doi.org/10.1177/44.10.8813082

160. Streit WJ, Walter SA, Pennell NA (1999) Reactive microgliosis. Progress in Neurobiology 57:563–581. https://doi.org/10.1016/S0301-0082(98)00069-0

161. Schafer DP, Stevens B (2015) Microglia Function in Central Nervous System Development and Plasticity. Cold Spring Harb Perspect Biol 7:a020545. https://doi.org/10.1101/cshperspect.a020545

162. Manjally AV, Tay TL (2022) Attack of the Clones: Microglia in Health and Disease. Front Cell Neurosci 16:831747. https://doi.org/10.3389/fncel.2022.831747

163. Ito D, Imai Y, Ohsawa K, Nakajima K, Fukuuchi Y, Kohsaka S (1998) Microglia-specific localisation of a novel calcium binding protein, Iba1. Molecular Brain Research 57:1–9. https://doi.org/10.1016/S0169-328X(98)00040-0

164. Bennett ML, Bennett FC, Liddelow SA, Ajami B, Zamanian JL, Fernhoff NB, Mulinyawe SB, Bohlen CJ, Adil A, Tucker A, Weissman IL, Chang EF, Li G, Grant GA, Hayden Gephart MG, Barres BA (2016) New tools for studying microglia in the mouse and human CNS. Proc Natl Acad Sci U S A 113:E1738-46. https://doi.org/10.1073/pnas.1525528113

165. Ransohoff RM (2016) A polarizing question: do M1 and M2 microglia exist? Nat Neurosci 19:987–991. https://doi.org/10.1038/nn.4338

166. Dubbelaar ML, Kracht L, Eggen BJL, Boddeke EWGM (2018) The Kaleidoscope of Microglial Phenotypes. Front Immunol 9:1753. https://doi.org/10.3389/fimmu.2018.01753

167. Torres-Platas SG, Comeau S, Rachalski A, Bo GD, Cruceanu C, Turecki G, Giros B, Mechawar N (2014) Morphometric characterization of microglial phenotypes in human cerebral cortex. J Neuroinflammation 11:12. https://doi.org/10.1186/1742-2094-11-12

168. Hinton G, Roweis S (2002) Stochastic Neighbor Embedding. In: Proceedings of the 15th International Conference on Neural Information Processing Systems. MIT Press, Cambridge, MA, USA, pp 857–864

169. Laurens van der Maaten, Geoffrey Hinton (2008) Visualizing Data using t-SNE. Journal of Machine Learning Research 9:2579–2605

170. Sousa C, Golebiewska A, Poovathingal SK, Kaoma T, Pires-Afonso Y, Martina S, Coowar D, Azuaje F, Skupin A, Balling R, Biber K, Niclou SP, Michelucci A (2018) Single-cell transcriptomics reveals distinct inflammation-induced microglia signatures. EMBO Rep 19. https://doi.org/10.15252/embr.201846171

171. Kim H-J, Cho M-H, Shim WH, Kim JK, Jeon E-Y, Kim D-H, Yoon S-Y (2017) Deficient autophagy in microglia impairs synaptic pruning and causes social behavioral defects. Mol Psychiatry 22:1576–1584. https://doi.org/10.1038/mp.2016.103

172. Sellgren CM, Gracias J, Watmuff B, Biag JD, Thanos JM, Whittredge PB, Fu T, Worringer K, Brown HE, Wang J, Kaykas A, Karmacharya R, Goold CP, Sheridan SD, Perlis RH (2019) Increased synapse elimination by microglia in schizophrenia patient-derived models of synaptic pruning. Nat Neurosci 22:374–385. https://doi.org/10.1038/s41593-018-0334-7

173. Stevens B, Allen NJ, Vazquez LE, Howell GR, Christopherson KS, Nouri N, Micheva KD, Mehalow AK, Huberman AD, Stafford B, Sher A, Litke AM, Lambris JD, Smith SJ, John SWM, Barres BA (2007) The classical complement cascade mediates CNS synapse elimination. Cell 131:1164–1178. https://doi.org/10.1016/j.cell.2007.10.036

174. Kober DL, Brett TJ (2017) TREM2-Ligand Interactions in Health and Disease. J Mol Biol 429:1607–1629. https://doi.org/10.1016/j.jmb.2017.04.004

175. Monteiro S, Roque S, Marques F, Correia-Neves M, Cerqueira JJ (2017) Brain interference: Revisiting the role of IFNγ in the central nervous system. Progress in Neurobiology 156:149–163. https://doi.org/10.1016/j.pneurobio.2017.05.003

176. Biesemann C, Grønborg M, Luquet E, Wichert SP, Bernard V, Bungers SR, Cooper B, Varoqueaux F, Li L, Byrne JA, Urlaub H, Jahn O, Brose N, Herzog E (2014) Proteomic screening of glutamatergic mouse brain synaptosomes isolated by fluorescence activated sorting. EMBO J 33:157–170. https://doi.org/10.1002/embj.201386120

177. Gylys KH, Bilousova T (2017) Flow Cytometry Analysis and Quantitative Characterization of Tau in Synaptosomes from Alzheimer's Disease Brains. Methods Mol Biol 1523:273–

284. https://doi.org/10.1007/978-1-4939-6598-4_16

178. Gray EG, Whittaker VP (1962) The isolation of nerve endings from brain: an electron-microscopic study of cell fragments derived by homogenization and centrifugation. J Anatomy 96:79–88

179. Dunkley PR, Jarvie PE, Heath JW, Kidd GJ, Rostas JA (1986) A rapid method for isolation of synaptosomes on Percoll gradients. Brain Research 372:115–129. https://doi.org/10.1016/0006-8993(86)91464-2

180. Hunsberger HC, Wang D, Petrisko TJ, Alhowail A, Setti SE, Suppiramaniam V, Konat GW, Reed MN (2016) Peripherally restricted viral challenge elevates extracellular glutamate and enhances synaptic transmission in the hippocampus. J Neurochem 138:307–316. https://doi.org/10.1111/jnc.13665

181. Stone TW, Darlington LG (2002) Endogenous kynurenines as targets for drug discovery and development. Nat Rev Drug Discov 1:609–620. https://doi.org/10.1038/nrd870

182. Jeon SW, Kim Y-K (2017) Inflammation-induced depression: Its pathophysiology and therapeutic implications. J Neuroimmunol 313:92–98. https://doi.org/10.1016/j.jneuroim.2017.10.016

183. Carlin JM, Borden EC, Sondel PM, Byrne GI (1989) Interferon-induced indoleamine 2,3-dioxygenase activity in human mononuclear phagocytes. J Leukoc Biol 45:29–34. https://doi.org/10.1002/jlb.45.1.29

184. Fujigaki H, Saito K, Fujigaki S, Takemura M, Sudo K, Ishiguro H, Seishima M (2006) The signal transducer and activator of transcription 1alpha and interferon regulatory factor 1 are not essential for the induction of indoleamine 2,3-dioxygenase by lipopolysaccharide: involvement of p38 mitogen-activated protein kinase and nuclear factor-kappaB pathways, and synergistic effect of several proinflammatory cytokines. J Biochem 139:655–662. https://doi.org/10.1093/jb/mvj072

185. Zunszain PA, Anacker C, Cattaneo A, Choudhury S, Musaelyan K, Myint AM, Thuret S, Price J, Pariante CM (2012) Interleukin-1β: a new regulator of the kynurenine pathway affecting human hippocampal neurogenesis. Neuropsychopharmacology 37:939–949. https://doi.org/10.1038/npp.2011.277

186. Gaelings L, Söderholm S, Bugai A, Fu Y, Nandania J, Schepens B, Lorey MB, Tynell J, Vande Ginste L, Le Goffic R, Miller MS, Kuisma M, Marjomäki V, Brabander J de, Matikainen S, Nyman TA, Bamford DH, Saelens X, Julkunen I, Paavilainen H, Hukkanen V, Velagapudi V, Kainov DE (2017) Regulation of kynurenine biosynthesis during influenza virus infection. FEBS J 284:222–236. https://doi.org/10.1111/febs.13966

187. Cunha C, Brambilla R, Thomas KL (2010) A simple role for BDNF in learning and memory? Front Mol Neurosci 3:1. https://doi.org/10.3389/neuro.02.001.2010

188. Lima Giacobbo B, Doorduin J, Klein HC, Dierckx RAJO, Bromberg E, Vries EFJ de (2019) Brain-Derived Neurotrophic Factor in Brain Disorders: Focus on Neuroinflammation. Mol Neurobiol 56:3295–3312. https://doi.org/10.1007/s12035-018-1283-6

189. Meeker R, Williams K (2014) Dynamic nature of the p75 neurotrophin receptor in response to injury and disease. J Neuroimmune Pharmacol 9:615–628. https://doi.org/10.1007/s11481-014-9566-9

190. Müller N, Schwarz MJ (2007) The immune-mediated alteration of serotonin and glutamate: towards an integrated view of depression. Mol Psychiatry 12:988–1000. https://doi.org/10.1038/sj.mp.4002006

191. Albrecht-Schgoer K, Lackner P, Schmutzhard E, Baier G (2022) Cerebral Malaria: Current Clinical and Immunological Aspects. Front Immunol 13:863568. https://doi.org/10.3389/fimmu.2022.863568

192. Düsedau HP, Kleveman J, Figueiredo CA, Biswas A, Steffen J, Kliche S, Haak S, Zagrebelsky M, Korte M, Dunay IR (2019) p75NTR regulates brain mononuclear cell function and neuronal structure in Toxoplasma infection-induced neuroinflammation. Glia 67:193–211. https://doi.org/10.1002/glia.23553

193. Schlüter D, Barragan A (2019) Advances and Challenges in Understanding Cerebral Toxoplasmosis. Front Immunol 10:242. https://doi.org/10.3389/fimmu.2019.00242

194. Petersen LR, Brault AC, Nasci RS (2013) West Nile virus: review of the literature. JAMA 310:308–315. https://doi.org/10.1001/jama.2013.8042

195. Zhang XZ, Penzel T, Han F (2013) Increased incidence of narcolepsy following the 2009 H1N1 pandemic. Somnologie 17:90–93. https://doi.org/10.1007/s11818-013-0619-8

196. Srivastava B, Błazejewska P, Hessmann M, Bruder D, Geffers R, Mauel S, Gruber AD, Schughart K (2009) Host genetic background strongly influences the response to influenza a virus infections. PLoS ONE 4:e4857. https://doi.org/10.1371/journal.pone.0004857

197. Bahadoran A, Lee SH, Wang SM, Manikam R, Rajarajeswaran J, Raju CS, Sekaran SD (2016) Immune Responses to Influenza Virus and Its Correlation to Age and Inherited Factors. Front Microbiol 7:1841. https://doi.org/10.3389/fmicb.2016.01841

198. Cai KC, van Mil S, Murray E, Mallet J-F, Matar C, Ismail N (2016) Age and sex differences in immune response following LPS treatment in mice. Brain Behav Immun 58:327–337. https://doi.org/10.1016/j.bbi.2016.08.002

199. Gandhi R, Hayley S, Gibb J, Merali Z, Anisman H (2007) Influence of poly I:C on sickness behaviors, plasma cytokines, corticosterone and central monoamine activity: moderation by social stressors. Brain Behav Immun 21:477–489. https://doi.org/10.1016/j.bbi.2006.12.005

200. Gibney SM, McGuinness B, Prendergast C, Harkin A, Connor TJ (2013) Poly I:C-induced activation of the immune response is accompanied by depression and anxiety-like behaviours, kynurenine pathway activation and reduced BDNF expression. Brain Behav Immun 28:170–181. https://doi.org/10.1016/j.bbi.2012.11.010

201. Kodali MC, Chen H, Liao F-F (2021) Temporal unsnarling of brain's acute neuroinflammatory transcriptional profiles reveals panendothelitis as the earliest event preceding microgliosis. Mol Psychiatry 26:3905–3919. https://doi.org/10.1038/s41380-020-00955-5

202. Kallfass C, Ackerman A, Lienenklaus S, Weiss S, Heimrich B, Staeheli P (2012) Visualizing production of beta interferon by astrocytes and microglia in brain of La Crosse virus-infected mice. Journal of Virology 86:11223–11230. https://doi.org/10.1128/JVI.01093-12

203. Owens T, Khorooshi R, Wlodarczyk A, Asgari N (2014) Interferons in the central nervous system: a few instruments play many tunes. Glia 62:339–355. https://doi.org/10.1002/glia.22608

204. Masuda T, Sankowski R, Staszewski O, Böttcher C, Amann L, Sagar, Scheiwe C, Nessler S, Kunz P, van Loo G, Coenen VA, Reinacher PC, Michel A, Sure U, Gold R, Grün D, Priller J, Stadelmann C, Prinz M (2019) Spatial and temporal heterogeneity of mouse and human microglia at single-cell resolution. Nature 566:388–392. https://doi.org/10.1038/s41586-019-0924-x

205. Kraus J, Voigt K, Schuller AM, Scholz M, Kim KS, Schilling M, Schäbitz WR, Oschmann P, Engelhardt B (2008) Interferon-beta stabilizes barrier characteristics of the blood-brain barrier in four different species in vitro. Mult Scler 14:843–852. https://doi.org/10.1177/1352458508088940

206. Veldhuis WB, Floris S, van der Meide PH, Vos IMP, Vries HE de, Dijkstra CD, Bär PR, Nicolay K (2003) Interferon-beta prevents cytokine-induced neutrophil infiltration and attenuates blood-brain barrier disruption. J Cereb Blood Flow Metab 23:1060–1069. https://doi.org/10.1097/01.WCB.0000080701.47016.24

207. Utech M, Ivanov AI, Samarin SN, Bruewer M, Turner JR, Mrsny RJ, Parkos CA, Nusrat A (2005) Mechanism of IFN-gamma-induced endocytosis of tight junction proteins: myosin II-dependent vacuolarization of the apical plasma membrane. Mol Biol Cell 16:5040–5052. https://doi.org/10.1091/mbc.e05-03-0193

208. Chai Q, He WQ, Zhou M, Lu H, Fu ZF (2014) Enhancement of blood-brain barrier permeability and reduction of tight junction protein expression are modulated by chemokines/cytokines induced by rabies virus infection. Journal of Virology 88:4698–4710. https://doi.org/10.1128/JVI.03149-13

209. Loos T, Dekeyzer L, Struyf S, Schutyser E, Gijsbers K, Gouwy M, Fraeyman A, Put W, Ronsse I, Grillet B, Opdenakker G, van Damme J, Proost P (2006) TLR ligands and cytokines induce CXCR3 ligands in endothelial cells: enhanced CXCL9 in autoimmune arthritis. Lab Invest 86:902–916. https://doi.org/10.1038/labinvest.3700453

210. Gack MU, Albrecht RA, Urano T, Inn K-S, Huang I-C, Carnero E, Farzan M, Inoue S, Jung JU, García-Sastre A (2009) Influenza A virus NS1 targets the ubiquitin ligase TRIM25 to evade recognition by the host viral RNA sensor RIG-I. Cell Host Microbe 5:439–449. https://doi.org/10.1016/j.chom.2009.04.006

211. Chung W-C, Kang H-R, Yoon H, Kang S-J, Ting JP-Y, Song MJ (2015) Influenza A Virus NS1 Protein Inhibits the NLRP3 Inflammasome. PLoS ONE 10:e0126456. https://doi.org/10.1371/journal.pone.0126456

212. Oishi K, Yamayoshi S, Kawaoka Y (2015) Mapping of a Region of the PA-X Protein of Influenza A Virus That Is Important for Its Shutoff Activity. Journal of Virology 89:8661–8665. https://doi.org/10.1128/JVI.01132-15

213. Linnerbauer M, Wheeler MA, Quintana FJ (2020) Astrocyte Crosstalk in CNS Inflammation. Neuron 108:608–622. https://doi.org/10.1016/j.neuron.2020.08.012

214. Hasegawa-Ishii S, Inaba M, Umegaki H, Unno K, Wakabayashi K, Shimada A (2016) Endotoxemia-induced cytokine-mediated responses of hippocampal astrocytes transmitted by cells of the brain-immune interface. Sci Rep 6:25457. https://doi.org/10.1038/srep25457

215. Bezzi P, Carmignoto G, Pasti L, Vesce S, Rossi D, Rizzini BL, Pozzan T, Volterra A (1998) Prostaglandins stimulate calcium-dependent glutamate release in astrocytes. Nature 391:281–285. https://doi.org/10.1038/34651

216. Lin J, Zhou L, Luo Z, Adam MI, Zhao L, Wang F, Luo D (2021) Flow cytometry analysis of immune and glial cells in a trigeminal neuralgia rat model. Sci Rep 11:23569. https://doi.org/10.1038/s41598-021-02911-x

217. Zhang X, Kracht L, Lerario AM, Dubbelaar ML, Brouwer N, Wesseling EM, Boddeke EWGM, Eggen BJL, Kooistra SM (2022) Epigenetic regulation of innate immune memory in microglia. J Neuroinflammation 19:111. https://doi.org/10.1186/s12974-022-02463-5

218. Vasek MJ, Garber C, Dorsey D, Durrant DM, Bollman B, Soung A, Yu J, Perez-Torres C, Frouin A, Wilton DK, Funk K, DeMasters BK, Jiang X, Bowen JR, Mennerick S, Robinson JK, Garbow JR, Tyler KL, Suthar MS, Schmidt RE, Stevens B, Klein RS (2016) A complement-microglial axis drives synapse loss during virus-induced memory impairment. Nature 534:538–543. https://doi.org/10.1038/nature18283

219. Neher JJ, Neniskyte U, Zhao J-W, Bal-Price A, Tolkovsky AM, Brown GC (2011) Inhibition of microglial phagocytosis is sufficient to prevent inflammatory neuronal death. J Immunol 186:4973–4983. https://doi.org/10.4049/jimmunol.1003600

220. Scott-Hewitt N, Perrucci F, Morini R, Erreni M, Mahoney M, Witkowska A, Carey A, Faggiani E, Schuetz LT, Mason S, Tamborini M, Bizzotto M, Passoni L, Filipello F, Jahn R, Stevens B, Matteoli M (2020) Local externalization of phosphatidylserine mediates developmental synaptic pruning by microglia. EMBO J 39:e105380. https://doi.org/10.15252/embj.2020105380

221. Schafer DP, Lehrman EK, Kautzman AG, Koyama R, Mardinly AR, Yamasaki R, Ransohoff RM, Greenberg ME, Barres BA, Stevens B (2012) Microglia sculpt postnatal neural circuits in an activity and complement-dependent manner. Neuron 74:691–705. https://doi.org/10.1016/j.neuron.2012.03.026

222. Fonseca MI, Chu S-H, Hernandez MX, Fang MJ, Modarresi L, Selvan P, MacGregor GR, Tenner AJ (2017) Cell-specific deletion of C1qa identifies microglia as the dominant source of C1q in mouse brain. J Neuroinflammation 14:48. https://doi.org/10.1186/s12974-017-0814-9

223. Lian H, Yang L, Cole A, Sun L, Chiang AC-A, Fowler SW, Shim DJ, Rodriguez-Rivera J, Taglialatela G, Jankowsky JL, Lu H-C, Zheng H (2015) NFκB-activated astroglial release of complement C3 compromises neuronal morphology and function associated with Alzheimer's disease. Neuron 85:101–115. https://doi.org/10.1016/j.neuron.2014.11.018

224. Lang D, Schott BH, van Ham M, Morton L, Kulikovskaja L, Herrera-Molina R, Pielot R, Klawonn F, Montag D, Jänsch L, Gundelfinger ED, Smalla KH, Dunay IR (2018) Chronic Toxoplasma infection is associated with distinct alterations in the synaptic protein composition. J Neuroinflammation 15:438. https://doi.org/10.1186/s12974-018-1242-1

225. French T, Düsedau HP, Steffen J, Biswas A, Ahmed N, Hartmann S, Schüler T, Schott BH, Dunay IR (2019) Neuronal impairment following chronic Toxoplasma gondii infection is aggravated by intestinal nematode challenge in an IFN-γ-dependent manner. J Neuroinflammation 16:159. https://doi.org/10.1186/s12974-019-1539-8

226. Postupna NO, Keene CD, Latimer C, Sherfield EE, van Gelder RD, Ojemann JG, Montine TJ, Darvas M (2014) Flow cytometry analysis of synaptosomes from post-mortem human brain reveals changes specific to Lewy body and Alzheimer's disease. Lab Invest 94:1161–1172. https://doi.org/10.1038/labinvest.2014.103

227. Postupna NO, Latimer CS, Keene CD, Montine KS, Montine TJ, Darvas M (2018) Flow cytometric evaluation of crude synaptosome preparation as a way to study synaptic alteration in neurodegenerative diseases. Neuromethods 141:297–310. https://doi.org/10.1007/978-1-4939-8739-9_17

228. Gajera CR, Fernandez R, Montine KS, Fox EJ, Mrdjen D, Postupna NO, Keene CD, Bendall SC, Montine TJ (2021) Mass-tag barcoding for multiplexed analysis of human synaptosomes and other anuclear events. Cytometry A. https://doi.org/10.1002/cyto.a.24340

229. Luk WP, Zhang Y, White TD, Lue FA, Wu C, Jiang CG, Zhang L, Moldofsky H (1999) Adenosine: a mediator of interleukin-1beta-induced hippocampal synaptic inhibition. J Neurosci 19:4238–4244

230. Ikegaya Y, Delcroix I, Iwakura Y, Matsuki N, Nishiyama N (2003) Interleukin-1beta abrogates long-term depression of hippocampal CA1 synaptic transmission. Synapse 47:54–57. https://doi.org/10.1002/syn.10154

231. Wang S, Cheng Q, Malik S, Yang J (2000) Interleukin-1beta inhibits gamma-aminobutyric acid type A (GABA(A)) receptor current in cultured hippocampal neurons. J Pharmacol Exp Ther 292:497–504

232. Manabe T, Rácz I, Schwartz S, Oberle L, Santarelli F, Emmrich JV, Neher JJ, Heneka MT (2021) Systemic inflammation induced the delayed reduction of excitatory synapses in the CA3 during ageing. J Neurochem

159:525–542. https://doi.org/10.1111/jnc.15491

233. Wegrzyn D, Freund N, Faissner A, Juckel G (2021) Poly I:C Activated Microglia Disrupt Perineuronal Nets and Modulate Synaptic Balance in Primary Hippocampal Neurons in vitro. Front Synaptic Neurosci 13:637549. https://doi.org/10.3389/fnsyn.2021.637549

234. Baumgartner R, Forteza MJ, Ketelhuth DFJ (2019) The interplay between cytokines and the Kynurenine pathway in inflammation and atherosclerosis. Cytokine 122:154148. https://doi.org/10.1016/j.cyto.2017.09.004

235. Suh H-S, Zhao M-L, Rivieccio M, Choi S, Connolly E, Zhao Y, Takikawa O, Brosnan CF, Lee SC (2007) Astrocyte indoleamine 2,3-dioxygenase is induced by the TLR3 ligand poly(I:C): mechanism of induction and role in antiviral response. Journal of Virology 81:9838–9850. https://doi.org/10.1128/JVI.00792-07

236. Ciranna L (2006) Serotonin as a modulator of glutamate- and GABA-mediated neurotransmission: implications in physiological functions and in pathology. Curr Neuropharmacol 4:101–114. https://doi.org/10.2174/157015906776359540

237. O'Connor JC, Lawson MA, André C, Moreau M, Lestage J, Castanon N, Kelley KW, Dantzer R (2009) Lipopolysaccharide-induced depressive-like behavior is mediated by indoleamine 2,3-dioxygenase activation in mice. Mol Psychiatry 14:511–522. https://doi.org/10.1038/sj.mp.4002148

238. Schwarcz R, Stone TW (2017) The kynurenine pathway and the brain: Challenges, controversies and promises. Neuropharmacology 112:237–247. https://doi.org/10.1016/j.neuropharm.2016.08.003

239. Walker AK, Budac DP, Bisulco S, Lee AW, Smith RA, Beenders B, Kelley KW, Dantzer R (2013) NMDA receptor blockade by ketamine abrogates lipopolysaccharide-induced depressive-like behavior in C57BL/6J mice. Neuropsychopharmacology 38:1609–1616. https://doi.org/10.1038/npp.2013.71

240. Sadasivan S, Zanin M, O'Brien K, Schultz-Cherry S, Smeyne RJ (2015) Induction of microglia activation after infection with the non-neurotropic A/CA/04/2009 H1N1 influenza virus. PLoS ONE 10:e0124047. https://doi.org/10.1371/journal.pone.0124047

241. Guan Z, Fang J (2006) Peripheral immune activation by lipopolysaccharide decreases neurotrophins in the cortex and hippocampus in rats. Brain Behav Immun 20:64–71. https://doi.org/10.1016/j.bbi.2005.04.005

242. Ghosh A, Carnahan J, Greenberg ME (1994) Requirement for BDNF in activity-dependent survival of cortical neurons. Science 263:1618–1623. https://doi.org/10.1126/science.7907431

243. Wang L, Chang X, She L, Xu D, Huang W, Poo M (2015) Autocrine action of BDNF on dendrite development of adult-born hippocampal neurons. J Neurosci 35:8384–8393. https://doi.org/10.1523/JNEUROSCI.4682-14.2015

244. Zhang J-C, Yao W, Hashimoto K (2016) Brain-derived Neurotrophic Factor (BDNF)-TrkB Signaling in Inflammation-related Depression and

Potential Therapeutic Targets. Curr Neuropharmacol 14:721–731. https://doi.org/10.2174/1570159x14666160119094646

245. Rana T, Behl T, Sehgal A, Srivastava P, Bungau S (2021) Unfolding the Role of BDNF as a Biomarker for Treatment of Depression. J Mol Neurosci 71:2008–2021. https://doi.org/10.1007/s12031-020-01754-x

246. Caviedes A, Lafourcade C, Soto C, Wyneken U (2017) BDNF/NF-κB Signaling in the Neurobiology of Depression. Curr Pharm Des 23:3154–3163. https://doi.org/10.2174/1381612823666170111141915

247. Martinowich K, Manji H, Lu B (2007) New insights into BDNF function in depression and anxiety. Nat Neurosci 10:1089–1093. https://doi.org/10.1038/nn1971

248. Leßmann V (1998) Neurotrophin-Dependent Modulation of Glutamatergic Synaptic Transmission in the Mammalian CNS. General Pharmacology: The Vascular System 31:667–674. https://doi.org/10.1016/S0306-3623(98)00190-6

249. Harley SBR, Willis EF, Shaikh SN, Blackmore DG, Sah P, Ruitenberg MJ, Bartlett PF, Vukovic J (2021) Selective Ablation of BDNF from Microglia Reveals Novel Roles in Self-Renewal and Hippocampal Neurogenesis. J Neurosci 41:4172–4186. https://doi.org/10.1523/JNEUROSCI.2539-20.2021

250. Laudiero L, Aloe L, Levi-Montalcini R, Buttinelli C, Schilter D, Gillessen S, Otten U (1992) Multiple sclerosis patients express increased levels of β-nerve growth factor in cerebrospinal fluid. Neurosci Lett 147:9–12. https://doi.org/10.1016/0304-3940(92)90762-V

251. Stanzel RDP, Lourenssen S, Blennerhassett MG (2008) Inflammation causes expression of NGF in epithelial cells of the rat colon. Exp Neurol 211:203–213. https://doi.org/10.1016/j.expneurol.2008.01.028

252. Minnone G, Benedetti F de, Bracci-Laudiero L (2017) NGF and Its Receptors in the Regulation of Inflammatory Response. Int J Mol Sci 18:1028. https://doi.org/10.3390/ijms18051028

253. Müller N, Schwarz M (2006) Schizophrenia as an inflammation-mediated dysbalance of glutamatergic neurotransmission. Neurotox Res 10:131–148. https://doi.org/10.1007/BF03033242

254. Blaylock RL, Strunecka A (2009) Immune-glutamatergic dysfunction as a central mechanism of the autism spectrum disorders. Curr Med Chem 16:157–170. https://doi.org/10.2174/092986709787002745

255. Ting JT, Feng G (2008) Glutamatergic Synaptic Dysfunction and Obsessive-Compulsive Disorder. Curr Chem Genomics 2:62–75. https://doi.org/10.2174/1875397300802010062

256. Evans DL, Charney DS, Lewis L, Golden RN, Gorman JM, Krishnan KRR, Nemeroff CB, Bremner JD, Carney RM, Coyne JC, Delong MR, Frasure-Smith N, Glassman AH, Gold PW, Grant I, Gwyther L, Ironson G, Johnson RL, Kanner AM, Katon WJ, Kaufmann PG, Keefe FJ, Ketter T, Laughren TP, Leserman J, Lyketsos CG, McDonald WM, McEwen BS, Miller AH, Musselman D, O'Connor

C, Petitto JM, Pollock BG, Robinson RG, Roose SP, Rowland J, Sheline Y, Sheps DS, Simon G, Spiegel D, Stunkard A, Sunderland T, Tibbits P, Valvo WJ (2005) Mood disorders in the medically ill: scientific review and recommendations. Biol Psychiatry 58:175–189. https://doi.org/10.1016/j.biopsych.2005.05.001

257. Kreijtz JHCM, Fouchier RAM, Rimmelzwaan GF (2011) Immune responses to influenza virus infection. Virus Res 162:19–30. https://doi.org/10.1016/j.virusres.2011.09.022

258. Hosp JA, Dressing A, Blazhenets G, Bormann T, Rau A, Schwabenland M, Thurow J, Wagner D, Waller C, Niesen WD, Frings L, Urbach H, Prinz M, Weiller C, Schroeter N, Meyer PT (2021) Cognitive impairment and altered cerebral glucose metabolism in the subacute stage of COVID-19. Brain. https://doi.org/10.1093/brain/awab009

259. Haley MJ, Brough D, Quintin J, Allan SM (2019) Microglial Priming as Trained Immunity in the Brain. Neuroscience 405:47–54. https://doi.org/10.1016/j.neuroscience.2017.12.039

260. Bodea L-G, Wang Y, Linnartz-Gerlach B, Kopatz J, Sinkkonen L, Musgrove R, Kaoma T, Muller A, Vallar L, Di Monte DA, Balling R, Neumann H (2014) Neurodegeneration by activation of the microglial complement-phagosome pathway. J Neurosci 34:8546–8556. https://doi.org/10.1523/JNEUROSCI.5002-13.2014

261. Kalia LV, Lang AE (2015) Parkinson's disease. The Lancet 386:896–912. https://doi.org/10.1016/S0140-6736(14)61393-3

262. Wendeln A-C, Degenhardt K, Kaurani L, Gertig M, Ulas T, Jain G, Wagner J, Häsler LM, Wild K, Skodras A, Blank T, Staszewski O, Datta M, Centeno TP, Capece V, Islam MR, Kerimoglu C, Staufenbiel M, Schultze JL, Beyer M, Prinz M, Jucker M, Fischer A, Neher JJ (2018) Innate immune memory in the brain shapes neurological disease hallmarks. Nature 556:332–338. https://doi.org/10.1038/s41586-018-0023-4

263. Kempuraj D, Thangavel R, Natteru PA, Selvakumar GP, Saeed D, Zahoor H, Zaheer S, Iyer SS, Zaheer A (2016) Neuroinflammation Induces Neurodegeneration. J Neurol Neurosurg Spine 1

264. Ransohoff RM (2016) How neuroinflammation contributes to neurodegeneration. Science 353:777–783. https://doi.org/10.1126/science.aag2590

265. Lasselin J, Karshikoff B, Axelsson J, Åkerstedt T, Benson S, Engler H, Schedlowski M, Jones M, Lekander M, Andreasson A (2020) Fatigue and sleepiness responses to experimental inflammation and exploratory analysis of the effect of baseline inflammation in healthy humans. Brain Behav Immun 83:309–314. https://doi.org/10.1016/j.bbi.2019.10.020

266. McCusker RH, Kelley KW (2013) Immune-neural connections: how the immune system's response to infectious agents influences behavior. J Exp Biol 216:84–98. https://doi.org/10.1242/jeb.073411

267. Sadasivan S, Sharp B, Schultz-Cherry S, Smeyne RJ (2017) Synergistic effects of influenza and 1-methyl-4-phenyl-1,2,3,6-tetrahydropyridine (MPTP) can be eliminated by the use

of influenza therapeutics: experimental evidence for the multi-hit hypothesis. NPJ Parkinsons Dis 3:18. https://doi.org/10.1038/s41531-017-0019-z

268. Toovey S, Jick SS, Meier CR (2011) Parkinson's disease or Parkinson symptoms following seasonal influenza. Influenza Other Respir Viruses 5:328–333. https://doi.org/10.1111/j.1750-2659.2011.00232.x

269. Tulisiak CT, Mercado G, Peelaerts W, Brundin L, Brundin P (2019) Can infections trigger alpha-synucleinopathies? Prog Mol Biol Transl Sci 168:299–322. https://doi.org/10.1016/bs.pmbts.2019.06.002

DECLARATION OF HONOR

„I hereby declare that I prepared this thesis without impermissible help of third parties and that none other than the indicated tools have been used; all sources of information are clearly marked, including my own publications.

In particular, I have not consciously:

- Fabricated data or rejected undesired results
- Misused statistical methods with the aim of drawing other conclusions than those warranted by the available data
- Plagiarized external data or publications
- Presented the results of other researchers in a distorted way

I am aware that violations of copyright may lead to injunction and damage claims of the author and also to prosecution by the law enforcement authorities.

I hereby agree that the thesis may be reviewed for plagiarism by mean of electronic data processing. This work has not yet been submitted as a doctoral thesis in the same or a similar form in Germany or in any other country. It has not yet been published as a whole."

Magdeburg, 20.06.2022 Henning Düsedau